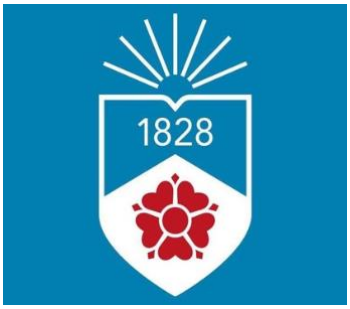

Predicting Meningioma Recurrence Using Spectrochemical Analysis of Tissues and Subsequent Predictive Computational Algorithms

---

by

Taha Luay Lilo

A thesis submitted in partial fulfilment for the requirements for the degree of Doctor of Philosophy at the University of Central Lancashire

March 2022

RESEARCH STUDENT DECLARATION FORM

Type of Award **PhD**

School **School of Pharmacy and Biomedical Sciences**

*Sections marked * delete as appropriate*

1. Concurrent registration for two or more academic awards

Either *I declare that while registered as a candidate for the research degree, I have not been a registered candidate or enrolled student for another award of the University or other academic or professional institution

2. Material submitted for another award

Either ***** I declare that no material contained in the thesis has been used in any other submission for an academic award and is solely my own work

or *

3. Collaboration

Where a candidate's research programme is part of a collaborative project, the thesis must indicate in addition clearly the candidate's individual contribution and the extent of the collaboration. Please state below:

_____

4. Use of a Proof-reader

or *No proof-reading service was used in the compilation of this thesis.

Signature of Candidate

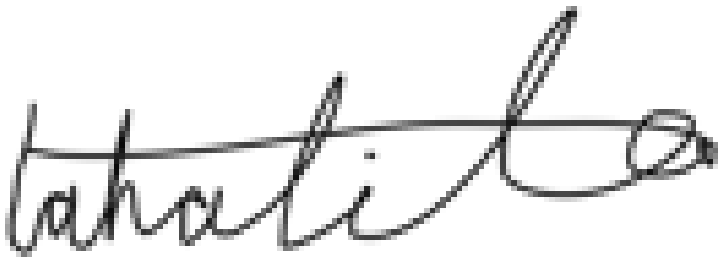

Print name: Taha L Lilo

ABSTRACT

INTRODUCTION Meningiomas are the most common types of tumour of the central nervous system (CNS) and are classified as WHO grades (1,2 ,&3) depending on histological sub-type, tumour growth rate and the likelihood of recurrence. The majority of meningioma are benign, yet, around 10% will recur following resection. Variation in follow-up of patients comes with significant clinical, logistical, and financial implications, hence, the search for predictors for meningioma recurrence has become an increasingly urgent research topic.

AIM The aim was to assess the suitability of biospectroscopy sensor-based techniques Fourier-transform infrared (FTIR) and Raman spectroscopy for analysis of meningioma tissues to accurately segregate patients with benign meningioma (WHO 1 &2) into either high-risk group for recurrence or low risk group based on the spectrochemical signature.

METHODS Patients with convexity meningioma (n=99), Simpson grade 1 or 2 only and WHO grade 1 (n=70) or grade 2 (n=24) with a minimum 5 years follow up (n=5 recurrence) were consented for study. Formalin-fixed paraffin-embedded (FFPE) were sectioned and de-waxed prior to ATR-FTIR or Raman spectrochemical analyses. Derived spectral datasets were then explored for discriminating features *via* multivariate analysis and machine learning algorithms, such as principal component analysis linear discriminant analysis (PCA-LDA) and partial least squares discriminant analysis (PLS-DA). Three-dimensional (3D) discriminant analysis techniques were also used to analyse Raman hyperspectral tissue images in a (3D) fashion.

RESULTS: WHO grade 1 verses grade 2 meningioma samples and those that recurred from those that did not recur were accurately and blindly segregated. For the ATR-FTIR data, PLS-DA gave the best results where grade 1 and grade 2 meningiomas were discriminated with 79% accuracy, 80% sensitivity and 73% specificity; while grade 1 *vs.* grade 1 recurrence and grade 2 *vs.* grade 1 recurrence were discriminated with 94% accuracy (94% sensitivity and specificity) and 97% accuracy (97% sensitivity and 100% specificity), respectively. For the Raman data, the classical spectral analysis after extracting each spectrum from the Raman imaging area achieved best classification performances by using principal component analysis-quadratic discriminant analysis (PCA-QDA) and successive projections algorithm quadratic discriminant analysis (SPA-QDA), resulting in accuracies of 96.2%, sensitivities of 85.7% and specificities of 100% using both algorithms. For the Raman 3D image data, 3D principal component analysis quadratic discriminant analysis (3D-PCA-QDA) was able to distinguish grade 1 and grade 2 meningioma samples with 96% test accuracy (100% sensitivity and 95% specificity), and most recurrence samples were predicted as grade 2 which have higher likelihood of recurrence.

DISCUSSION Several wavenumbers were identified as possible biomarkers towards tumour differentiation, associated with lipids, protein, DNA/RNA, and carbohydrate alterations. For Raman spectroscopy, the following wavenumbers were found to be associated with class differentiation: 850 cm^{-1} (amino acids or polysaccharides), 1130 cm^{-1} (phospholipid structural changes), the region between 1230–1360 cm^{-1} (Amide III and CH_2 deformation), 1450 cm^{-1} (CH_2 bending), and 1858 cm^{-1} (C=O stretching). These findings highlight the potential of Raman microspectroscopy imaging for determination of meningioma tumour grades.

CONCLUSION Reagent-free, non-destructive, and low-cost ATR-FTIR and Raman spectroscopy techniques could give predictive information towards meningioma grade discrimination and the propensity of meningioma to recur. This has enormous clinical potential with regards to being developed for intra-operative real-time assessment of disease. In addition, by building a predictive reoccurrence model in advance, it would be possible to predict the best treatment for the patient according to the likelihood of tumour reoccurrence.

DEDICATION

To the best parents anyone could ask for, Sarab and Luay, for your unconditional love, support, and patience.

To my beautiful wife, Anna, for being my best friend and problem solver.

ACKNOWLEDGEMENTS

Thanks for my supervisory team

Dr Jane Alder, for helping me writing up, proof reading, and meeting deadlines.

Professor Frank Martin, for project design and using his spectroscopy lab at UCLan.

Professor Tim Dawson, for histopathology training, using the BTNW facility, and providing the meningioma subtypes slides from his own library.

Mr Gareth Roberts, for his regular meetings as a clinical supervisor, regarding work progress, design refinements and using his patients datasets.

Professor Charles Davis, see prologue.

Professor Nihal Gurusinghe, for his regular meetings as a clinical supervisor, using his patients datasets.

Thanks for the UCLan team for their support

Dr Lisa Shaw, for her support as RDT at UCLan.

Dr Chris Smith, for his help and ideas to progress as transferring from MD to PhD degree.

Dr Julie Burrow, for all her help running the labs and logistic support.

Dr Camilo Morais, for his ongoing support with the mathematics, MATLAB®, and algorithms.

Thanks for my senior colleagues and clinicians at the Royal Preston Hospital

Mr Gregory Hall, for giving me the tools to reflect on from his own PhD experience.

Mr Arup Ray, for his persistence in pushing me seeing the light at the end of the tunnel when I could not!

Mrs Katherine Ashton, for her support in research neuropath lab and training me in preparation of slides.

Dr Joseph Jacob, for his help with slides preparation and histopathology analysis.

The Sydney Driscoll Foundation for the ongoing support and facilities.

The Brain Tumour Northwest for providing tissue samples, slides, and images.

TABLE OF CONTENTS

LIST OF TABLES

LIST OF FIGURES

CHAPTER 1 | INTRODUCTION

CHAPTER 4 | RAMAN SPECTROSCOPY ANALYSIS

PROLOGUE

Back in 2013, when I was a junior neurosurgical registrar at the department of neurosurgery at the Royal Preston Hospital; Professor Charles Davis, called me to his office. Thoughts started rushing into my head. I was walking through the department corridors trying to think of reasons of why I got summoned to his office and what I possibly may have done wrong in the past week or two.

When I got to him, he asked me to tell him what I knew about meningioma. I promptly recited a couple of paragraphs I remembered from a neurosurgical textbook I was studying on, which only reflected the basic level of understanding that I had for the topic at the time. Despite the coarseness of my knowledge, saying that the reason I was asked to his office is that he was looking for someone with "inquisitive mind" and my name was suggested.

He then continued: "Do you know what those lockers on both side of the corridor are?".

I replied negatively. He explained that those were the files of his meningioma patients. He proudly carried on telling me about him starting the very first meningioma clinic in the UK in 1989.

He then ended the conversation with this very statement:

"Those files are yours now; you breath, eat, wake up and sleep with those folders in your mind until we get answers!".

Although I kept quiet but, in my head, I was wondering "answers for what?".

During the six months that followed, we underwent a full retrospective and prospective review of meningioma patients, examining the conventional methods to predict recurrence

with various hormone receptors and other immunohistochemistry markers. New slides were made, prepared, and examined.

After many hours of hard work and dedication, we finally had the occasion to present our work to the British Neuro-Oncology Society (BNOS) meeting in July 2013. On that warm British summer day in Durham, with the title "Meningioma-Predicting Recurrence", We concluded that with our then current knowledge and understanding of the disease, we did not actually comprehend which meningioma recurs nor why and when they do! Therefore, it is very difficult for the neurosurgeons to justify discharging meningioma patients even if the disease was deemed "benign".

The audience were then divided into two groups: a group opposing my suggestion for logistic, financial, and capacity reasons pertaining to the NHS setting. The other group, that was more supportive of our suggestion of following up meningioma patients for life giving the current evidence. It seemed to me the latter group was made up mainly of senior neurosurgeons. Possibly with their wide and extensive experience, they came across one or two difficult scenarios where they have discharged a patient to discover years later their disease have recurred and probably at that point it was too late to do something about it.

On that evening, as I was driving back home, I had a mixture of feelings; a feeling of joy for winning the prize of best oral presentation at the BNOS and another feeling, that was the one nagging me: earlier that day I presented only a problem without a solution!

When the endorphins of triumph eventually faded, I was only left with the unanswered question: "Why the so called "benign" meningioma recurs?"

Ultimately, after more than a year of asking myself this question I only developed the courage to carry this question forward to academics, who helped me formulate and structure this quest. The following six years or so was what I did.

First, I started looking into lipids biomarkers and immunohistochemistry and after almost a year and half and a couple of experiments I concluded this is probably not the best way forward for me, so I started all over again. This time with spectrometrical analysis.

Between changing direction of my research, being a full-time doctor and subsequently the pandemic, I cannot deny that more than few times I was close to giving up, I am now very glad I did not.

The following few chapters are my attempts to answer this question I asked myself driving back from Durham, is there a better way than following up all meningioma patients for life? Can we segregate those patients who deemed benign but have more potential for recurrence?

I hope this work provides the first steps for much longer path for myself and may be useful also for future researchers.

I would like to think of this work as a story that applies to almost anything in life: Do not be afraid to ask questions; If there is a question, there must be an answer to it somewhere.
No matter how difficult or daunting the journey might seem, enjoy the process and every step along the way.

Taha L. Lilo

Preston, UK

October 2021

The UK first meningioma only clinic files at the Royal Preston Hospital 2013

CHAPTER 1 | INTRODUCTION

1.1 Introduction to meningioma

The majority of brain cancers are classified as glioma or meningioma (Gajjar *et al.*, 2013). Gliomas are a more aggressive type of tumour, defined as neuroepithelial tumours originating from the glial or supporting cells of the central nervous system (CNS) (Davis *et al.*, 2018). Meningiomas are the most common type of brain and intradural spinal tumour, originating from meningeal coverings that surround the brain and the spinal cord. The location, progression, and severity for patients with meningioma varies, but are typified as slow-growing tumours with a poor prognosis; and are often diagnosed at a very large size (Mehta *et al.*, 2019). The majority of meningioma occur in a supratentorial location, while a few arise in the posterior cranial fossa and, rarely, as extra cranial meningiomas (Takahashi et al., 2019). Meningioma often manifests as single or sporadic lesions, producing symptoms such as sensory and motor deficits and gait disturbance, while multiple meningiomas are commonly associated with neurofibromatosis type II (Yeo et al., 2019).

Meningiomas can be divided into WHO grade 1 (benign), grade 2 (atypical) and grade 3 (anaplastic) (Louis *et al.*, 2021). Grade 1 meningiomas are the most common type of tumours, with slower growth and lower likelihood of recurrence; grade 2 meningiomas also have a slower growth, compared to grade 3, but higher likelihood of recurrence. One recent

study found the median progression free survival in all patients was 4.6 years for grade two meningiomas (Bender *et at*., 2021).

Grade 3 meningiomas are a very rare type of tumour with fast growing rate and much higher likelihood of recurrence. Accurate diagnosis is important since surgical outcomes and treatment are dependent on the meningioma grade and histological subtypes.

1.2 History of meningioma terminology

Having an appreciation of the history of meningiomas is of vast importance so we better understand the evolution in the nomenclature of histological classification. Interestingly, the nomenclature was not only the product of the histopathological basis of identification, but also of other factors, such as the socio-national influence of the era (Barthélemy *et al.*, 2016). Cushing first introduced the term "meningioma", in 1922 (Cushing, 1922). The tumour commonly runs a benign course; however, around 20-35% of the tumours are atypical or malignant (McLendon *et al.*, 2006). Although Cushing was the first to use the term, he was not the first to describe "meningiomas" (Ellenbogen *et al.*, 2018). In fact, he stated in his paper that those lesions must have struck the anatomists for long time (Cushing, 1922). The first known description of meningioma in an autopsy report was by Felix Plater in 1614 (Rockhill *et al.*, 2007). The first specific scientific publication to describe the tumour was written by the French surgeon Antoine Louis 1774 who wrote the first scientific treatise devoted exclusively for this tumour called: "fungoid tumours of the dura mater" (al-Rodhan & Laws Jr, 1990; Netsky & Lapresle, 1956). Following that, the 19th century the French pathologist Jean Cruveilhier dedicated a chapter in his book "Pathological Anatomy of Human Body" for the "Cancerous

tumours of the meninges" (Bakay, 1989). His description included a beautifully hand drawn pictures of meningiomas (Figure 1.1).

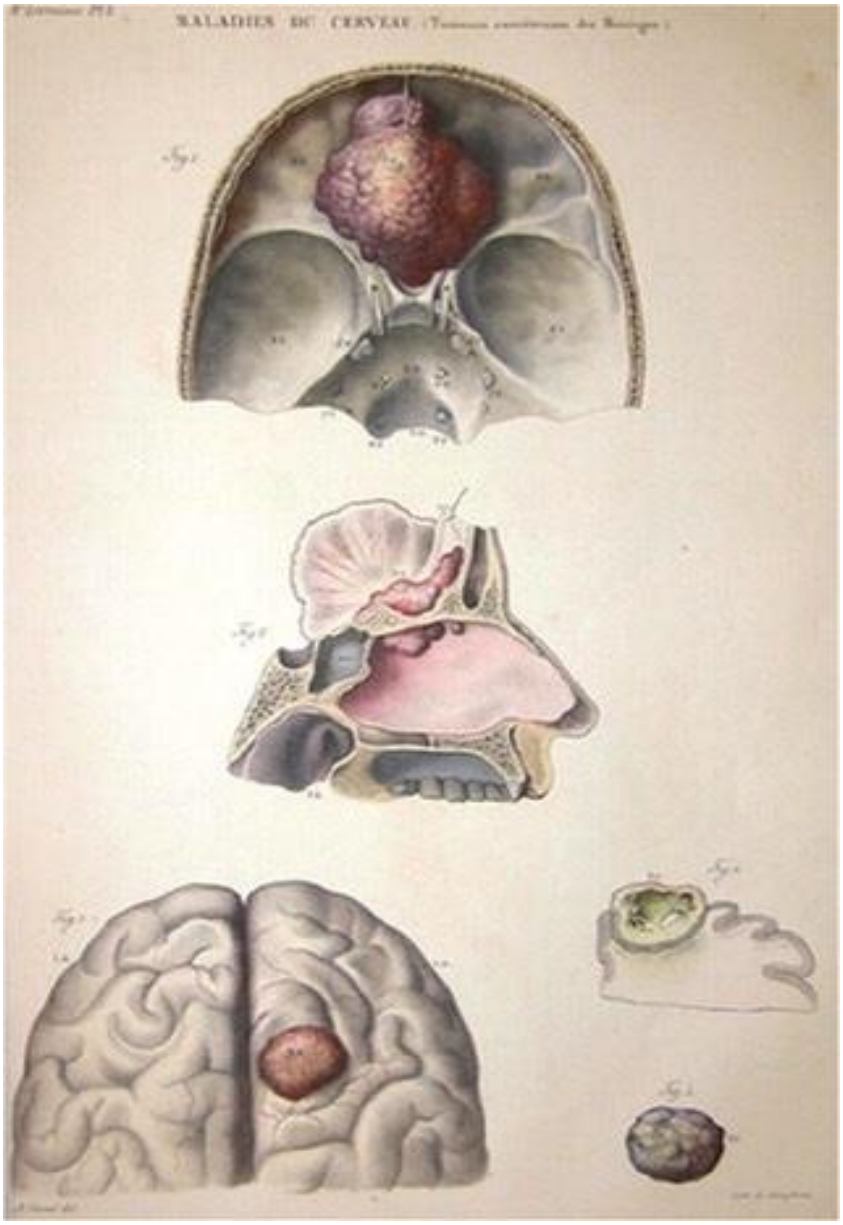

Figure 1.1 Cruiveilhier's Anatomie Pathologique Du Corps Humain showing (Cancerous Tumors of the Meningies). Public Domain; courtesy of the University of Low Libraries.

Cruveilhier, however, was uncertain whether those tumours were malignant or not so he suggested the use of the term "cancerous" delicately (Barthélemy *et al.*, 2016). In the 19th century, the Franco German histopathologist Hermann Lebert gave the name "Fibroplastic intra cranial tumours" in his histopathological description of tumours of the CNS. He initially regarded them as benign tumours, however in his later works he divided them into benign and those with malignant potential (Lebert, 1851). Around the same period, in 19th century Germany, the prominent physician, Virchow, noticed the granular nature of some of the specimens he came across for which he used the term "psammoma" borrowing from Greek for sand "brain sand tumours" (Barthélemy *et al.*, 2016). Virchow's supremacy drew attention away from his contemporaries attempts to name the lesions; like the British surgeon and pathologist Sir James Paget who described them "myeloid" in nature and the German Heinrick Meckel who used the term "acervuloma" (Cushing & Eisenhardt, 1938). Virchow later offered the term "sarcoma" in addition to his previously suggested name. Thus, he expressed his belief of the malignant nature of those tumours despite his earlier support to Lebert's claims of the benign nature of those lesions (Barthélemy *et al.*, 2016). Another term was proposed by Charles Philippe Robin "epithelioma"; yet, it did not get much attention. By the end of the 19th and the beginning of the 20th century, the terms "endothéliome" and "endothelioma" by Bouchard and Golgi respectively dominated in Europe. In fact, it was used an alias for "Meningiomas" in Cushing's 1922 Cavendish lecture in London (Barthélemy *et al.*, 2016).

In 1879, the prominent Scottish surgeon, William Macewen, described what could have been the first meningioma surgery. In his 1888 invited address to the British Medical Association society in Glasgow, he described seven brain surgeries he had conducted successfully using his own brain mapping technique through clinical signs and symptoms (Figure 1.2). One of which was his operation on Barbara Watson, a fourteen year- old who presented with recurrence of tumour above her left eyeball. He had removed her periosteal

tumour a year before. This time she presented with left pupillary miosis, pain and cognitive slowness. While she was admitted to his ward for observation, she was found to suffer from right sided convulsions involving the face, arm and the leg followed by a generalised seizure with loss of consciousness. He started his surgery by removing a barley sized lesion which was adherent to the periosteum and similar in consistency to the lesion he removed a year before. He found the bone rough and soft to touch. Then he removed a 1-inch piece of bone by trephine and found a similar finding on the inner table of the skull. He found that a considerable amount of the tumour had spread over the inner plate and into the dura matter of the brain. He removed as much as was practical. Barbara recovered well after surgery and her symptoms improved. She lived for another 8 years and she died of an unrelated cause secondary to Bright's disease, known today as acute or chronic nephritis. Her post-mortem autopsy showed no evidence of tumour recurrence. Macewen never received the recognition as the first meningioma surgeon for a number of reasons, one of which was the absence of any histopathological evidence in addition to the autopsy result. Cushing himself questioned the nature of the lesion that he came across by saying he was unfortunate not have happened on a true brain tumour. Cushing, however, gave Macewen the credit of being the chief pioneer in cranio-cerebral surgery (Macmillan, 2005).

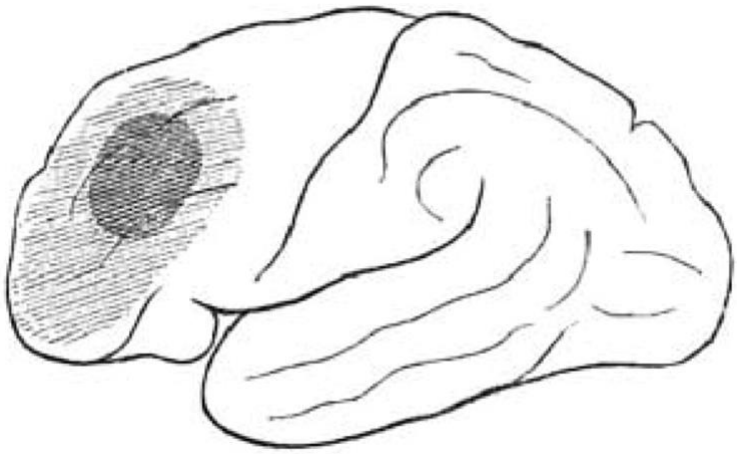

Figure 1.2 The localisation of the lesion in the first documented surgical removal of meningioma (Macmillan, 2005).

As the global leadership in medicine and surgery was gradually shifting across the Atlantic, William Keen was the first brain surgeon who performed a successful brain tumour resection in the United States in December 1887, on a convexity meningioma. The patient survived 30 years after his surgery. Keen used to use the term "endothelioma" nevertheless, both the surgeon and the patient referred to it as a "fibroma" (Doyle *et al.*, 2017).

Cushing's observation of the nomenclature confusion over the past two centuries in Europe supported by his awareness of a new American leadership in the field possibly encouraged him to introduce a new term for those tumours. His choice of the new term was selected regardless of their histology, calvarial involvement or any other varieties (Cushing, 1922).

1.3 Origin

The origin of meningioma is thought to be located in the progenitor cells that give rise to arachnoid cap cells outside of the thin arachnoid layer that covers the CNS (Pećina-Šlaus *et*

al., 2016). There is striking resemblance between meningiomas and arachnoid cap cells (Wiemels *et al.*, 2010). They both share structural and functional features, like; desmosomes, tight junctions, pinocytic vesicles (Pećina-Šlaus *et al.*, 2016).

When Cushing used his new term, it was already known that meningiomas did not arise from the meninges but from the arachnoid villi (Barthélemy *et al.*, 2016). Those are primarily found along major venous sinuses, mainly around the superior sagittal sinus (Asaoka *et al.*, 2002). Yet, meningioma can be present anywhere arachnoid villi are abundant (Kleihues *et al.*, 1993). Hence, there are many reported cases of rarely located meningioma. This may represent a diagnostic challenge clinically and radiologically (Kleihues *et al.*, 1993).

1.4 Epidemiology

Meningioma represents over 36% of all primary CNS tumours according to the latest CBTRUS statistical report (Ostrom *et al.*, 2016). That makes meningioma the most common CNS primary brain tumour (Figure 1.3) with overall prevalence of 97.5/100000 reported cases in the United States (Wiemels *et al.*, 2010). The incidence of meningioma in the UK from 1996 to 2008 was 5.30 per 100,000 person-years (Cea-Soriano *et al.*, 2012). The true prevalence, however, could be higher; one autopsy study found that 2.3% of individuals have undiagnosed asymptomatic meningioma (Larjavaara *et al.*, 2008).

Meningioma affects more women than men in adults with a male: female ratio ranging from 1:4 up to 1:10 and a 1:2 male: female ratio for cranial meningioma (Ellenbogen *et al.*, 2018; Levy Jr *et al.*, 1982). Spinal meningioma represents only 7.5-12.7% of all meningiomas

(Solero *et al.*, 1989). In the UK, incidence was found to be higher in women than in men (7.19 vs. 3.05 per 100,000 person-years) (Cea-Soriano *et al.*, 2012).

The risk of developing meningioma increases with age (Longstreth Jr *et al.*, 1993) with a peak incidence around the sixth to seventh decades of life (Louis *et al.*, 2007). In children, meningiomas are less common, representing 0.4-4.6% of all childhood central nervous system tumours and 1.5-2% of all meningiomas (Louis *et al.*, 2007). Using data from the National Cancer Intelligence Network on tumour site, to identify 42,207 tumour cases, self-reported ethnicity was obtained from hospitals and meningioma was found to be significantly ($p<0.01$) more common in Black African populations compared to White with an incidence rate ratio of 1.29 (1.05–1.59) (Maile *et al.*, 2016). A similar pattern was observed in the US where Black Africans had a higher incidence compared to White and Hispanic races (Wiemels *et al.*, 2010).

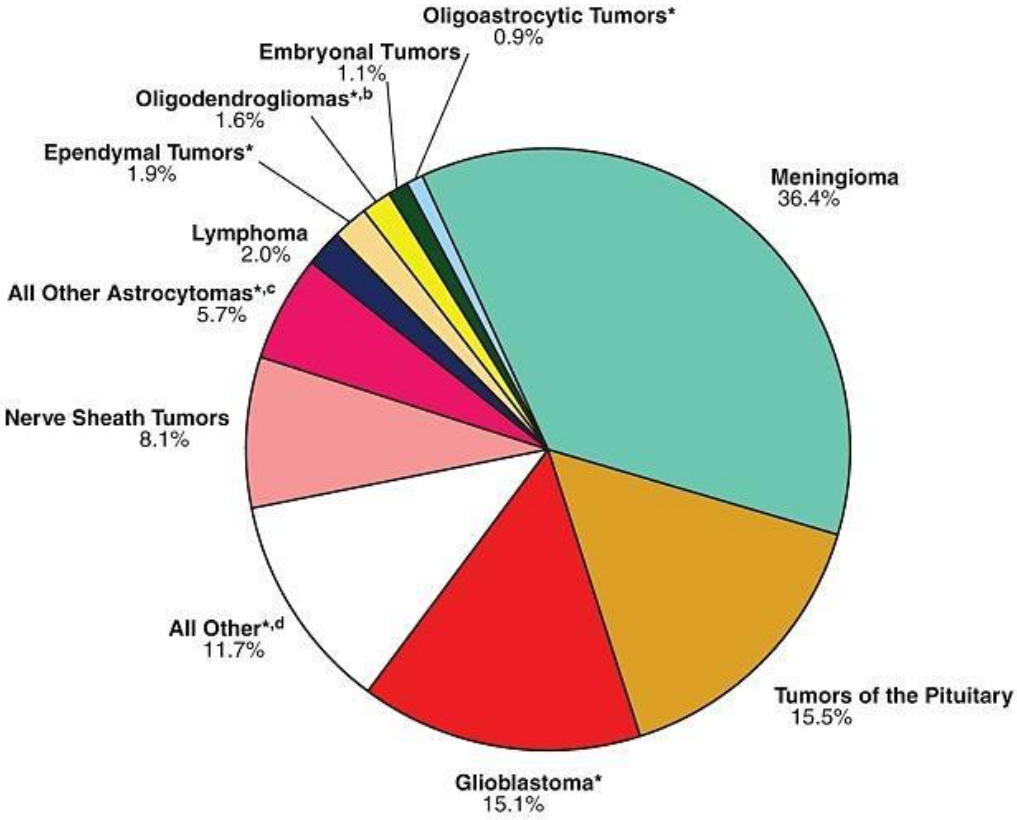

Figure 1.3 The relative incidence of CNS brain tumours from the CBTRUS report (Ostrom *et al.*, 2016).

1.5 Meningioma Genetics and Molecular Profiling

There are a number of genetic alterations observed in meningiomas for example inactivating mutations in NF2 and MEN1 and recurrent somatic mutations in PIK3CA, TRAF7, KLF4, AKT1, SMO, and POLR2A in benign (grade 1) tumours (Yuzawa *et al.*, 2016). Nevertheless, the majority of meningiomas are sporadic. Monosomy of chromosome 22 and NF2 are by far the most common and the most established (Louis *et al.*, 2007). Studies go back to 1972 linking meningiomas to monosomy of chromosome 22 (Hartmann *et al.*, 2006). Loss of 22q occurs in up to 50-60% patients and it is the most frequent chromosomal alteration in meningioma (Hartmann *et al.*, 2006). Recent scientific advances have improved our knowledge to how the NF2 gene loss results in tumour formation though its product protein, Merlin (Pećina-Šlaus, 2013). Patel *et al.* (2019) have managed to characterise the molecular profile of the high-grade meningioma, most likely to reoccur having loss of the repressive DREAM complex, a highly conserved set of proteins involved in regulating the cell cycle and keeping cells quiescent. When this repression is lost, cell cycle progression and proliferation became elevated.

Almost 61% of meningiomas are progesterone receptor positive (PR+). Typically, PR+ meningiomas run a benign course (Louis *et al.*, 2007). The expression of oestrogen receptors (ER), however, may be of less prognostic value (Alexiou *et al.*, 2011). Since somatostatin receptors are expressed in 70-100% of meningiomas, they may be utilised to maximise resection and early detection of recurrence through imaging the radiolabelled tumours (Alexiou *et al.*, 2011). Other markers have also been researched in meningiomas with possibly less

clinical significance, such as epidermal growth factor receptor (EGFR) and platelet-derived growth factor (PDGF). Cyclooxygenase-2 (COX-2) expression has also been linked to tumour progression and angiogenesis (Alexiou *et al.*, 2011).

In the most recent updated WHO guidelines the following molecular biomarkers have been defined for classification and grading of meningiomas, including SMARCE1 (clear cell subtype), BAP1 (rhabdoid and papillary subtypes), and KLF4/TRAF7 (secretory subtype) mutations, TERT promoter mutation and/or homozygous deletion of CDKN2A/B (CNS WHO grade 3) to predict early recurrence, H3K27me3 loss of nuclear expression to predict poor prognosis and methylome profiling to predict recurrence risk (Louis *et al.*, 2021).

A recent large study examining over 3000 meningiomas found some interesting corelations between meningioma genomic subgroups and clinical features including tumour location. Those genomic subgroups were linked with tumour locations, such as the relation of HH tumours with midline location, and the relation of non-NF2 tumours in anterior skull base regions. Those findings along with other relations of genomic subgroups to patients and clinical features will help us to use targeted therapies. Coupled with machine learning algorithms, those findings open the door for non-invasive diagnosis (Youngblood *et al.*, 2020).

1.6 Risk Factors

Some authors classify risk factors in meningioma to modifiable and non-modifiable risk factors as shown in Table 1.1.

Table 1.1 A summary of predisposing risk factors to meningioma.

Non-Modifiable Risks	**Modifiable Risks**
Age: meningioma is more common in adults	Exposure of brain to ionising radiation: There are a number of ways through which iatrogenic radiation could have happened: A cohort of children immigrants to Israel were treated for head worms (*Tinia Capitis*) by exposure to ionising radiation during the 1950's. It was noted since the 1980's there was a significant increased incidence of meningioma in this group compared to public (Sadetzki *et al.*, 2000). The survivors of atomic bomb exposure in Nagasaki and Hiroshima: A review of the bombing survivors suggested a statistically significant increase for schwannomas and statistically non- significant increase for meningioma and other CNS tumours (Preston *et al.*, 2002). Radiotherapy for other cranial conditions: A review of literature looked into patients who received radiotherapy in the pediatric and young adult age group found increased risk of meningioma including WHO 1, 2 &3 with a latency period of 22.9±11.4 years (Yamanaka *et al.*, 2017). Dental x-rays: A study found increased incidence of meningiomas in patient who have been exposed to dental x-ray in the past when the radiation exposure was higher compared to the modern era (Claus *et al.*, 2012).
Gender: Female more common than Male	Exposure to exogenous sex hormones in females: Some papers have found a statistical link between sex hormones and the development of meningiomas while others have found no significant link have been found between external exposure to female sex hormones and meningiomas (Claus *et al.* 2013; Jhawar *et al*., 2003)
Genetic disorders; such as NF2	Meningioma and obesity: A strong positive relation was found between females with high BMI and the development of meningioma. There is relation between obese men and increased risk of meningioma probably through conversion of androgen to estrogen in peripheral tissue (Claus *et al.* 2013).
Ethnicity: more common in Black Africans	

1.7 Histopathological classification

Meningioma histological classification is part of the WHO classification of central nervous tissue tumours. Historically, this was first initiated by the WHO and the world health assembly in 1956 and 1957 respectively. The objective was to unify a worldwide accepted system through which a clear histopathological and clinical diagnosis can be made. Without it, no large-scale international collaborative epidemiological studies or clinical trials would have been possible.

The criteria have evolved over the years reflecting the progressive advances in the field of diagnostics; in 1979 the first edition was published reflecting the histological typing. Followed by the 1993 second edition which included immunohistochemistry into diagnostic pathology. The third edition was published in 2000 which incorporated genetic profiles. In this edition, the blue book, as the series known, have markedly evolved to feature sections on imaging, clinical findings, epidemiology, prognosis, and predictive factors. The 2007 edition has included more collaboration with geneticists and featured new variants and entities. The 2016 included brain invasion as a criterion for WHO 2meningioma. The 2021 edition introduces major changes that advance the role of molecular diagnostics in CNS tumour classification integrated with other established approaches such as histology and immunohistochemistry (Louis et al., 2021).

1.7.1 Grade 1

For tumours with low proliferative potential and possibly cure following surgery. Within the benign WHO 1 category for meningiomas, there are several subtypes: Meningothelial, fibrous, transitional, psammomatous and angiomatous meningiomas. Those

classifications are imprecise in predicting patient outcome and recurrence. The most common subgroups for grade 1 are meningiothelial, fibrous and transitional.

1.7.2 Grade 2

Implies infiltrative behaviour of the tumour and often recurs. It also has the potential to progress to a higher-grade malignant tumour. For the WHO grade 2 meningiomas, subgroups include clear cell and choroid.

1.7.3 Grade 3

For tumours with malignant features like nuclear atypia and brisk mitotic activity. Those lesions usually require adjuvant therapy. grade 3meningiomas include; anaplastic, papillary and rhabdoid.

In Table 1.2 is shown the WHO criteria for the histological grading of meningiomas (Perry *et al.*, 1997).

Table 1.2 WHO criteria for the histological grading of meningiomas.

Benign WHO grade 1	**Atypical WHO grade 2**	**Anaplastic WHO grade 3**
Histological variant other than clear cell, Chordoid, papillary and rhabdoid	Mitotic activity ≥ 4/10 HPF Plus;	Mitotic index ≥ 20/10 HPF
Lacks criteria of atypical and anaplastic meningioma	Brain invasion Or;	Papillary Rhabdoid Frank anaplasia Malignancy cytology (resembling sarcoma, carcinoma or melanoma-like histology)
Meningiothelial Fibrous Transitional Psammomatous Angiomatous Microcystic Secretory Lymphoplasmacyte-rich Metaplastic	At least 3 of 5 parameters: -sheeting architecture (loss of whirling and/or fascicles) -small cell formation (high nuclear-to-cytoplasmic ratio) -macronucleoli -hypercellularity -spontaneous necrosis (not induced by radiation or embolization)	*any one of the above qualify

The WHO then classified the histological subtypes into two groups according to their risk of recurrence and aggressive behaviour, as shown in Table 1.3.

Table 1.3 2016 Meningioma variants grouped by the WHO grade and biological behaviour

Meningiomas with low risk of recurrence;

Histology	**Grade**
Meningiothelial	WHO 1
Fibrous (Fibroplastic)	WHO 1
Transitional (mixed)	WHO 1
Psammomatous	WHO 1
Angiomatous	WHO 1
Microcystic	WHO 1
Secretory	WHO 1
Lymphoplasmacyte-rich	WHO 1
Metaplastic	WHO 1

1.7.5 The histological variants of meningiomas

The three most common histological subtypes are the meningiothelial, fibrous and the transitional.

1.7.5.1 Meningothelial meningioma

A classic common type characterised by a medium sized epithelioid tumour cells forming lobules partly demarcated by a thin collagenous septa. The tumour cells of this type are largely uniform with oval nuclei. Eosinophilic cytoplasm is abundant. Whorls and psammoma bodies are infrequent. However, when present they tend to be less formed than in the transitional, fibrous or psammomatous subtypes (Figure 1.4).

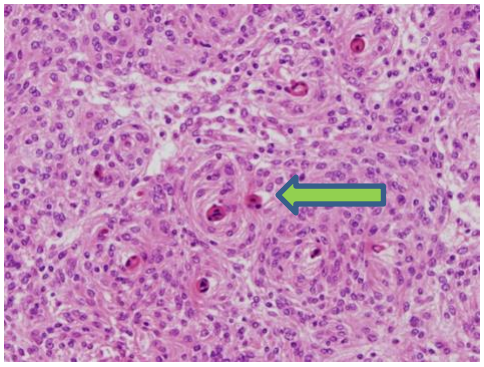

Figure 1.4 Meningiothelial meningioma.

1.7.5.2 Fibrous meningioma

Another classic and common type of meningioma. Consists of spindles of cells forming parallel storiform and interlacing bundles in a collagen rich matrix. Similar to meningiothelial meningioma, whorl formation and psammoma bodies are infrequent (Figure 1.5).

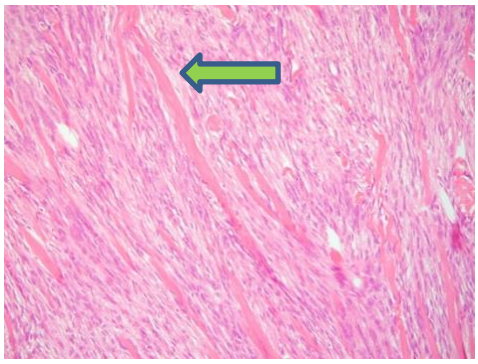

Figure 1.5 Fibrous meningioma.

1.7.5.3 Transitional meningioma

Another common variant. Contains meningiothelial and fibrous patterns as well as transitional features. Lobular and fascicular foci appear side by side with conspicuous tight whorls and psammoma bodies. Common in NF2 mutation meningiomas (Figure 1.6).

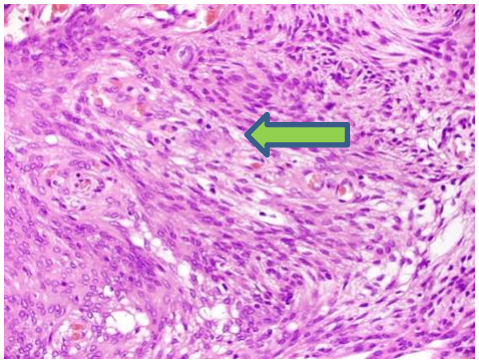

Figure 1.6 Transitional meningioma.

1.7.5.4 Psammomatous meningioma

Contains an abundance of psammoma bodies over tumour cells commonly in the transitional variant. Often the psammoma bodies become confluent forming irregular calcified masses and occasionally bone. Commonly found in thoracic spine meningioma. Bone related proteins including osteopontin produced by CD68 positive macrophages are thought to play a role in its formation (Al-Metfy *et al.*, 2011) (Figure 1.7).

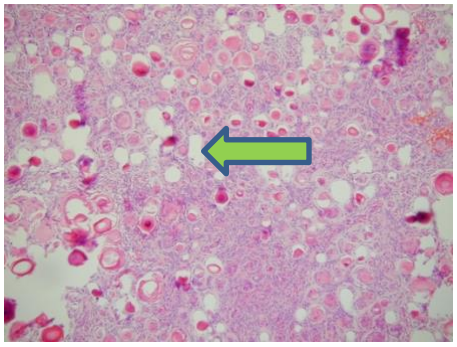

Figure 1.7 Psammomatous meningioma.

1.7.5.5 Angiomatous meningioma

Also known as vascular meningioma. Features numerous small and medium size blood vessels with hyalinised walls. Often constitute a greater proportion of the tumour mass than other types. The differential diagnosis of this type includes vascular malformations and haemangioblastoma (Figure 1.8).

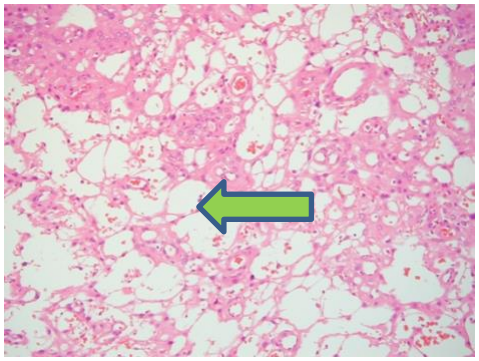

Figure 1.8 Angiomatous meningioma.

1.7.5.6 Microcytic meningioma

Characterised by cells with thin elongated processes encompassing microcysts and creating a cobweb-like background. Atypia and cerebral oedema are common, but they are typically benign (Figure 1.9).

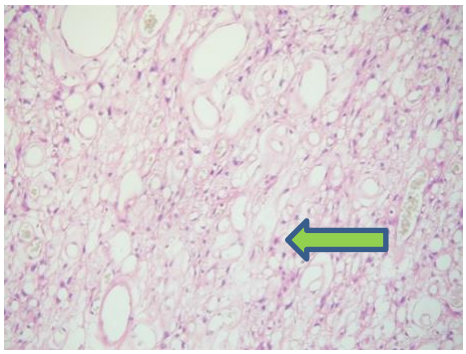

Figure 1.9 Microcystic meningioma.

1.7.5.7 Secretory meningioma

Characterised by the presence of focal epithelial differentiation in the form of intracellular lumina with periodic acid-Schiff (PAS) positive eosinophilic secretion which has been termed pseudopsammoma bodies. Carcinoembryonic antigen (CEA) is secreted from the tumour cells which are also positive for cytokeratin. Luminal secretions are CEA, therefore CEA blood levels can be measured as a biomarker and are seen to drop following resection of the tumour and raise in recurrence (Figure 1.10).

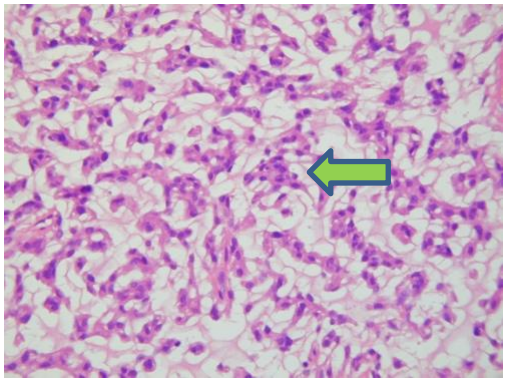

Figure 1.10 Secretory meningioma.

1.7.5.8 Lymphoplasmacyte-Rich

A rare type of WHO 1 meningioma, characterised by extensive inflammatory infiltrates on a background of meningiothelial, fibrous or transitional meningioma. Usually, abundant lymphoplasmacytic infiltration which sometimes include lymphoid follicle formation, which may obscure the meningiothelial components of the tumour requiring immunohistochemistry to rule out the lymphoproliferative process. Sometimes, macrophages become the predominant cell rather than the plasma cells, therefore, the term inflammation-rich meningioma has been suggested. Systemic abnormalities may be associated with this condition like hyperglobulinaemia and iron-refractory anaemia (Figure 1.11).

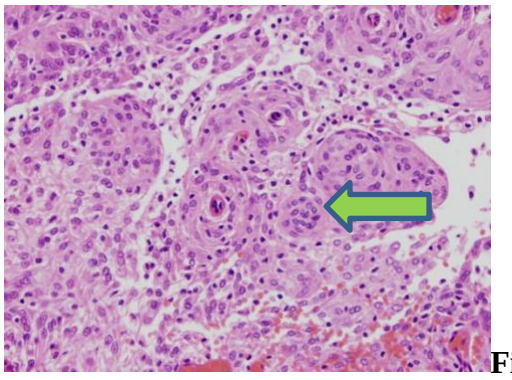

Figure 1.11 Lymphoplasmacyte-Rich meningioma.

1.7.5.9 Metaplastic meningioma

Another rare type exhibiting metaplastic changes that may be cartilaginous, osseous, xanthomatous, myxoid or lipomatous. The mesenchymal changes can be focal or widespread (Figure 1.12).

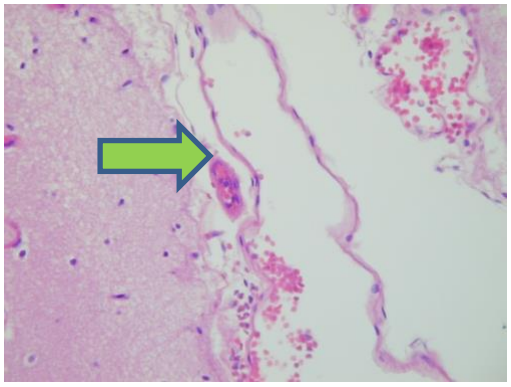

Figure 1.12 Lipomatous metaplastic meningioma.

1.7.5.10 Chordoid meningioma

A rare variant of meningioma that resembles chordoma. Characterised by cords of trabeculae of eosinophilic often vacuolated cells in a mucoid matrix. Typically, they are clinically large supratentorial tumours. They have a high rate of recurrence. They may, infrequently, be associated with haematological conditions such as anaemia or Castleman disease (Figure 1.13).

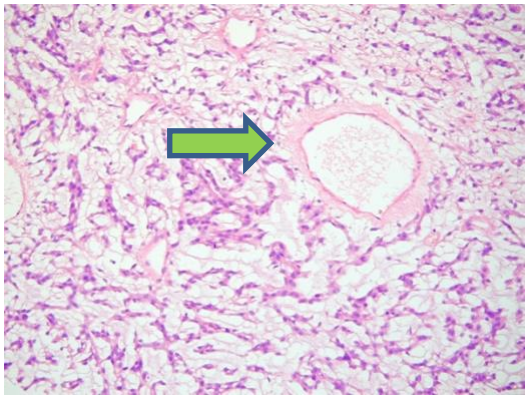

Figure 1.13 Chordoid meningioma.

1.7.5.11 Clear cell

A rare variant of meningioma with commonly no pattern or sheeting architecture and round to polygonal cells with clear, glycogen-rich cytoplasm and prominent perivascular and interstitial collagen. Clear cell meningioma has a tendency towards cerebellopontine angle location in the brain and the cauda equina region in the spine. It has also tendency to affect younger adults and children. There is also a family tendency, in association with SMRCE1 mutation. They generally carry aggressive behaviour with potential CSF seeding (Figure 1.14).

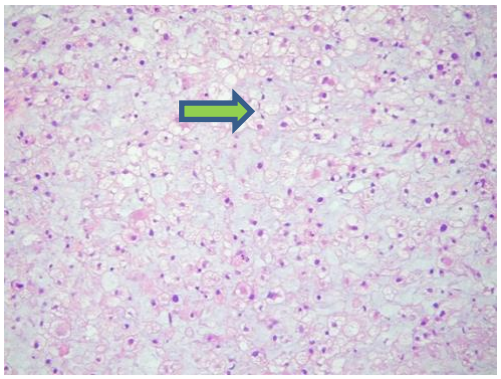

Figure 1.14 Clear cell Meningioma.

1.7.5.12 Atypical meningioma

Intermediate grade between benign and malignant forms. Under the microscope, they resemble their benign counterpart with increased mitotic activity ≥ 4/10HPF, brain invasion, or at least three of the following features: increased cellularity, small cells with high nuclear to cytoplasmic ration, prominent nucleoli, sheeting, and spontaneous necrosis (not induced by embolization or radiation). Brain invasion has to be associated with breach of pia. This is usually quantified by immunohistochemistry with glial fibrillary acidic protein (GFAP) to highlight the intervening brain parenchyma. Extension into the Virchow Robin space without pial breach is not brain invasion. Even benign meningioma can have brain invasion, nevertheless, they still carry a higher likelihood of recurrence. Therefore, brain invasion is a criterion of atypical meningioma (Louis *et al.*, 2016) (Figure 1.15).

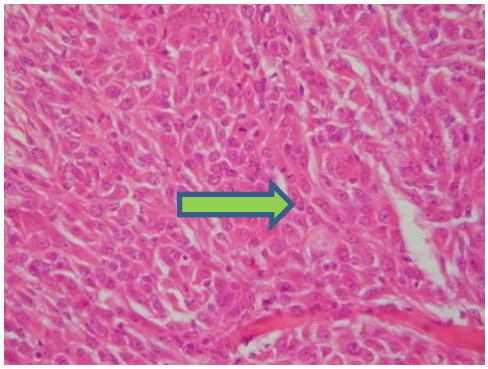

Figure 1.15 Atypical meningioma.

1.7.5.13 Papillary meningioma

A rare aggressive tumour. Characterised by the presence of perivascular pseudopapillary pattern constituting most of the tumour. They commonly occur in young adults. Brain invasion has been noted in 75% of cases. Extra cranial metastasis reported in 20% of cases mainly to lung (Figure 1.16).

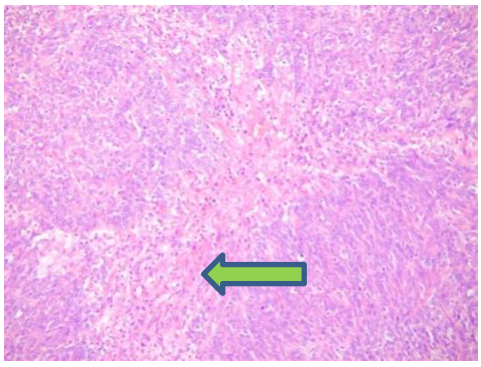

Figure 1.16 Papillary meningioma.

1.7.5.14 Rhabdoid meningioma

An uncommon aggressive variant, consists primarily of rhabdoid cells (plump cells with eccentric nuclei, open chromatin and a prominent nucleolus with abundant eosinophilic cytoplasm containing whorls of intermediate filaments. Sometimes other types of meningiomas

contain focal rhabdoid features; such cases are less aggressive and therefore, it is suggested that they are graded as normally but with the added with “rhabdoid features” (Figure 1.17).

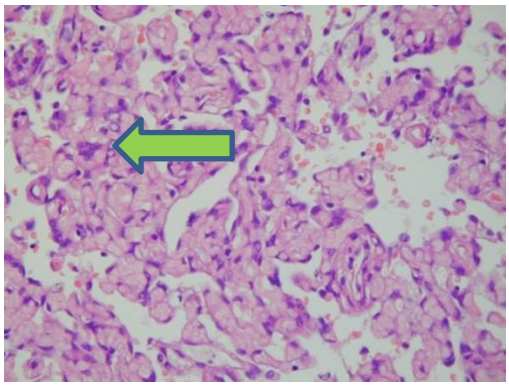

Figure 1.17 Rhabdoid meningioma.

1.7.5.15 Anaplastic(malignant) meningioma

Account for 1-3% of meningiomas. Exhibit malignant cytology similar to that of carcinoma, melanoma, or high-grade sarcoma and/or markedly elevated mitotic activity ≥ 20/10 HPF. Other features include extensive necrosis and a Ki-67 proliferation index >20% . Confirmation of the meningiothelial origin of cases with diffuse anaplasia often requires history of meningioma at the same location, immunohistochemistry and/or genetic support. Survival is usually 2-5 years depending on the degree of resection. However, surgical tumour margin can be a challenge since these is a lack of interphase between atypia and anaplasia (Figure 1.18).

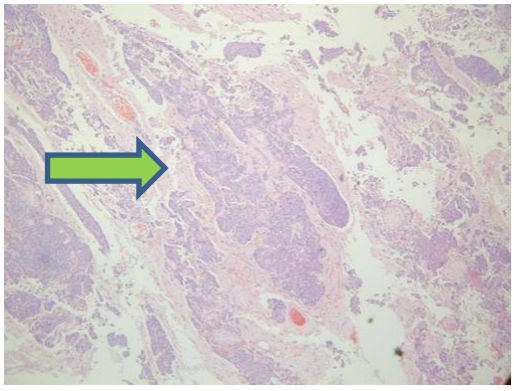

Figure 1.18 Anaplastic meningioma.

1.7.5.16 Other morphological variants

These are a wide group of other rare meningioma variants addressed collectively under one headline. The reason being, is the insufficient level of current evidence to support giving them a distinct variant. These include meningiomas with oncocytic, mucinous, sclerosing, whorling-sclerosing, GFAP-expressing and granulofilamentous inclusion-bearing features. Another pattern is the meningothelial rosette which is rarely seen secondarily in a variety of meningiomas.

The previously known pigmented meningioma, is currently described as melanocytoma. The international Agency for Research on Cancer (IARC) along with the International Society of Neuropathology (INS) produced a reference book based on the WHO classification, the blue book. Throughout the successive editions of the book, the evolutionary process in the tissue diagnosis throughout the years is evident. Tumour grade along with other factors can be used as a prognostic tool to predict overall patient prognosis and survival (Louis *et al.*, 2016).

1.8 Location

Cranial Meningiomas have been found in a number of locations. The location is important as it may bring different symptoms. Also, the ease of surgical removal and the chance of full excision can be successfully conducted in some locations more than others.

The majority of meningiomas are located in the convexity and this is followed by parasagittal meningioma and sphenoid wing meningioma. A list of tumour locations benign and malignant tumours and percentage relative to the total number is shown for each location in Table 1.4 (Rockhill *et al.*, 2007).

Table 1.4 A list of where benign and malignant meningioma have been located and ranked in terms of percentage relative to total number measured.

Tumour Location	**No. Benign (%)**	**No. Malignant (%)**
Convexity	60 (34)	7 (50)
Parasagittal	39 (22)	4 (29)
Sphenoid ridge	30 (17)	3 (21)
Lateral ventricle	10 (5)	0 (0)
Tentorium	7 (4)	0 (0)
Cerebellar convexity	9 (5)	0 (0)
Tuberculum sellae	7 (3)	0 (0)
Intraorbital	4 (2)	0 (0)
Cerebellopontine angle	4 (2)	0 (0)
Olfactory groove	6 (3)	0 (0)
Foramen magnum	1 (1)	0 (0)
Clivus	1 (1)	0 (0)
Other	1 (1)	0 (0)
Total	179	14

1.9 Clinical Course

Meningiomas are slow growing tumours, therefore, the clinical course quite commonly can be insidious (Rockhill *et al.*, 2007). Depending on the location and size it may cause symptoms with the most common of which being headache. Yet, patients may also present with an array of other symptoms such as seizures, visual disturbance, limb weakness, loss of smell sense, depression, or personality change. Some of the meningiomas are incidentally found on scanning for other causes. In fact, around 40% of meningiomas are asymptomatic (Yano *et al.*, 2006). Those who are symptomatic, there are two types of symptoms:

a) Non-specific: which are related to increase intracranial pressure that may lead to headache, nausea, vomiting or visual disturbance.
b) Specific: which are related to the location and size of meningioma like seizures, hemiplegia, ophthalmoplegia, gait disturbance and personality changes.

1.10 Diagnosis

Meningioma diagnosis is usually radiological. The lesions usually appear as a solitary extra axial mass with close proximity or contact to dura matter. The modality of choice for diagnosing meningioma is MRI scan, however, CT scan is also useful in high probability cases and when there is a need for good bony definition and for looking for calcification (Nagar *et al.*, 2007).

1.10.1 MRI scan

The modality of choice is MRI scan with gadolinium. Meningioma appears as isointense lesion on T1 weighted images before contrast and homogenous uptake of contrast. FLAIR (Fluid Attenuated Invention Recovery) sequence is useful in evaluating surrounding oedema. MR angio/venogram is a useful tool to define the vascular supply of the lesion and/or the invasion of the venous sinuses. DWI sequence can be useful in detecting dedifferentiation of WHO 2or 3 meningioma and the progression of tumour grade (Nagar *et al.*, 2007).

1.10.2 CT scan

Meningioma appears as a hypodense lesion on plain CT and bright after contrast. Useful in detecting bony definition and invasion. Calcification within the tumour is better visualised on a CT scan although it still can be detected on T2 weighted images MRI scan.

1.10.3 Cerebral Angiography

Not a diagnostic tool as such, nevertheless, it is a useful addition for the definition of vascular supply for surgical planning. It can also be used as a therapeutic tool; cerebral embolisation pre-operatively to reduce the surgical blood loss have become a standard practice in many centres. However, the EANO meningioma guidelines do not recommend it as a routine practice but only useful in selected cases (Goldbrunner *et al.*, 2016).

1.10.4 SPECT Octreotide Scintigraphy

This technique is based on the presence of high number of somatostatin receptors (SSr); however, it is a rarely used method, used to detect difficult tumours that do not appear well on an MRI scan such as lesions like skull base, optic sheath and tumour recurrence that are difficult to differentiate from scar tissue (Krenning *et al*., 1993).

1.11Management

Despite being the most common brain tumour, the level of evidence is low in the management of meningiomas. Hence, the meningioma task force of the European Association of Neuro- Oncology (EANO) reviewed the scientific literature and composed a framework of the best possible evidence-based recommendations for clinicians. In general, the following are the recommended treatment options. Large tumours may require treatment either surgically or with radiotherapy or both. Recurrence is possible with meningioma. Although the potential for recurrence is directly proportional to tumour grade, low-grade tumours do not confirm safety. There is no strong data to support the use of pharmacological agents in any of the aforementioned management plans (Venur *et al.*, 2018). The clinical dilemma stems from the

follow up arrangements that are required for the patients. NICE guidelines describe follow up arrangement for meningioma with clear follow up instructions up to 9 years however, at 9 years plus, the recommendation is to consider discharging the patient if there is no recurrence. In practice, some surgeons follow up patients for few years with interval MRI scans. Others prefer to follow up patients for life. In the absence of reliable indicator of recurrence, there is no strong basis to any particular longer term follow up arrangement given that even benign Meningiomas can recur (Pećina-Šlaus *et al.*, 2016). This commitment has its own financial, logistical, and patient convenience implications. Hence, the search for predictors for meningioma recurrence has been an increasingly popular research topic in recent years. There is an argument can be made for long term follow up and one against; although long term follow up or follow up for life can be safe and a surgeon, therefore, would unlikely miss a tumour recurrence or find it when it is too late. However, the counter argument is the implication of follow up arrangement from financial costs, from scans, to setting up clinics and travelling time and effort. Not to mention the anxiety patient can experience and go through waiting for the results and the MRI scan experience itself (scanxiety).

1.12 Predicting Recurrence

The recurrence of meningioma has been a clinical challenge for decades with meningioma recurrence being greater with partial resection and higher WHO grade. Nevertheless, a WHO 1 meningiomas still carry significant risk of recurrence (7-23% at 5 years, 20-39% at 10 years, and 24-60% at 15 years) (Marosi *et al.*, 2008). Moreover, recurrent meningioma carries higher risk of disease progression within shorter disease-free intervals (Marosi *et al.*, 2008).

As previously stated, the higher the WHO grade, the higher the chance of recurrence with poorer overall survival. A recent study looked into 49 cases of WHO grade 2 meningioma. Various factors were examined including patient and clinical characteristics, location, MRI findings, Simpsons grade, time to recurrence, and p53 expression. The authors found that atypical meningiomas tend to be associated with about an eight- fold increased risk of recurrence compared with WHO grade 1. They also concluded that if time to recurrence was less than 24 months, there was a threefold increase in further relapse and this group of patients needed closer follow up (Cao *et al.*, 2015).

Other researchers have focused on the radiological findings of the tumour to predict recurrence. A study that examined various independent variables of recurrence including MRI findings suggested that mushroom-shaped meningiomas were associated with a significantly higher incidence of recurrence compared to those with smooth borders. They also concluded that there is no relation between radiological calcification of the tumour and recurrence (Ildan *et al.*, 2007). Supporting this evidence, another paper reviewed 335 patients that underwent surgical resection of intracranial benign and atypical meningiomas also agreed with the higher recurrence rate in the radiological mushroom-shaped meningiomas. This radiological finding may represent the invasive potential of the tumour. More interestingly, they found that pial invasion was also a significant predictor of recurrence in both benign and atypical meningiomas (Nowak *et al.*, 2015).

Although there is an agreement to the role of radiotherapy in the overall survival of meningioma patients, timing of adjuvant radiotherapy has been extensively researched with mixed results in literature. Nevertheless, significant advances may only reap their rewards following the conduction of a prospective, randomized trial of early adjuvant radiotherapy (Klinger *et al.*, 2015).

1.12.1 Markers of meningioma prognosis

Since the turn of the century, scientists have been focusing more on the molecular and genetic profile of the tumour to predict the recurrence of meningioma as previously introduced in Section 1.4. Table 1.5 outlines some of the molecular changes associated with meningioma aggressiveness and recurrence.

Table 1.5 Possible molecular markers of meningioma prognosis.

Molecular Marker	Biological Role	Reference
CCNB1 overexpression	Cell cycle progression	Bie *et al.*, 2011
CDC2 overexpression	Cell cycle progression	Bie *et al.*, 2011
AKT2 overexpression	PI3K signalling	Wang *et al.*, 2014
HES1 overexpression	Notch pathway signalling	Yew *et al*., 2013
NF2 mutation	Growth regulation, motility	Alexiou *et al*., 2011
MKI67 over expression	Proliferation protein	Roser *et al.*, 2004
MDM2 loss of expression	p53 antagonist	Amatya *et al.*, 2004

Immunohistochemistry has provided an alternative route for the identification of a recurrence profile. Typical immunohistochemical targets within meningioma tissue include: EGFR E30, VEGF-A, HER2, IGF-1r, GHr, CD34, Caspase-3, PR and AR (Kärjä *et al.*, 2010). They also have audited a wide range of immunohistochemical targets within meningioma tissue with a view to the identification of protein expression patterns which may be associated with tumour aggressiveness and recurrence. Unfortunately, their findings were inconclusive.

1.12.2 Simpson Grade and its relevance to recurrence

In 1957, Donald Simpson published his famous paper regarding the recurrence of meningiomas after surgical treatment. In his paper, and after he reviewed the results of various centres, he linked the completeness of surgical resection with the chance of recurrence (Simpson, 1957). He then graded the degree of surgical resection which is still widely used in most neurosurgical centres as a tool to report the surgical level of excision and as a predictor of recurrence as shown in Table 1.6.

Table 1.6 A summary of the Simpson grade used to predict recurrence based on degree of surgical resection

Simpson Grade	Degree of surgical resection	Prediction of recurrence
Grade I	complete removal including resection of underlying bone and associated dura	9% symptomatic recurrence at 10 years
Grade II	complete removal and coagulation of dural attachment	19% symptomatic recurrence at 10 years
Grade III	complete removal w/o resection of dura or coagulation	29% symptomatic recurrence at 10 years
Grade IV	subtotal resection	44% symptomatic recurrence at 10 years
Grade V	simple decompression with or without biopsy	100% symptomatic recurrence at 10 years (small sample in original paper)

Recently, a number of papers have been published to challenge the value of Simpson grade. Oya *et al.* (2012) found that the value of the Simpson grade has been diluted recently with the emergence of other prognostic factors. A relatively similar conclusion was reached by Sughrue *et al.* (2010). Despite these challenges and the evolution of diagnostic and surgical techniques, more recent series still find the Simpson grade of value in predicting recurrence (Klinger *et al.*, 2015).

1.13 Research problem: meningioma verses meningiomas?

In the absence of high level evidence, the management and follow up arrangement for meningioma patients is highly driven by local tradition and experience-based practice. Although a number of studies are looking into predictor of recurrence, currently there is no single reliable predictor of recurrence with strong level of evidence. Therefore, clinicians have to individually tailor the therapy for each patient based on a number of factors including clinical, surgical, radiological, histopathological, genetic, and molecular factors. The number of variables that play a role in the aggressiveness of meningiomas, as well as the insidious nature of progression begs the question whether we are dealing with a single disease. Therefore, is it meningioma or meningiomas?

1.14 Aims and Objectives

The aim of the thesis was to assess the suitability of biospectroscopy sensor-based techniques to analyse the molecular signatures of meningioma and accurately segregate patients with benign meningioma into either high-risk group for recurrence or low risk group. Hence, this would ideally allow safe discharge of patients from the low-risk group after a period of follow up and identification of the high-risk patients to be followed up for life.

Objectives:

I. To be able to segregate the WHO Grade 1 meningioma from WHO Grade 1 recurrence using ATR-FTIR and Raman spectroscopy.
II. To be able to segregate the WHO Grade 2 meningioma from WHO Grade 1 using ATR-FTIR and Raman spectroscopy;

III. To be able to segregate the WHO Grade 2 meningioma from WHO Grade 1 recurrence using ATR-FTIR and Raman spectroscopy;

IV. To compare ATR-FTIR vs. Raman for distinguishing Grade 1vs Grade 1 recurrence vs 2

1.15 Justification and Novelty

The biospectrometry methods Raman and ATR spectroscopy were chosen for analysis of meningioma tumour samples. The reason for this choice was that these methods are cheap, reliable, fast, reproducible, simple and have been used extensively in other tumours such as ovarian cancers, gliomas. To our knowledge we are the first group working on segregating benign WHO 1 meningiomas into two separate subgroups determining which patients will require long-term follow-up based on predictions of aggressiveness and recurrence.

1.16 Hypothesis

The hypothesis is that the variability in the molecular phenotype of meningiomas (for example Grade 1, Grade 2, recurrence) are sufficiently different from one another that biospectrometry techniques are sensitive enough to stratify the patient into different categories based on the meningioma aggressiveness and potential for recurrence.

1.17 Spectroscopy

1.17.1 FTIR Spectroscopy

The infrared (IR) region encompasses radiation with wavenumbers ranging from about 12,800 to 10 cm^{-1} (0.78 to 1000 μm). This IR range is divided into three regions: the near-IR, the mid-IR, and the far-IR region (Skoog *et al.*, 2007). These three IR regions differ considerably and mid-IR is more commonly employed for analysing biological samples, since it detects fundamental vibration molecular modes (Skoog *et al.*, 2007).

IR spectroscopy is based on the vibrational motions of chemical bonds, like bending, stretching, rocking, and scissoring, where each type of vibration is specifically related to a vibrational energy level. The vibrational absorption of energy occurs only when the molecular bond has an electric dipole moment changeable by atomic displacement due to its vibration. The IR spectral signature then is transformed *via* a Fourier-transform (FT) filter to change the time domain to frequency, thus generating the term FTIR (Santos *et al.*, 2017). The mid-IR region also contains an important wavenumber range of biological interest, the so-called "biofingerprint" region (Baker *et al.*, 2014). The biofingerprint region covers the region between 900–18000 cm^{-1}, and it is where biomolecules such as lipids, carbohydrates, proteins, and nucleic acids absorbs IR light (Table 1.7) (Santos *et al.*, 2017).

Table 1.7 Main spectral features in the IR biofingerprint region (Santos *et al.*, 2017).

Wavenumber (cm^{-1})	**Assignment**	**Biomolecule category**
970	$\upsilon_s(\mathrm{R}-\mathrm{PO}_4^{2-})$ of phosphorylated proteins	Proteins
1030	$\upsilon(\mathrm{C}-\mathrm{O}/\mathrm{C}-\mathrm{C})$ of glycogen	Carbohydrates
1080	$\upsilon_s(\mathrm{PO}_2^-)$ of phosphodiester groups	Nucleic acids
1155	$\upsilon(\mathrm{C}-\mathrm{O})$	Carbohydrates
1225	$\upsilon_{as}(\mathrm{PO}_2^-)$ in RNA/DNA	Nucleic acids

1260	Amide III: $\upsilon(\mathrm{C}-\mathrm{N})$	Proteins
1550	Amide II: $\delta(\mathrm{N}-\mathrm{H})$ coupled to $\upsilon(\mathrm{C}-\mathrm{N})$	Proteins
1650	Amide I: $\upsilon(\mathrm{C}=\mathrm{O})$	Proteins
1750	$\upsilon(\mathrm{C}=\mathrm{C})$	Lipids

υ = stretching; υ_s = symmetric stretching; υ_{as} = asymmetric stretching; δ = bending

Figure 1.19 shows the main absorption bands for these biomolecules in the IR biofingerprint region (Kelly *et al.*, 2011). Changes in the IR signature for these biomolecules are associated with concentration changes (changes of band intensity) and changes of molecular configuration and neighbouring functional groups (band shifts towards higher or lower wavenumbers).

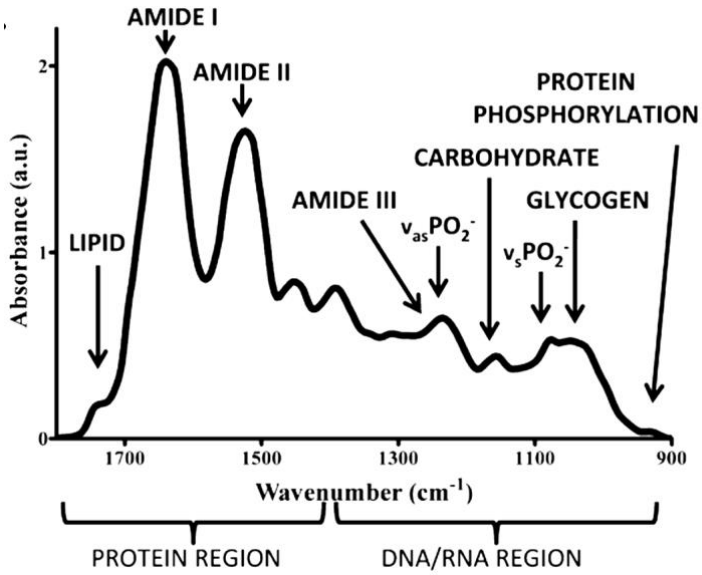

Figure 1.19 IR biofingerprint region with main absorption assignments. (Reprinted (adapted) with permission from Kelly *et al.*, 2011. Copyright 2011 American Chemical Society).

The FTIR spectrometer is composed of five main parts: (1) light source, (2) spectrograph, (3) sampling area, (4) detector, and (5) computer module. The (1) light source

generates IR radiation; the (2) spectrograph is an optical apparatus containing an interferometer, diffraction grating or prism to split the IR light into different wavenumbers; the (3) sampling area contains the sample apparatus to hold the sample while it is irradiated with IR light, being a transmittance or reflectance apparatus, such as an attenuated total reflection (ATR) module, in which a crystal (typically a diamond crystal) is placed in contact with the sample where internal reflections between the crystal and the sample material attenuates the IR signature; the (4) detector is responsible for capturing the diffracted IR light, thus generating an electrical response; and, the (5) computer module process the electrical signature transforming it into an interferogram and, by using the Fourier-transformation, into a spectrum. Figure 1.20 shows an example of an ATR-FTIR spectrometer.

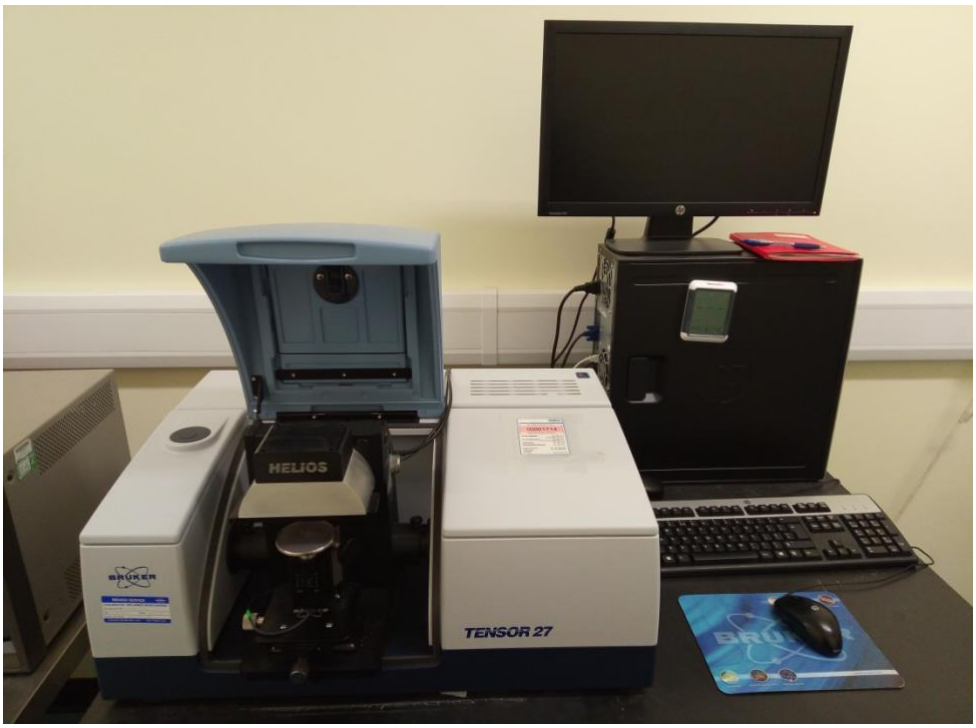

Figure 1.20 ATR-FTIR spectrometer.

1.17.2 Raman spectroscopy

Raman is an advanced spectroscopy technique capable of obtaining spectra from chemical species according to their polarizability changes and includes a wide range of polar and non-polar chemical bonds. When photons from a monochromatic light source interact with the chemical bonds present in a sample, these photons are then absorbed, hence, increasing the molecular vibrational energy. Thereafter, these photons are emitted, thus returning the molecule to their initial vibrational energy. This process itself is called elastic scattering and no Raman signature is observed. However, during this process, a small portion of molecules do not return to their initial vibrational energy stage, thus causing a difference between the absorbed and emitted energy. This is called inelastic scattering and it is the source of Raman spectroscopy. This inelastic scattering phenomenon occurs in less than 1% of absorbed photons, and it is divided into two subtypes of scattering: Stokes and anti-Stokes scattering. In the Stokes scattering, the molecule absorbs part of the energy from the incoming monochromatic light, thereby emitting a wavelength of less energy than the wavelength received; and, in the anti-Stokes scattering, the molecule emits a wavelength of higher energy than the wavelength from the monochromatic light. The anti-Stokes scattering happens under certain circumstances when the molecule is partially excited before absorbing the light from the monochromatic source. The Raman instrument then filters the elastic scattering so that only the Raman scattering is detected, and this signal is used to produce a spectrum containing peaks representing chemical information, and frequency shifts representing the wavenumbers from the Raman scattering (Santos *et al.*, 2017). Both Stokes and anti-Stokes scattering occur, but at room temperature, there is a low population of molecules in an initial excited energy state, thus the anti-Stokes signal is weaker than the Stokes signal, hence, many Raman spectrometers only records the Stokes scattering (Skoog *et al.*, 2007).

Raman is often used to analyse biological samples, since it is water transparent, that is, the water signal in Raman is very small so not masking the signal from the other chemical compounds below 3000 cm^{-1} (Skoog *et al.*, 2007). IR is sensitive to water; therefore, samples are often measured dry in IR spectroscopy to minimise the water interference; while Raman can measure all forms, including liquids or dry samples (Butler *et al.*, 2016). The Raman biofingerprint region is between 2000–500 cm^{-1}, and comprises mostly stretching vibrations for carbohydrates, lipids, proteins, and nucleic acids (Figure 1.21) (Kelly *et al.*, 2011).

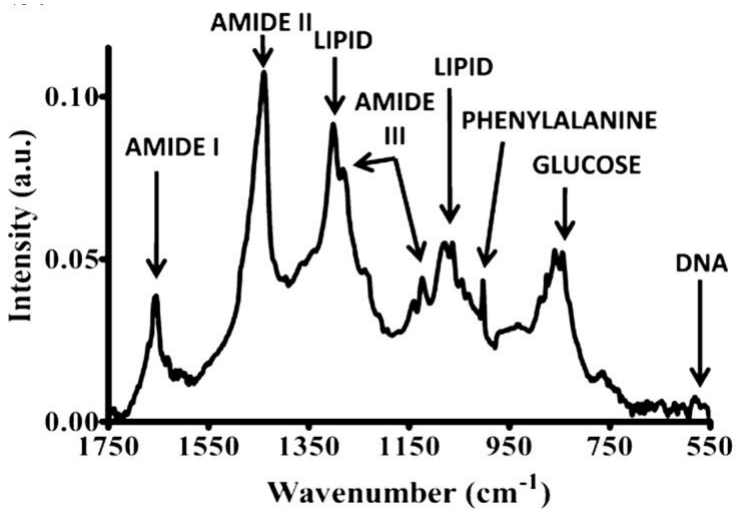

Figure 1.21 Raman biofingerprint region with main absorption assignments. (Reprinted (adapted) with permission from Kelly *et al.*, 2011. Copyright 2011 American Chemical Society).

The Raman spectrometer is composed of five main parts: (1) a monochromatic laser source, (2) a sampling area, (3) a spectrograph, (4) a detector, and (5) a computer module. The (1) monochromatic laser light, often in the visible or near-IR range, is used to excite the samples to virtual energy levels where the inelastic scattering occur; the (2) sampling area is usually a moving stage where the sample is affixed; the (3) spectrograph is usually a fixed diffraction grating; the (4) detector is a charge-coupled device (CCD) detector where the full spectrum is record with no need for a Fourier-transformation; and (5) the computer module is responsible

for converting the CCD detector signal into a spectrum. Figure 1.22 shows an example of a Raman spectrometer.

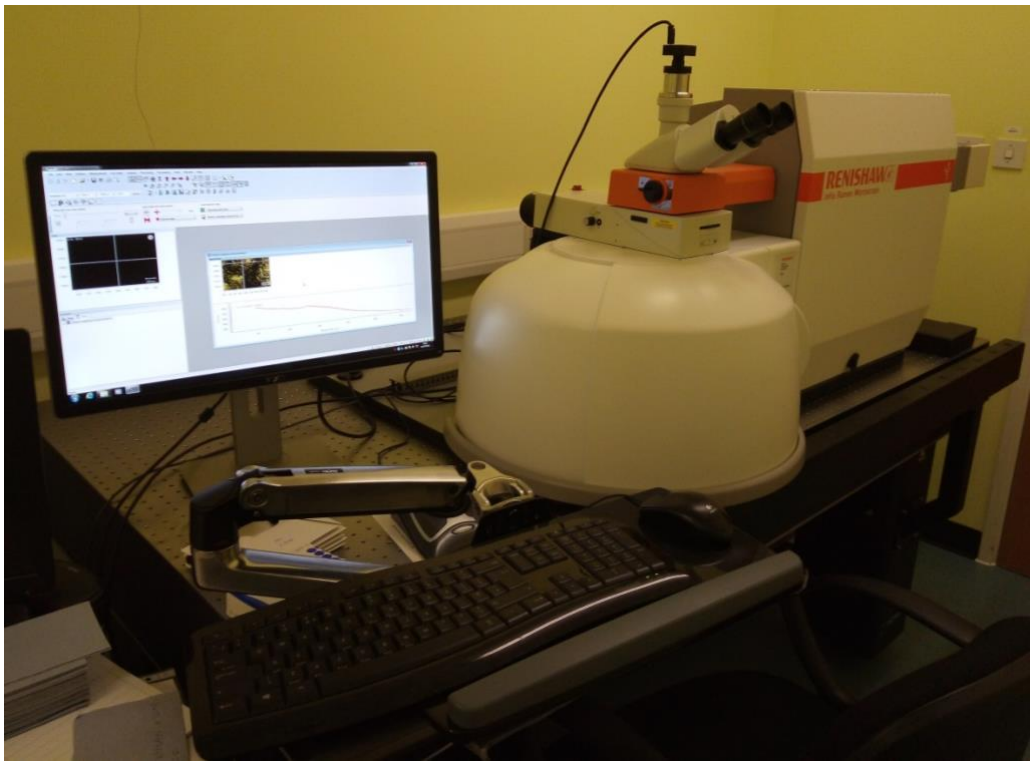

Figure 1.22 Raman spectrometer.

Both FTIR and Raman spectroscopy can be employed for the chemical analysis of tissue, where vibrational signals are obtained from biomolecules bonds that compose the tissue. These unique spectral features for FTIR and Raman make these spectroscopy techniques very attractive to determine chemical compositions of unknown substances. FTIR spectroscopy, as well as other molecular spectroscopy techniques such as liquid chromatography-mass spectrometry (LC/MS), nuclear magnetic resonance (NMR) spectroscopy, near-infrared (NIR), and Raman spectroscopy provide robust and supportive data about the sample chemical composition.

FTIR and Raman spectroscopies are a fast, low-cost, and reagent-free tool for cancer diagnostics (Bury *et al.*, 2019b). They are a high throughput technique which, together with multivariate analysis or machine learning algorithms, can be used for cancer detection in an automatic, quick, and easy fashion (Morais *et al.*, 2020b). For brain cancers specifically, knowing the tumour type or subtype is essential to start the correct patient treatment and reduce post-surgery risks (Bury *et al.*, 2019b), which ultimately will decrease patient mortality.

Although FTIR and Raman spectroscopy share similarities in the measurement of molecular vibration signatures. there are direct points that distinguish the origin, functionality, and the mode of identification of unknown materials by the two techniques (Poletto *et al.*, 2012). By principle, as mentioned earlier, FTIR is based on changes of dipole moment while Raman in changes of molecular polarizability, hence, the spectral profile for a same sample measured by both techniques will be substantially different, where signatures will be present at specific wavenumber positions in the FTIR spectrum while not in the Raman spectrum or vice-versa. Additionally, from a practical point-of-view, these techniques considerably diverge. FTIR is a more robust technique with less physical interfering however not as sensitive as Raman spectroscopy to analyse certain compounds, such as inorganic substances. Also, FTIR is greatly affected by water absorption. On the other hand, Raman is water-free and is a powerful technique to analyse inorganic substances, such as silica crystals and carbon nanotubes. However, Raman is highly affected by cosmic rays and fluorescence interfering which can mask the signal of interest. The latter is especially apparent when analysing coloured substances, hence, making it difficult to analyse these types of substances with Raman. Table 1.8 summarises the main differences between the two spectroscopic techniques.

Table 1.8 Main differences between Raman and IR spectroscopy.

Raman spectroscopy	**Infrared spectroscopy**
It is based on molecular polarizability changes, therefore, only molecules with variation of its polarizability after vibration are Raman active	It is based on changes of molecular dipole moments, therefore, only molecules that change their resultant dipole moment after vibration is IR active
Raman is a scattering technique where the light source is a monochromatic laser not necessarily in the IR region	IR is an absorption technique where the light source emits IR radiation
Raman is water-free	There are several water absorptions in the IR spectrum which may mask the information of interest. Spectra of aqueous samples should be analysed carefully.
Depending on the power or exposure time of the laser light, Raman can be destructive to the sample	IR is not destructive to the sample
Relative higher instrumentation cost	Relative lower instrumentation cost

Several studies have used FTIR or Raman spectroscopy to investigate biological samples, either tissues or biofluids, to detect brain cancers and their subtypes. Table 1.9 summarises the main findings along with the classification algorithms used to distinguish the samples. The classification performance to distinguish non-cancer from cancer samples or cancer subtypes seems to improve overtime. The results are dependent on the instrumentation, sample type and preparation and the algorithm used to process the spectral data. The results also look more promising when using mapping or imaging techniques instead of point-spectra, since spatially-distributed information carry more information about the sample specimen and often improves the classification (Morais & Lima, 2017; Morais *et al.*, 2019c). Also, the analyses were made using different algorithms which have weight in the classification outcomes. Often PCA-LDA (or just LDA), PLS-DA and SVM are used to discriminate and classify the samples.

Table 1.9 Overview of FTIR and Raman studies to investigate brain cancers.

Technique	Sample type	Samples	Algorithm	Main results	Reference
FTIR (Imaging)	Tissue (snap-frozen)	Non-cancer control Astrocytoma grade 3 Astrocytoma grade 2 Glioblastoma	GA-LDA	Sample discrimination at 89% accuracy	Steiner *et al.* (2003)
FTIR (Imaging)	Tissue (snap-frozen)	Non-cancer control Glioblastoma grade 4 Astrocytoma grade 3 Astrocytoma grade 2	ga_ors (Nikulin *et al.*, 1998)	Samples groups classified at 64% overall accuracy. Control tissues classified at 95% accuracy.	Beleites *et al.* (2005)
Raman (Mapping)	Tissue (snap-frozen)	Normal dura mater Meningioma	LDA PLS-DA	100% discrimination between normal and meningioma	Koljenović *et al.* (2005)
Raman (Resonance)	Tissue (snap-frozen)	Meningiomas Normal tissue Glioblastoma Acoustic neuroma Pituitary adenoma	PCA-SVM	90.9% sensitivity and 100% specificity to discriminate the samples	Zhou *et al.* (2012)
FTIR (ATR-FTIR) Raman	Tissue (FFPE)	Normal brain Meningioma Glioma Brain metastases LA AA GBM	LDA PCA-LDA	Statistically significant differences were found between the samples groups and subgroups	Gajjar *et al.* (2013)
FTIR (ATR-FTIR)	Serum	Non-cancer control Glioma (HGG, LGG)	SVM	Discrimination of non-cancer vs. gliomas with an average sensitivity of 93.75%, and average specificity of 96.53%	Hands *et al.* (2014)
FTIR (ATR-FTIR)	Serum	Non-cancer control Brain cancer Metastatic cancer Glioma (HGG, LGG) Meningioma	SVM	Samples groups and subgroups were classified with accuracies between 80-100%	Hands *et al.* (2016)

FTIR (ATR-FTIR)	Serum	Non-cancer control Brain cancers	Random forest 2D correlation analysis	Samples discriminated at 92.8% sensitivity and 91.5% specificity.	Smith *et al.* (2016)
Raman	Serum	Non-cancer control Meningiomas	PCA-LDA	Sample discrimination at 80% sensitivity and 92% specificity	Mehta *et al.* (2018)
Raman	Tissue (fresh, snap-frozen, FFPE)	Astrocytoma IDH-wildtype IDH-mutant Oligodendroglioma	PCA-LDA	79%-94% sensitivity and 90-100% specificity to classify glioma subtypes and 91% sensitivity and 95% specificity to classify IDH mutation.	Livermore *et al.* (2019)
FTIR (ATR-FTIR)	Serum	Non-cancer control Brain cancers	PLS-DA SVM Random forest	Non-cancer vs. cancer discrimination at 91% sensitivity and specificity. Glioblastoma vs. lymphoma discrimination at 90.1% sensitivity and 86.3% specificity.	Cameron *et al.* (2019)
FTIR (ATR-FTIR)	Serum	Non-cancer control Brain cancers	SVM	Sample discrimination at 93.2% sensitivity and 92.8% specificity	Butler *et al.* (2019)
Raman (Handheld)	Tissue (FFPE, fresh)	Normal brain LGG HGG Meningiomas Metastases Lymphoma	PCA-LDC	Samples groups were discriminated at 90.3–99.6% accuracies (fresh tissue) and 88.0–99.5% accuracies (FFPE)	Bury *et al.* (2019a)
FTIR (ATR-FTIR)	Plasma	Normal brain HGG LGG Meningioma Brain metastases	PCA-LDC SVM	Discrimination between normal vs. LGG vs. HGG at 100% accuracy Discrimination between all groups at 97% accuracy	Bury *et al.* (2019b)
FTIR (ATR-FTIR) Raman	Tissue (fresh-frozen)	Normal brain Glioma Meningioma	PCA-QDA GA-QDA	Non-tumour *vs.* tumour were correct classified at	Bury *et al.* (2020)

				94% (Raman) and 97.2% (FTIR)	
FTIR (ATR-FTIR, Synchrotron)	Serum Tissue	Gliomas (IDH1 mutated and wild-type)	LDA PLS-DA	Discrimination of IDH1 samples using serum at 69.1% accuracy; and, using tissue at 82.9% accuracy	Cameron *et al.* (2020a)
FTIR (ATR-FTIR)	Serum	Non-cancer control Glioblastoma Meningioma Lymphoma Metastasis	PLS-DA SVM Random forest	Discrimination between controls vs. brain cancers at sensitivity and specificity above 90%. Discrimination brain lesions with accuracies above 80%.	Cameron *et al.* (2020b)

ATR-FTIR: attenuated total reflection Fourier-transform infrared spectroscopy. FFPE: formalin-fixed paraffin-embedded. LA: low-grade astrocytoma. AA: anaplastic astrocytoma. GBM: glioblastoma multiforme. HGG: high-grade glioma. LGG: low-grade glioma. GA-LDA: genetic algorithm linear discriminant analysis. LDA: linear discriminant analysis. PLS-DA: partial least squares discriminant analysis. PCA-LDA: principal component analysis linear discriminant analysis. PCA-SVM: principal component analysis support vector machines. SVM: support vector machines. PCA-QDA: principal component analysis quadratic discriminant analysis. SPA-QDA: successive projections algorithm quadratic discriminant analysis. PCA-LDC: principal component analysis linear discriminant classifier. GA-QDA: genetic algorithm quadratic discriminant analysis.

These algorithms are applied after pre-processing the samples spectra, where peak removal (*e.g.*, cosmic rays removal in Raman spectroscopy), selection of specific spectral regions of interest (*e.g.*, biofingerprint region), smoothing, baseline corrections, derivatives, and normalisation procedures are performed to reduce spectral interferences and improve the signal-to-noise ratio of the spectra (Morais *et al.*, 2019d; Morais *et al.*, 2020b). The final classification is then made by these machine learning algorithms where a training set of samples feeds the model while a test set validates them towards external samples prediction (Morais *et al.*, 2020b). It is important to test different types of algorithms since results may vary depending on the algorithm chosen and validated them by cross-validation and external predictions in order to avoid overfitting, which may lead to false results (Morais *et al.*, 2020b).

CHAPTER 2 | MATERIAL AND METHODS

2.1 Samples and Patient Demographics

2.1.1 Sample collection

Ninety-nine formalin-fixed paraffin-embedded (FFPE) brain tissue samples (70 WHO grade 1 meningiomas, 24 grade WHO 2 meningiomas and 5 grade 1 meningiomas that re-occurred) were used for analysis. The 99 patients in the cohort were divided into a wide range of age group ranging from 36 to 92 years at presentation. 73 F and 26 M. F:M ratio= 2.8:1. Mean age 59 and standard deviation = 11.67. Samples were collected at 10-µm-thick and sourced from the Brain Tumour Northwest (BTNW) biobank (National Research Ethics Service ethics approval NRES14/EE/1270). A dedicated neuropathologist examined the paraffin blocks for the patients and decided on which one to proceed with. There was a discission of whether we map the samples should be mapped out or not. We elected to keep the samples unmapped to be more representative of a real-world setting taking advantage of the number of points or spectra we are taking for each patient. Therefore, the same method can be replicated in real time for future application. All experiments were approved by the STEMH (Science, Technology, Engineering, Medicine and Health) ethics committee at the University of Central Lancashire (STEMH 917). The patient demographics are show in Table 2.1 and H&E images for all samples are available upon reasonable request to the BTWN biobank.

Table 2.1 Patient demographics for the FFPE brain tissue samples used in the study.

Patient Number	WHO grade	Sex	Age	Histology
1	1	F	67	Fibrous

2	1	F	63	Transitional
3	1	M	47	Transitional
4	1	F	70	Transitional
5	1	F	35	Transitional
6	1	F	54	Fibrous
7	1	F	53	Fibrous
8	1	F	43	Transitional
9	1	F	55	Transitional
10	1	M	70	Transitional
11	1	F	50	Transitional
12	1	M	55	Transitional
13	1	F	59	Meningothelial
14	1	F	65	Meningothelial
15	1	M	47	Syncytial
16	1	M	58	Secretory type
17	1	M	55	Secretory type
18	1	M	55	Secretory type
19	1	F	76	Transitional
20	1	F	50	Meningothelial
21	1	F	41	Meningothelial
22	1	F	41	Transitional
23	1	M	69	Transitional
24	1	F	48	Fibrous
25	1	F	52	Fibrous
26	1	F	54	Secretory type
27	1	M	88	Fibrous
28	1	F	86	Fibrous
29	1	F	76	Fibrous
30	1	M	76	Syncytial

31	1	F	59	Fibrous
32	1	F	52	Fibrous
33	1	F	36	Fibrous
34	1	F	50	Fibrous
35	1	F	73	Syncytial
36	1	F	58	Transitional
37	1	M	60	Transitional
38	1	M	55	Transitional
39	1	F	55	Secretory type
40	1	F	60	Transitional
41	1	F	76	Transitional
42	1	M	50	Microcystic
43	1	F	54	Secretory type
44	1	F	54	Secretory type
45	1	M	61	Secretory type
46	1	F	48	Transitional
47	1	F	77	Secretory type
48	1	F	42	Fibrous
49	1	F	68	Transitional
50	1	F	65	Transitional
51	1	F	81	Meningothelial
52	1	F	54	Secretory type
53	1	M	59	Syncytial
54	1	F	72	Fibrous
55	1	F	44	Angiomatous
56	1	F	64	Psammomatous
57	1	F	66	Transitional
58	1	F	51	Transitional
59	1	F	50	Meningothelial

60	1	F	58	Meningothelial
61	1	F	47	Secretory type
62	1	F	61	Fibrous
63	1	F	53	Fibrous
64	1	F	52	Secretory type
65	1	F	51	Secretory type
66	1	F	57	Meningothelial
67	1	F	58	Fibrous
68	1	M	39	Angiomatous
69	1	F	43	Fibrous
70	1	F	57	Fibrous
71	2	F	67	Atypical
72	2	F	67	Atypical
73	2	M	62	Chordoid
74	2	M	62	Atypical
75	2	M	57	Atypical
76	2	F	76	Atypical
77	2	F	66	Chordoid
78	2	F	53	Chordoid
79	2	F	58	Atypical
80	2	M	40	Chordoid
81	2	M	80	Atypical
82	2	F	44	Atypical
83	2	F	44	Atypical
84	2	F	60	Atypical
85	2	F	60	Atypical
86	2	M	66	Atypical
87	2	F	57	Chordoid
88	2	F	92	Atypical

89	2	F	79	Atypical
90	2	M	75	Atypical
91	2	F	75	Atypical
92	2	F	62	Atypical
93	2	F	62	Atypical
94	2	M	61	Atypical
95	1-recurrence	M	69	Transitional
96	1-recurrence	F	50	Transitional
97	1-recurrence	M	55	Transitional
98	1-recurrence	F	59	Meningothelial
99	1-recurrence	F	65	Meningothelial

2.1.2 Sample measurement

The FFPE brain tissue samples were placed onto aluminium-covered glass slides for spectroscopy measurement. Aluminium foil is an inexpensive way to improve the signal-to-noise ratio in both FTIR and Raman spectroscopy (Paraskevaidi *et al.*, 2018). For FTIR measurements, the samples were affixed onto a moving platform with the sample facing up against the ATR crystal, defined by an internal reflective element (diamond crystal) with an approximately area of 250 µm × 250 µm. De-parrafinisation was performed prior to commencing measurements using local protocols with xylene and ethanol (Baker *et al.*, 2014). Moving the platform upward allowed the specimen to contact the diamond crystal for spectral acquisition at 8 cm^{-1} spectral resolution, over the range between 4000 and 400 cm^{-1} (32 co-addition scans). Ten spectra were collected per tissue sample in different random locations to minimise bias. After each sample, the ATR crystal was cleaned with distilled water and a new

background spectrum was acquired to take into account ambient changes before the next sampling. The time to measure each sample was approximately 10 min.

A similar protocol was performed on Raman spectroscopy, where the same samples were analysed. For Raman, each tissue sample was affixed onto a moving platform (sample facing up toward the laser and acquisition lens) and microspetroscopy imaging was performed with an acquisition area of approximately 100 µm × 50 µm. The instrument was calibrated with a reference silica standard before measurements and no contact between the sample material and the acquisition lens was made. Samples were measured at 50× magnification using a 785 nm laser (50% laser power (150 mW)) and 0.1 s exposure time over the spectral range between 780 and 1858 cm^{-1}. The spectra were acquired using the StreamHR^{TM} imaging technique (high-confocality mode) with a grid area of 42 x 28 pixels, resulting in 1176 spectra for each tissue image (1 cm^{-1} data spacing). The laser power was set relatively high to ensure a good signal-to-noise ratio. To minimise any potential photodamage to the sample, the laser exposure was set to only 0.1 s. Moreover, no damage was visually observed in the samples after measurements. The sample acquisition time was approximately 8 min for each sample.

2.2 Data Analysis

2.2.1 Pre-processing

The first step to analyse spectral data is to pre-process them in order to maximise the signal-to-noise ratio and minimise any spectral interference. The protocol for pre-processing follows four steps depending on whether some corrections are needed or not: (1) to minimise random noise; (2) to remove light scattering effects; (3) to correct baseline distortions; and, (4) to

normalize the spectra by a spectral feature or a factor (Morais *et al.*, 2020b). The (1) random noise is minimised after employing smoothing techniques, such as the Savitzky-Golay smoothing filter, where a moving window filter out the noise through a polynomial curve fitting procedure. The (2) light scattering is rarer to occur in both FTIR and Raman spectroscopy, but when present, it is characterised by a large distortion of the baseline acting differently for each sample, so the spectra shift in the y-axis in a systematic fashion. It is corrected by filters such as the standard normal variate (SNV) or the multiplicative scatter correction (MSC). The (3) common baseline distortions are frequent in FTIR and Raman spectroscopy, and they are corrected by filters that create an artificial baseline for the spectral spectroscopy, so an artificial baseline is fitted to the peaks which after subtraction makes the real baseline close to zero. The (4) spectral normalization is made to correct problems associated with unknown concentration changes or changes of tissue thickness, and it will depend on the application of interest. Usually, Amide I or vector normalization is performed. Amide I normalization is made when Amide I peak is not an important feature in the data, so this peak will have maximum absorption of 1 for all spectra and the remaining will be scaled accordingly. The vector normalization is made when Amide I may be an important peak, so the spectra is normalized against the spectral norm instead. Operations in 2D and 3D computer graphics are often performed using copies of vectors that have been normalized i.e., converted to unit vectors. The normalized vector of X is a vector in the same direction but with norm (length) 1. It is denoted X^^ and given by

$$X^{\wedge\wedge}=(X)/(|X|),$$

where |X| is the norm of X. It is also called a unit vector.

Another common pre-processing used to smooth out and correct baseline problems in the spectra are the Savitzky-Golay derivatives, which simultaneously perform steps (1) to (3) and can enhance small spectral differences between the samples (Morais *et al.*, 2020b).

The data analysis for the FTIR tissue spectra was performed within MATLAB R2014b environment (MathWorks, Natick, USA) using the Classification Toolbox for MATLAB (Ballabio & Consonni, 2013). The biofingerprint spectra (1800-900 cm^{-1}) were pre-processed by Savitzky-Golay 2^{nd} derivative (window of 7 points, 2^{nd} order polynomial fit) and vector normalisation for correcting random noise, baseline distortions and to improve the signal-to-noise ratio (Baker *et al.*, 2014; Morais et al., 2019d). The Raman images were converted into suitable .txt files using the Renishaw WiRE software and processed using MATLAB R2014b with lab-made routines. All the samples' images were pre-processed by cosmic rays (spikes) removal, Savitzky-Golay smoothing (window of 15 points, 2^{nd} order polynomial fitting) and asymmetric least squares baseline correction. The window size in the Savitzky-Golay smoothing was determined visually by testing different window sizes, where the smallest window size that removed random noise and kept the same spectral shape and intensity without smoothing-out relevant spectral peaks was chosen.

2.2.2 Exploratory Analysis

After pre-processing, the spectra are analysed using exploratory analysis tools. The most common exploratory analysis tool employed to analyse spectral data is the Principal Component Analysis (PCA) (Bro & Smilde, 2014). In PCA, the pre-processed data are decomposed into a few numbers of factors called Principal Components (PCs) responsible for most of the variance within the original dataset. The PCs are orthogonal to each other and are

built in a decreasing order of explained variance, so that the first PC explains most of the variance, followed by the second PC and so on (Morais *et al.*, 2020b). Each PC is composed of scores, representing the variance on the sample direction, and loadings, representing the variance on the wavenumber direction. The PCA decomposition takes the form shown in Equation 2.1 (Bro & Smilde, 2014):

$$\mathbf{X} = \mathbf{T}\mathbf{P}^{\mathbf{T}} + \mathbf{E} \qquad \text{(Equation 2.1)}$$

where **X** is a matrix containing the mean-centred pre-processed spectral data; **T** is a matrix containing the PCA scores for a determined number of PCs; **P** is a matrix containing the PCA loadings for a determined number of PCs; **E** is a residual matrix; and the superscript **T** represents the matrix transpose operation.

The scores can be used to identify similarities/dissimilarities between the samples through the visualisation of clustering patterns, while the loadings can be used to discover the wavenumbers of highest importance responsible for clustering segregation. Besides being an unsupervised tool for exploratory analysis, PCA also acts as a tool for data reduction and feature extraction, since the PCA scores can be used to represent the sample input data instead of the full spectrum in further machine learning algorithms, and the PCA loadings can be used for biomarkers detection (Morais et al., 2019d). In addition, the PCA results can be used for outlier detection by means of a Hotelling's T^2 *versus* Q residuals test (Morais et al., 2019d).

For imaging data, besides PCA, another important technique is the Multivariate Curve Resolution Alternating Least Squares (MCR-AL) (Jaumot *et al.*, 2015). MCR-ALS assumes a bilinear model that is the multi-wavelength extension of the Beer-Lambert's law. It

decomposes an experimental matrix **D** into concentration and spectral profiles as shown in Equation 2.2 (Jaumot *et al.*, 2015):

$$\mathbf{D} = \mathbf{C}\mathbf{S}^{\mathbf{T}} + \mathbf{E} \qquad \text{(Equation 2.2)}$$

where **C** is a matrix containing the concentration profiles for a determined number of pure components in **D**; **S** is a matrix containing the spectral profiles for the pure components in **D**; and **E** is a residual matrix.

MCR-ALS can remove noise and physical/chemical interferences from the spectral matrix **D**, and allow one to recover the pure concentration and spectral profiles of the components that make the spectral matrix **D**. Therefore, MCR-ALS is very useful to handle image data since it allows the reconstruction of image maps based on the recovered concentration profiles, where one can identify spatial and chemical differences between the samples being imaged (Prats-Montalbán *et al.*, 2011).

2.2.3 Feature Selection and Classification

In addition to PCA, there are other tools commonly used to extract useful information from the spectral data in order to reduce their size and to simplify biomarker discovery. These are the tools of feature selection, where specific spectral features responsible for maximising the segregation between groups of samples are selected from the dataset in a supervised fashion. Two common tools for feature selection are the Successive Projections Algorithm (SPA) (Soares *et al.*, 2013) and the Genetic Algorithm (GA) (McCall, 2005). SPA is an iterative forward feature selection algorithm operating by minimising the collinearity in the spectral dataset, thus selecting wavenumbers whose information content is minimally redundant; and, GA is an iterative combinational algorithm inspired by Mendelian genetics, where a set of initial wavenumbers undergo selection, cross-over combinations, and mutations until the fittest

set of wavenumbers are found (Morais *et al.*, 2020b). The selected wavenumbers by SPA and GA are then used to identify possible biomarkers, and they are also used as input data for classification.

The full spectra, PCA scores or SPA/GA selected wavenumbers can be used for classification using machine learning techniques. The simplest of these techniques belong to the area of discriminant analysis, in which the most commonly used algorithms are the linear discriminant analysis (LDA), quadratic discriminant analysis (QDA) and partial least squares discriminant analysis (PLS-DA) (Dixon & Brereton, 2009; Brereton & Lloyd, 2014). LDA and QDA are supervised discriminant analysis techniques based on a Mahalanobis distance calculation between the samples, where the main difference between these techniques is that in LDA the calculation assumes that the classes have similar variance structure, thus using a pooled covariance matrix; while in QDA, the calculation is made assuming the classes with different variance structures, thus using the variance-covariance matrix for each class individually (Morais & Lima, 2018). The data input for LDA or QDA must be the PCA scores or the SPA/GA selected wavenumbers, since these algorithms are not capable of working with the full spectral data.

PCA-LDA and PCA-QDA are supervised discriminant analysis algorithms based on a PCA model followed by a LDA or QDA classifier (Morais & Lima, 2018). Initially, the pre-processed spectral data is reduced by PCA to a small number of PCs accounting for the majority of the data explained variance (Bro & Smilde, 2014). Then, a LDA or QDA model is built using the PCA scores, where the samples are assigned to classes based on a Mahalanobis distance calculation (Morais & Lima, 2018). The LDA (L_{ic}) and QDA (Q_{ic}) classification scores can be calculated in a non-Bayesian form as shown in Equations 2.3 and 2.4 (Dixon & Brereton, 2009; Morais & Lima, 2018):

$$L_{ic} = (\mathbf{x}_i - \bar{\mathbf{x}}_c)^{\mathrm{T}} C_{\mathrm{pooled}}^{-1} (\mathbf{x}_i - \bar{\mathbf{x}}_c) \quad \text{(Equation 2.3)}$$

$$Q_{ic} = (\mathbf{x}_i - \bar{\mathbf{x}}_c)^{\mathrm{T}} C_c^{-1} (\mathbf{x}_i - \bar{\mathbf{x}}_c) \quad \text{(Equation 2.4)}$$

where $\mathbf{x}_i$ is a vector containing the scores for sample *i*; $\bar{\mathbf{x}}_c$ is the mean vector for class *c*; C_{pooled} is the pooled covariance matrix; and C_c is the variance-covariance matrix of class *c*. C_{pooled} and C_c are calculated as shown in Equation 2.5 and 2.6 (Morais & Lima, 2018):

$$C_{\mathrm{pooled}} = \frac{1}{n} \sum_{c=1}^{C} n_c C_c \quad \text{(Equation 2.5)}$$

$$C_c = \frac{1}{n_c - 1} \sum_{i=1}^{n_c} (\mathbf{x}_i - \bar{\mathbf{x}}_c)(\mathbf{x}_i - \bar{\mathbf{x}}_c)^{\mathrm{T}} \quad \text{(Equation 2.6)}$$

in which *n* is the total number of samples in the training set; *C* is the total number of classes; and n_c is the number of samples in class *c*.

In addition to the regular PCA-LDA and PCA-QDA, their three-dimensional versions (3D-PCA-LDA and 3D-PCA-QDA) can be applied to classify imaging data (Morais *et al.*, 2020a). In these algorithms, the 3D imaging data for each sample are firstly arranged into a 4D hypercube with sizes $s \times n \times m \times k$, where *s* represents the number of samples, *n* the number of pixels in the *x*-axis, *m* the number of pixels in the *y*-axis, and *k* the number of spectral wavenumbers. This hypercube is then analysed by 3D-PCA as described by Morais *et al.* (2019c), where scores and loadings are obtained for each pixel position (*x*, *y*) in the image surface. The scores represent the variance on the sample direction, thus being used to assess similarities and dissimilarities between the samples; and the loadings represent the variance on the wavenumber direction, thus being used to identify possible discriminant wavenumbers.

This procedure reduces the hypercube size into two 4D structures: (1) $s \times n \times m \times t$, where *t* represents the scores according to the number of principal components (PCs), which in this case were 2 PCs; and (2) $p \times n \times m \times k$, where *p* represents the loadings on each PC, which

in this case were 2 loadings arrays. Then, the scores and loadings are averaged on the *n* and *m* directions generating a single scores array for each sample ($s \times t$) and two loadings arrays with *k* wavenumbers ($p \times k$). The scores are used as input for linear and quadratic discriminant analysis (LDA and QDA) as described in equations 2.3 and 2.4, and the loadings are used to extract important wavenumbers related to class separation.

PLS-DA is a supervised feature extraction and classification algorithm where partial least squares (PLS) is applied to the pre-processed spectral data reducing the original wavenumbers to a small number of latent variables (LVs). Then, a linear discriminant classifier is used for classifying the groups (Brereton & Lloyd, 2014). PLS-DA usually performs better than PCA-LDA, therefore it is commonly employed as a benchmark technique for spectral classification (Morais *et al.*, 2020b). PLS-DA works similarly to PCA-LDA, where the spectral data are firstly decomposed by PLS, however, differently from PCA-LDA, the input class label for the training samples (*e.g.*, +1 or -1) are used during this process, since PLS maximises the covariance between the spectral information and the sample category. The samples are then assigned to classes based on a straight line that divides the classes' spaces (Brereton & Lloyd, 2014).

Another commonly used technique for classification is the Support Vector Machines (SVM) (Cortes & Vapnik, 1995). SVM is a very powerful machine learning algorithm where the full spectral dataset or the PCA scores and SPA/GA selected variables can be used for classification. SVM works firstly by transforming the data space into a feature space by means of a kernel function which is often non-linear. Then, a linear decision boundary is fit between the closest samples to the border of each class (these samples are called support vectors), hence classifying the samples according to this boundary (Brereton & Lloyd, 2010; Morais *et al.*, 2020b). Although being an algorithm that often outperforms LDA, QDA or PLS-DA, SVM is very susceptible to overfitting, so it must be used with caution (Morais *et al.*, 2019b).

Overfitting is often used in statistics, data science and machine learning. It refers to a modelling error that occurs when a function corresponds too closely to a particular set of data. Consequently, overfitting may fail to fit new data, in return may affect the accuracy of predicting future observations. It is easy to spot overfitting when the training set results are far more promising that the test set. To avoid overfitting there are several techniques can be applied, such as, cross validation, adding more data, dividing the training data, etc. If the problem persists, then to avoid this particular algorithm and try a different one. It is useful to spot this problem early in the data analysis. Algorithms that are known to be prone for this kind of problem should be avoided or used with caution.

2.2.4 Biomarkers Identification

The biomarkers identification is made by discovering the spectral markers responsible for class differentiation. There are ways to find these spectral markers, such as the PCA loadings, SPA and GA selected wavenumbers, or even the PLS-DA regression coefficients. Also, there is the combination of these outputs in order to see spectral markers that reoccur in different algorithms. The best spectral markers are those that gave the best classification performance in unknown test samples, and they can be validated by calculating some statistics such as *p*-values per wavenumber and the difference-between-mean (DBM) spectra, where one can see the absorbance effect on each of the spectral markers wavenumbers. The biomarker assignment is then made based on reference tables (Movasagui *et al.*, 2007; Movasagui *et al.*, 2008), where each wavenumber is related to a specific vibration and molecular functional group.

2.2.5 Statistical Validation

In order to validate the classification results, unknown test samples must be evaluated with each classification model and algorithm. To have reliable results, the classification performance of test samples must be high and close to the performance obtained during training and cross-validation, in which known samples are used (Morais *et al.*, 2020b). The test set is usually extracted from the experimental set of samples measured in the laboratory by using a sample selection algorithm, such as the Kennard-Stones (KS) (Kennard & Stone, 1969) or MLM (Morais et al., 2019e) method. These test samples do not participate in any of the data analysis steps and are only used at the end when the classification models are already built. The main metrics used to evaluate the test performance and consequently the algorithm performance are the accuracy (AC), sensitivity (SENS) and specificity (SPEC) (Morais *et al.*, 2020b). These metrics are calculated as shown in Equations 2.7, 2.8 and 2.9.

$$\mathrm{AC}\ (\%) = \frac{\mathrm{TP}+\mathrm{TN}}{\mathrm{TP}+\mathrm{FP}+\mathrm{TN}+\mathrm{FN}} \times 100 \qquad \text{(Equation 2.7)}$$

$$\mathrm{SENS}(\%) = \frac{\mathrm{TP}}{\mathrm{TP}+\mathrm{FN}} \times 100 \qquad \text{(Equation 2.8)}$$

$$\mathrm{SPEC}\ (\%) = \frac{\mathrm{TN}}{\mathrm{TN}+\mathrm{FP}} \times 100 \qquad \text{(Equation 2.9)}$$

where TP stands for true positives, TN stands for true negatives, FP for false positives and FN for false negatives.

Accuracy, sensitivity, and specificity values close to 100% is an indication of a perfect model prediction, as well as receiver operating characteristics (ROC) curves with the area under the curve (AUC) close to 1.0. To qualitatively assess the model performance taking into consideration the AUC, the general understanding is: 0.5 – no sample discrimination; between

0.7 and 0.8 – acceptable results; between 0.8 and 0.9 – excellent results; and, above 0.9 – outstanding results (Mandrekar, 2010).

CHAPTER 3 | FTIR SPECTROSCOPY ANALYSIS

3.1 Results

This study is composed of 99 patients separated into 3 groups: grade 1 meningiomas (*n* = 70, 700 spectra), grade 2 meningiomas (*n* = 24, 240 spectra) and grade 1 meningiomas that re-occurred (*n* = 5, 50 spectra) (see Table 2.1). Sample groups were pre-defined based on histopathologic evidence before spectral acquisition. Figure 3.1 shows an example of H&E slide for WHO Grade 1 and Grade 2 meningiomas. The raw and pre-processed (Savitzky-Golay 2nd derivative and vector normalisation) IR spectra for the tissue samples are shown in Figure 3.2a-c and in the Appendix B (Figures B1 and B2).

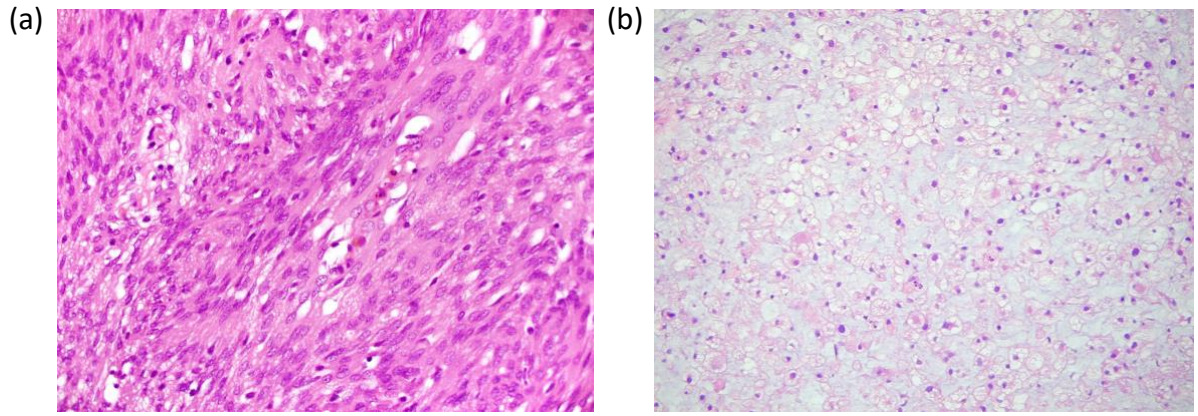

Figure 3.1 H&E slides. (a) WHO grade 1 meningioma (transitional meningioma); and (b) WHO grade 2 meningioma (clear cell).

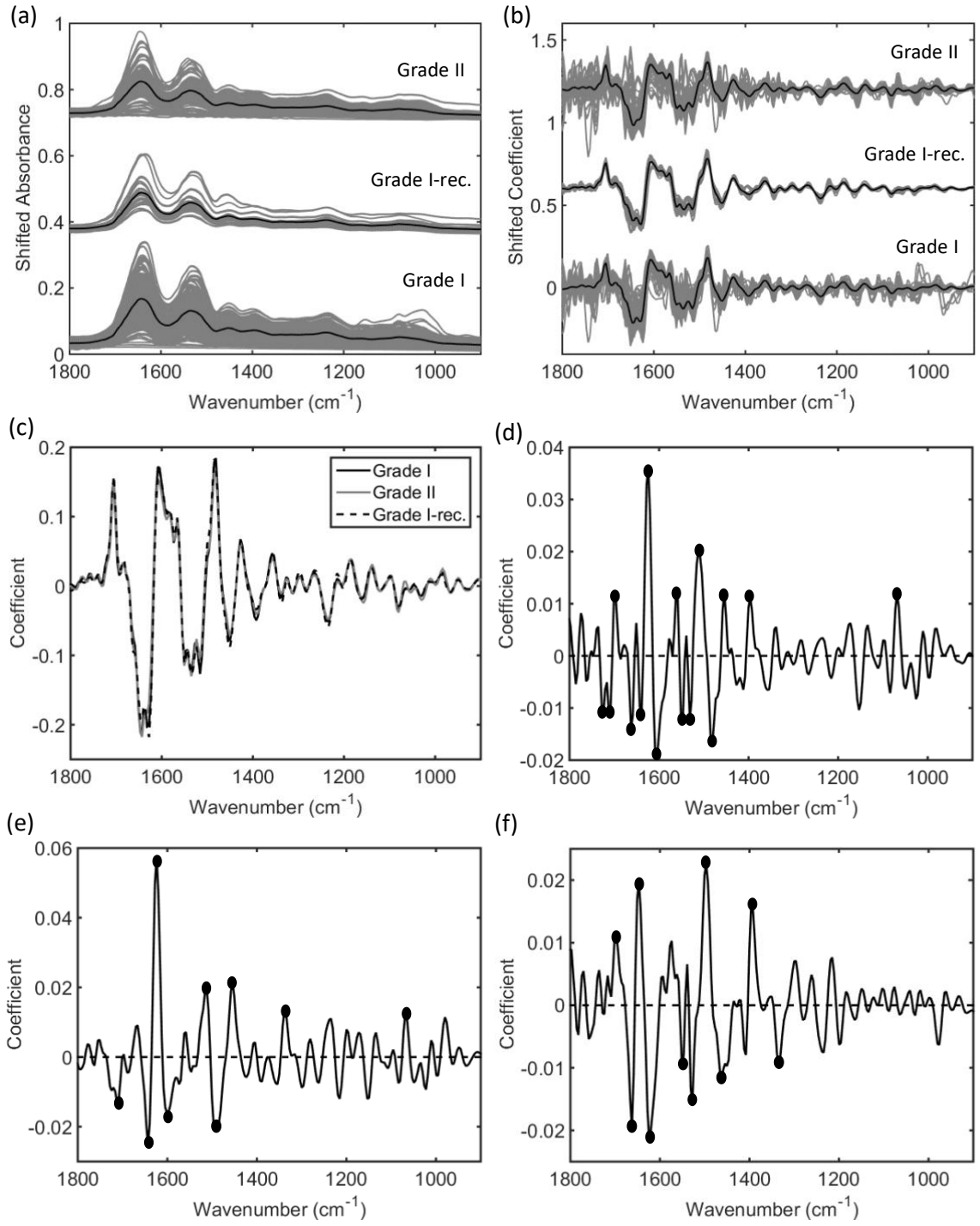

Figure 3.2 Infrared spectra for meningioma tumour samples (grade 1, grade 1–recurrence, and grade 2) in the biofingerprint region (1800–900 cm^{-1}). (a) Raw spectra and (b) pre-processed spectra (Savitzky-Golay 2nd derivative and vector normalisation), where black line: mean spectrum. (c) Mean spectrum for each class overlaid. (d) Difference-between-mean (BDM) spectrum for Grade 2 (+) *vs.* Grade 1(-) meningiomas; (e) difference-between-mean (BDM) spectrum for Grade 2 (+) *vs.* Grade 1-recurrence (-) meningiomas; and (f) difference-between-

mean (BDM) spectrum for Grade 1-recurrence (+) *vs.* Grade 1(-) meningiomas, where solid dots represent spectral wavenumbers with absolute coefficients >0.01.

Grade 1 and Grade 2 meningiomas exhibit higher levels of variability in comparison with Grade 1 recurrence most likely due to the smaller number of Grade 1 recurrence spectra (Figure 3.2b). The difference-between-mean (DBM) spectrum for Grade 2 (+ coefficients) and Grade 1(- coefficients) meningiomas is shown in Figure 3.2d, where 15 spectral markers were found with absolute coefficient intensity >0.01: 1725 cm^{-1} (lower coefficient in Grade 2, C=O stretching in fatty acids), 1708 cm^{-1} (lower coefficient in Grade 2, C=O stretching in thymine), 1698 cm^{-1} (higher coefficient in Grade 2, C_2=O stretching in guanine), 1663 cm^{-1} (lower coefficient in Grade 2, C=O stretching in cytosine), 1639 cm^{-1} (lower coefficient in Grade 2, Amide I), 1624 cm^{-1} (higher coefficient in Grade 2, base carbonyl stretching and ring breathing mode in nucleic acids), 1604 cm^{-1} (lower coefficient in Grade 2, adenine vibration in DNA), 1562 cm^{-1} (higher coefficient in Grade 2, ring base), 1550 cm^{-1} (lower coefficient in Grade 2, Amide II), 1530 cm^{-1} (lower coefficient in Grade 2, C=N and/or C=C stretching), 1512 cm^{-1} (higher coefficient in Grade 2, C-H in-plane bending), 1481 cm^{-1} (lower coefficient in Grade 2, Amide II), 1454 cm^{-1} (higher coefficient in Grade 2, asymmetric methyl deformation), 1396 cm^{-1} (higher coefficient in Grade 2, symmetric CH_3 bending of the methyl groups of proteins), and 1068 cm^{-1} (higher coefficient in Grade 2, C-O stretching in ribose) (Movasaghi *et al.*, 2008). Nine spectral markers with absolute coefficients >0.01 were found in the DBM spectrum for Grade 2 (+ coefficients) *vs.* Grade 1 recurrence (- coefficients) (Figure 3.2e): 1708 cm^{-1} (lower coefficient in Grade 2, C=O stretching in thymine), 1643 cm^{-1} (lower coefficient in Grade 2, Amide I), 1624 cm^{-1} (higher coefficient in Grade 2, base carbonyl stretching and ring breathing mode in nucleic acids), 1600 cm^{-1} (lower coefficient in Grade 2, C=O stretching in lipids), 1512 cm^{-1} (higher coefficient in Grade 2, C-H in-plane bending), 1490 cm^{-1} (lower

coefficient in Grade 2, C=C and/or in-plane C-H bending), 1454 cm^{-1} (higher coefficient in Grade 2, asymmetric methyl deformation), 1339 cm^{-1} (higher coefficient in Grade 2, collagen), and 1068 cm^{-1} (higher coefficient in Grade 2, C-O stretching in ribose) (Movasaghi *et al.*, 2008). The DBM spectrum for Grade 1recurrence (+ coefficients) *vs.* Grade 1(- coefficients) meningiomas (Figure 3.2f) indicates 10 spectral markers with absolute coefficients >0.01: 1698 cm^{-1} (higher coefficient in Grade 1 recurrence, C_2=O stretching in guanine), 1663 cm^{-1} (lower coefficient in Grade 1 recurrence, C=O stretching in cytosine), 1647 cm^{-1} (higher coefficient in Grade 1 recurrence, Amide I), 1624 cm^{-1} (lower coefficient in Grade 1 recurrence, base carbonyl stretching and ring breathing mode in nucleic acids), 1550 cm^{-1} (lower coefficient in Grade 1 recurrence, Amide II), 1527 cm^{-1} (lower coefficient in Grade 1 recurrence, C=N and/or C=C stretching), 1496 cm^{-1} (higher coefficient in Grade 1 recurrence, C=C stretching and/or C-H bending), 1460 cm^{-1} (lower coefficient in Grade 1 recurrence, asymmetric CH_3 bending in collagen), 1393 cm^{-1} (higher coefficient in Grade 1 recurrence, symmetric CH_3 bending in proteins), and 1335 cm^{-1} (lower coefficient in Grade 1 recurrence, CH ring deformation in polysaccharides or pectin) (Movasaghi *et al.*, 2008).

The spectral data underwent chemometric analysis by means of PCA-LDA, as a first discriminant attempt, and then by PLS-DA as a final and best discriminant model. The following comparisons were investigated: (1) grade 1 *vs.* grade 2 meningioma; (2) grade 1 *vs.* grade 1 meningiomas that re-occurred; and, (3) grade 2 *vs.* grade 1 meningiomas that re-occurred. An outlier test was performed using the Hotelling's T^2 *versus* Q residuals test and no spectral outlier was observed in the dataset (Appendix B, Figure B3). Thereafter, the samples for grade 1 and grade 2 meningiomas were divided into training (70% of samples) and validation (30%) sets using the Kennard-Stone uniform sample selection algorithm (Kennard & Stone, 1969). Cross-validated PCA-LDA and PLS-DA were built using venetian blinds cross-validation with 10 data splits.

3.1.1 Grade 1 vs. Grade 2 meningiomas

The training set was used for model construction, while the validation set for final model evaluation. PCA-LDA was applied to the spectral data using 10 PCs (98% explained variance, Appendix B, Figure B5), where training and validation accuracies were estimated at 89% and 71%, respectively (Table 3.1). Although reasonable accuracies and sensitivity (89% in the validation set), the specificity in validation was 20%, indicating that many grade 1 meningiomas were predicted as grade 2. PLS-DA was then applied to the spectral data as a most powerful alternative for class differentiation. PLS-DA model was built with 11 LVs (93% spectral explained variance, Appendix B, Figure B5), generating accuracies of 97% and 79% in the training and validation sets, respectively (Table 3.1). The sensitivity and specificity in the validation set were equal to 80% and 73%, respectively, with an area under the curve (AUC) value equal to 0.82, which indicates a good classification model.

Table 3.1 Quality metrics for PCA-LDA and PLS-DA models to distinguish grade 1 *vs.* grade 2 samples.

Algorithm	Dataset	Accuracy (%)	Sensitivity (%)	Specificity (%)
PCA-LDA	Training	89%	98%	62%
	Validation	71%	89%	20%
PLS-DA	Training	97%	96%	99%
	Validation	79%	80%	73%

The PLS-DA discriminant function (DF) graph and receiver operating characteristic (ROC) curve to discriminate grade 1 and grade 2 meningiomas are depicted in Figure 3.3. PLS-DA coefficients were used to extract biomarkers information through an automatic peak detection algorithm that sought for the 8 most relevant peaks representing the wavenumbers with highest absolute coefficients (Table 3.2).

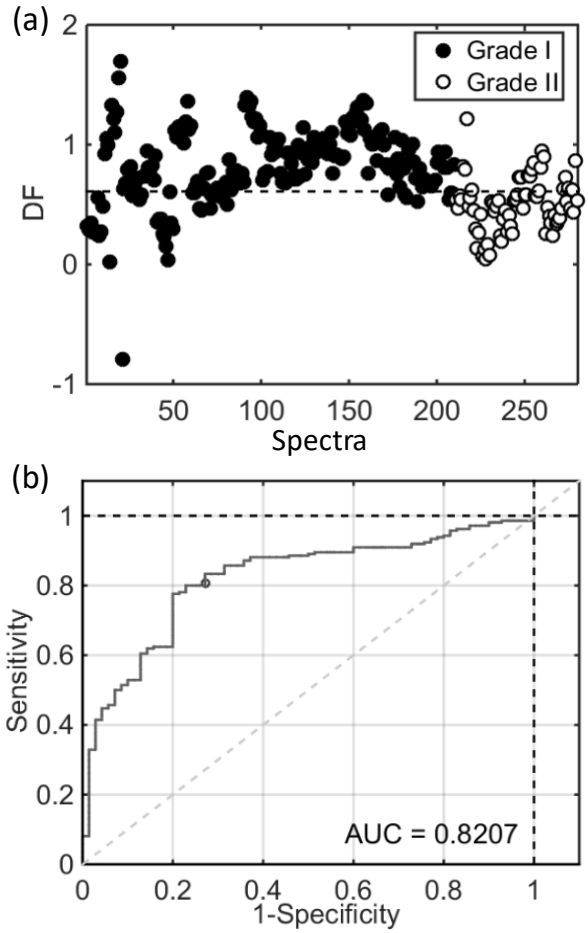

Figure 3.3 PLS-DA results to distinguish grade 1 *vs.* grade 2 meningiomas. (a) Discriminant function (DF) plot for samples' spectra; (b) receiver operating characteristic (ROC) curve, where AUC stands for area under the curve.

Table 3.2 Spectral markers identified by PLS-DA in order to discriminate grade 1 and grade 2 meningiomas. *P*-value calculated by an ANOVA test.

Wavenumber (cm^{-1})	Tentative assignment	Relative intensity[a]	*P*-value[b]
1651	Amide I	↓	0.035 (*)
1593	NH_2 adenine	↓	$<10^{-7}$ (**)
1546	Amide II	↑	0.637
1500	δ(CH) in-plane	↑	$<10^{-4}$ (**)
1454	$\delta(CH_3)$ asymmetric	↓	$<10^{-13}$ (**)
1377	ν(C-O)	↓	0.030 (*)
1227	$\nu_{as}(PO_2^-)$	↓	0.051
1122	ν(C-O) in carbohydrates	↑	0.014 (*)

[a]↑ = higher intensity in grade 2 meningioma; ↓ = lower intensity in grade 2 meningioma. [b]*P*-value <0.05 considered statistically significant (*) and *P*-value <0.001 considered statistically highly significant (**). δ: bending, ν: stretching, ν_{as}: asymmetric stretching.

3.1.2 Grade 1 vs. Grade 1 meningiomas that re-occurred

Cross-validated PCA-LDA was applied to the spectral data using 17 PCs (97% explained variance) (Appendix B, Figure B7), where both training and validation accuracies were estimated at 95% (Table 3.3). Although excellent values of accuracy and sensitivity (99%), the specificity is again low in validation (32%), indicating that many grade 1 meningiomas were predicted as grade 1 that reoccurred. PLS-DA was applied to the spectral data with 17 LVs (95% spectral explained variance) (Appendix B, Figure B7), generating accuracies of 96% and 94% in the training and validation sets, respectively (Table 3.3).

Table 3.3 Quality metrics for PCA-LDA and PLS-DA models to distinguish grade 1 *vs.* grade 1 recurrence samples.

Algorithm	Dataset	Accuracy (%)	Sensitivity (%)	Specificity (%)
PCA-LDA	Training	95	99	34
	Validation	95	99	32
PLS-DA	Training	96	96	100
	Validation	94	94	94

The sensitivity and specificity in the validation were both equal to 94%, with an AUC value equal to 0.98, which indicates an almost perfect classification. The PLS-DA DF graph and ROC curve to discriminate grade 1 and grade 1 recurrence meningiomas are depicted in Figure 3.4. The wavenumbers with highest absolute PLS-DA coefficients are depicted in Table 3.4.

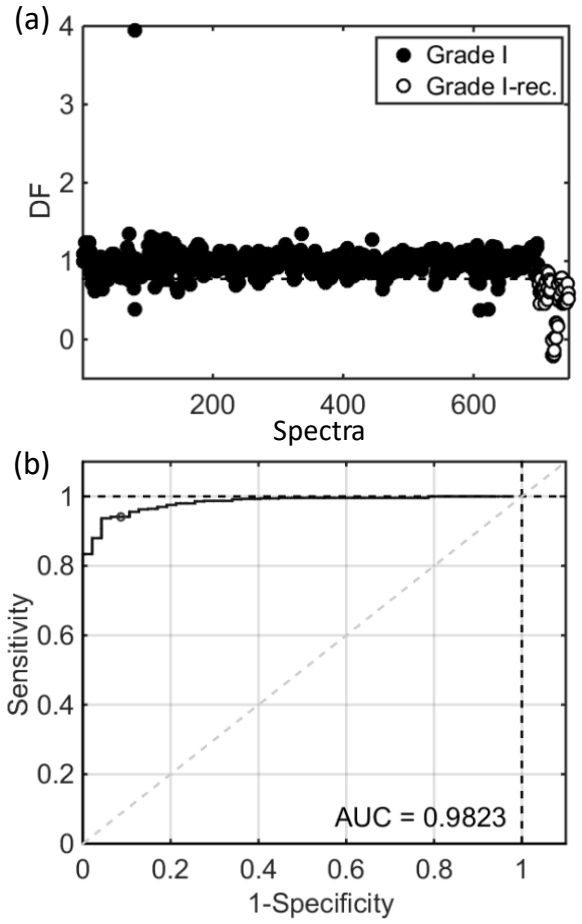

Figure 3.4 PLS-DA results to distinguish grade 1 *vs.* grade 1 recurrence meningiomas. (a) Discriminant function (DF) plot for samples' spectra; (b) receiver operating characteristic (ROC) curve, where AUC stands for area under the curve.

Table 3.4 Spectral markers identified by PLS-DA in order to discriminate grade 1 and grade 1 recurrence meningiomas. *P*-value calculated by an ANOVA test.

Wavenumber (cm^{-1})	Tentative assignment	Relative intensity[a]	*P*-value[b]
1755	ν(C=O) in lipids	↓	$<10^{-3}$ (**)
1693	Amide I (antiparallel β-sheet)	↑	$<10^{-3}$ (**)
1477	$\delta(CH_2)$ in lipids	↓	0.229
1423	$\delta(CH_2)$ in polysaccharides	↑	0.722
1400	$\nu_s(COO^-)$ in amino acids (aspartate, glutamate)	↓	$<10^{-5}$ (**)
1369	ν(C-N) in cytosine and guanine	↓	0.542
1346	$\delta(CH_2)$ in collagen	↓	0.940
1246	$\nu_{as}(PO_2^-)$	↑	$<10^{-4}$ (**)

[a]↑ = higher intensity in grade 1recurrence meningioma; ↓ = lower intensity in grade 1recurrence meningioma. [b]*P*-value <0.05 considered statistically significant (*) and *P*-value <0.001 considered statistically highly significant (**). δ: bending, ν: stretching, ν_s: symmetric stretching, ν_{as}: asymmetric stretching.

3.1.3 Grade 2 vs. Grade 1 meningiomas that re-occurred

Cross-validated PCA-LDA was applied to the spectral data using 12 PCs (96% explained variance) (Appendix B, Figure B9), where both training and validation accuracies were estimated at 90% (Table 3.5). Once more, the specificity of PCA-LDA is highly affected (45%), although the good accuracies and sensitivity (99%). PLS-DA was applied to the spectral data with 13 LVs (95% spectral explained variance) (Appendix B, Figure B9), generating accuracies of 99% and 97% in the training and validation sets, respectively (Table 3.5).

Table 3.5 Quality metrics for PCA-LDA and PLS-DA models to distinguish grade 2 *vs.* grade 1recurrence samples.

Algorithm	Dataset	Accuracy (%)	Sensitivity (%)	Specificity (%)
PCA-LDA	Training	90	99	47
	Validation	90	98	45
PLS-DA	Training	99	98	100
	Validation	97	97	100

The sensitivity and specificity in the validation were both equal to 97%, with an AUC value equal to 0.99, which indicates a close to perfect classification. The PLS-DA DF graph and ROC curve to discriminate grade 2 and grade 1 recurrence meningiomas are depicted in Figure 3.5, where the wavenumbers with highest absolute PLS-DA coefficients are depicted in Table 3.6.

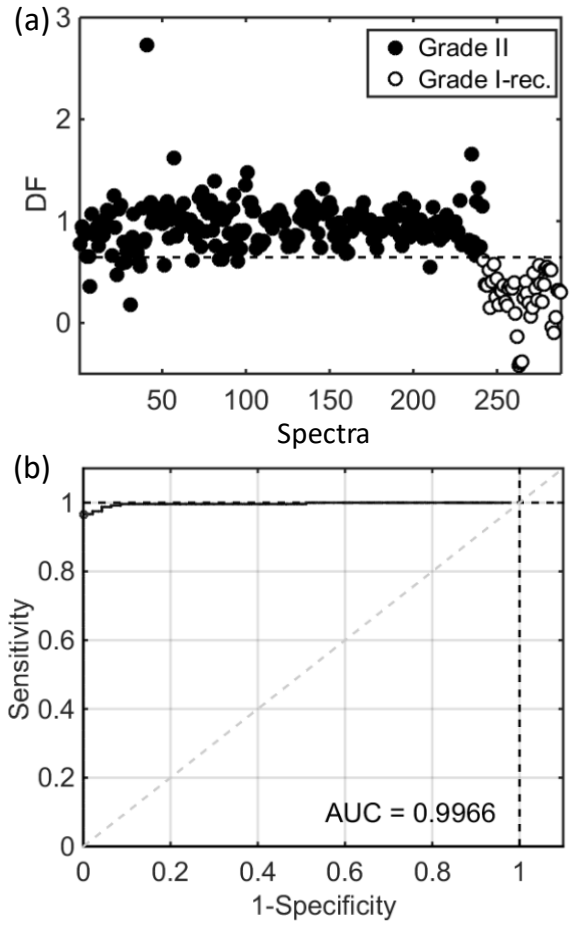

Figure 3.5 PLS-DA results to distinguish grade 2 *vs.* grade 1 recurrence meningiomas. (a) Discriminant function (DF) plot for samples' spectra; (b) receiver operating characteristic (ROC) curve, where AUC stands for area under the curve.

Table 3.6 Spectral markers identified by PLS-DA in order to discriminate grade 2 and grade 1 recurrence meningiomas. *P*-value calculated by an ANOVA test.

Wavenumber (cm^{-1})	**Tentative assignment**	**Relative intensity[a]**	***P*-value[b]**
1639	Amide I	↓	0.579
1597	NH_2 adenine	↑	0.001 (*)
1547	Amide II	↓	0.425
1523	ν(C=N)	↑	0.018 (*)
1454	$\delta(CH_3)$ asymmetric	↑	$<10^{-3}$ (**)
1265	$\nu_{as}(PO_2^-)$	↑	$<10^{-11}$ (**)
1242	Amide III	↑	$<10^{-5}$ (**)
1122	ν(C-O) in carbohydrates	↓	0.251

[a]↑ = higher intensity in grade 1recurrence meningioma; ↓ = lower intensity in grade 1recurrence meningioma. [b]*P*-value <0.05 considered statistically significant (*) and *P*-value <0.001 considered statistically highly significant (**).

3.2 Discussion

Normal and tumour brain tissues have been previously discriminated using IR or Raman spectroscopy (Gajjar *et al.*, 2013), where neoplastic tissue (meningioma, glioma, and brain metastasis) was found to be statically significantly different from normal tissue using PCA-LDA as the multivariate spectral analysis technique. Hands *et al.* (2016) reported serum diagnostic of brain tumours using ATR-FTIR spectroscopy with support vector machines (SVM) with sensitivity of 89.4% and specificity of 78.0% to distinguish cancerous from non-cancerous samples, and sensitivity of 82.1% and specificity of 75.0% to distinguish glioma from meningioma tissue. Bury *et al.* (2019) reported the use of ATR-FTIR spectroscopy to analyse plasma samples in order to distinguish non-cancer from different cancerous brain samples. Normal and meningioma samples were differentiated with 87% accuracy using PCA-LDA and 95% accuracy using SVM; and meningioma samples were diagnosed among several

groups of samples (normal, high-grade glioma, low-grade glioma, and brain metastasis) with an accuracy of 63% using PCA-LDA and 100% using SVM.

Herein, WHO grade 1 and grade 2 meningiomas were discriminated with 79% accuracy in the validation set (80% sensitivity, 73% specificity, AUC = 0.82) using PLS-DA, a simpler and less susceptible method to overfitting than SVM; indicating a satisfactory clinical performance taking into consideration the complexity of the data obtained, as demonstrated by the patient demographics in Table 2.1, and the inherent spectrochemical complexity of tissue samples. Although having high accuracies and sensitivities, the lower specificities of the PCA-LDA models indicate that these models are skewed towards the bigger class size, so the model is classifying the samples from this class more accurately (high sensitivity) than the samples from the smaller class (low specificity). The accuracy is influenced by the class size, so it tends to follow the sensitivity. The PLS-DA models, on the other hand, have a better consistency between sensitivity and specificity, thus indicating no overfitting. The statistically significant spectral markers were mainly associated with proteins (Amide I, Amide II), carbohydrates (ν(C-O)), and DNA/RNA functional groups (NH_2 adenine, $\nu_{as}(PO_2^-)$) (Table 3.2). Proteins play an important role in the molecular pathways for meningiomas, where, for example, integrin exhibits different expression profile within different grades of meningioma (Abbritti *et al.*, 2016). In addition, Amide I, Amide II, and carbohydrate absorptions have been associated with differences between normal and meningioma tissues (Bury et al., 2019b), and δ(CH), $\delta(CH_3)$, ν(C-O) and $\nu_{as}(PO_2^-)$ have been found related to spectral markers associated with brain tumours in general (Hands *et al.*, 2016). These findings indicate that IR spectroscopy allied with chemometrics could be used to aid clinical differentiation of grade 1 and grade 2 meningioma tumours in a non-destructive, fast, and sensitive way.

"Grade 1" and "Grade 1 recurrence" were found to be clearly different, in which a discriminant performance of 94% accuracy (94% sensitivity and specificity) was obtained to distinguish

both types of tumours. This indicates that one can assess the presence of recurrence in comparison with regular grade 1 tumours in an objective and automatic fashion by using IR spectroscopy and chemometrics. This is immensely important stratification information, which cannot be routinely derived or inferred from the histological examination of meningiomas lying within a WHO grade. The spectral markers associated with recurrence (Table 3.4) were mainly protein (Amide I), lipids, collagen, and DNA/RNA changes ($\nu_{as}(PO_2^-)$). DNA alterations, in special DNA methylation, are highly associated with meningioma progression, especially as a discriminant feature between *NF2*-mutated and non-*NF2*-mutated tumours (Suppiah *et al.*, 2019). By evaluating the spectral profile of all patients in grade 1 cohort, 12 patients (patients 2, 11, 16, 22, 26, 30, 34, 38, 50, 56, 57, 69) were found to have these spectral markers following the same trend observed in grade 1 recurrence, in terms of relative intensity. This corresponds to 17% of grade 1 cohort, and these patients could be potential candidates to have grade 1 re-occurring in the future, once their spectral markers profile are similar to the ones in grade 1 recurrence cohort. In this case, these patients could be followed closely in the clinical scenario to evaluate if the tumour will reoccur in the future. Since meningioma reoccurs with an average time of 10 years, this pilot study does not have this confirmative information for these patients, although the estimated recurrence rate of 17% is close to the usual meningioma grade 1recurrence rate of 10%. It is worth mentioning that if 12 Grade 1 tumours (non-recurrent) had the spectral pattern of the 5 with Grade 1 recurrencies. Meaning only 5/17 (29%) with the spectral pattern will actually progress (low PPV) but can exclude the other Grade 1 (non-recurrent tumours). Can therefore reduce number of patients needing follow up.

This is just a hypothesis that needs further validation, but if this methodology is proved true, one could use this spectrochemical information to follow up patients with higher likelihood of recurrence and provide them with more specific treatments and closer attention, reducing existent costs associated with unknown recurrence odds. How to apply this principle

in a clinical setting will be our future target to move forward with this project. To achieve this target, setting up a spectroscopy lab within the neurosurgical unit with the appropriate hard and software and trained staff will give this technology its full potential with real time application. A number of neurosurgical units all over the world are using spectrometrical tools in practice for diagnostic and operative purposes. However, designing a Raman system for neurosurgical applications demands significant technical considerations both in terms of hardware implementation and data science methods (DePaoli *et al.,2020)*. More on that in Chapter 5 under future work.

Finally, grade 2 and grade 1 recurrence were discriminated based on their spectrochemical profile with an accuracy of 97% (97% sensitivity and 100% specificity) and the main spectral markers associated with recurrence (Table 3.6) were proteins (Amide I, Amide II, and Amide III), carbohydrates (ν(C-O)), and DNA/RNA alterations [NH_2 adenine, $\nu_{as}(PO_2^-)$], therefore indicating that these tumour types are very different. An important advantage of using ATR-FTIR spectroscopy is that due to its non-destructive nature, the same tissue section could theoretically be used for conventional histological analysis. Moreover, the sensitivity and specificity for meningioma tumours detection towards clinical diagnosis might improve in future applications using FTIR microspectroscopy due to its relatively larger spatial resolution in comparison with ATR-FTIR spectroscopy, which enables the acquisition of richer spatially-distributed spectrochemical information.

CHAPTER 4 | RAMAN SPECTROSCOPY ANALYSIS

4.1Results

4.1.1 Classical discriminant analysis

Ninety brain tissue samples (66 meningiomas Grade 1, 24 meningiomas Grade 2) were analysed by Raman microspectroscopy imaging. The median microscopic and Raman image for meningiomas Grade 1 and Grade 2 are depicted in Figures 4.1a–1d (the colour figures represent the mean response (average Raman intensity between 780–1858 cm^{-1}) of the median image for each group). Notably, each image presents different visual features due to the different distributions of chemicals on the sample surface, but their spectrochemical profile are very similar as shown in Figure 4.1e and 4.1f, indicating that chemical differences between meningiomas Grade 1and Grade 2 are not visually clear.

The pre-processed spectra from the images acquired in the spectral range between 780–1858 cm^{-1} (Figure 4.1f) were used for further analysis. This spectral region includes the Raman fingerprint region, hence, encompassing spectrochemical signals of the main biomolecules present in the tissue samples (Kelly *et al.,* 2011). The assignment of the main peaks of the pre-processed Raman spectrum is depicted in Figure 4.1f. These include C-C stretching [$\nu(C\text{-}C)_1$] in amino acids or polysaccharides at 850 cm^{-1}, C-C stretching [$\nu(C\text{-}C)_2$] in proteins at 890 cm^{-1}, C-C stretching [$\nu(C\text{-}C)_3$] in amino acids at 930 cm^{-1}, C-C stretching [$\nu(C\text{-}C)_4$] in phenylalanine at 1003 cm^{-1}, phospholipid structural changes at 1130 cm^{-1}, Amide III peak at 1265 cm^{-1}, CH_2 bending [$\delta(CH_2)_1$] in lipids at 1296 cm^{-1}, CH_3/CH_2 deformation modes in DNA/RNA at 1336 cm^{-1}, CH_2

bending [$\delta(CH_2)_2$] in malignant tissues at 1450 cm^{-1}, NH_2 bending [$\delta(NH_2)$] in cytosine at 1610 cm^{-1}, and Amide I absorption at 1665 cm^{-1} (Movasaghi *et al.*, 2007). Some of these peaks are discriminant features between the samples and some of them are common amongst the tumour types. The identification of relevant distinguishing spectral features between Grade 1 and Grade 2 samples are achieved by chemometric techniques.

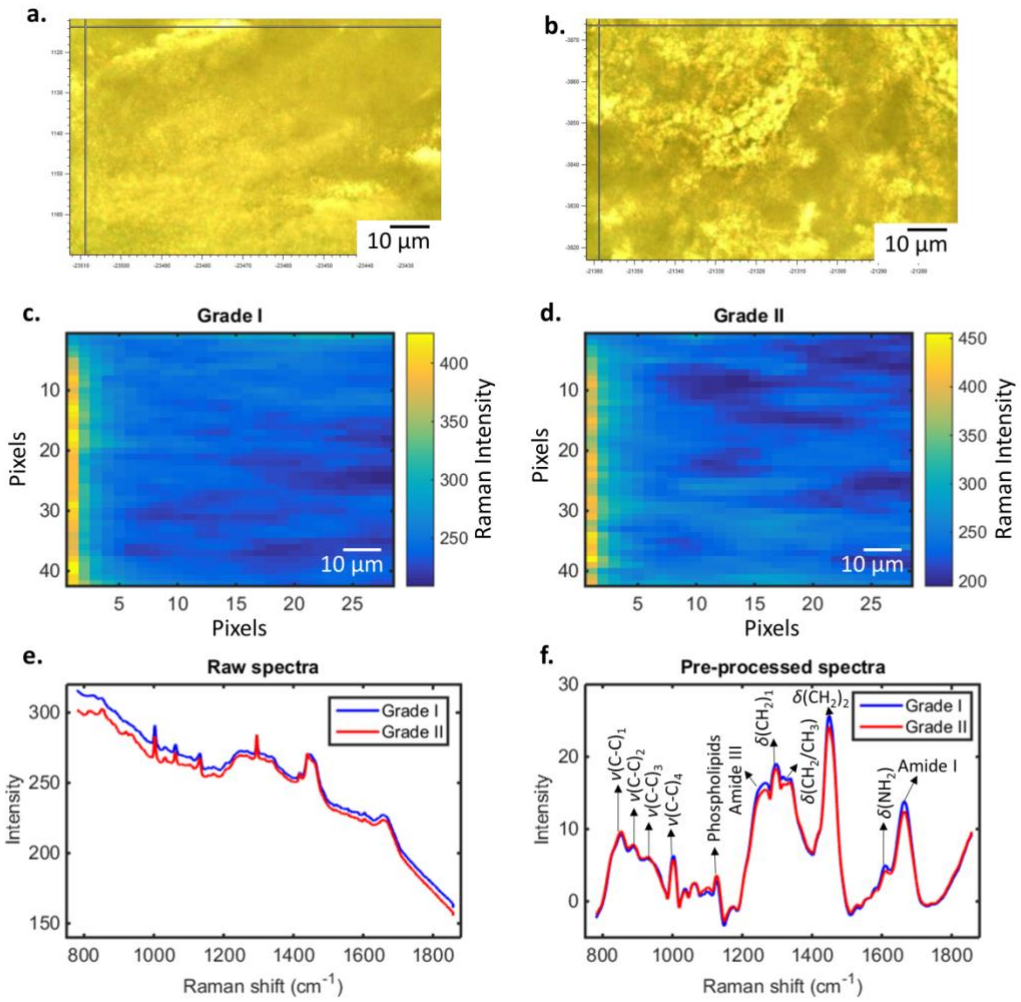

Figure 4.1 Median Raman miscrospectroscopy images. (a) Microscopic image of Grade 1 meningioma tissue; (b) microscopic image of Grade 2 meningioma tissue; (c) median raw image for meningioma Grade 1 samples; (d) median raw image for meningioma Grade 2 samples; (e) median raw spectra for meningiomas Grade 1 and Grade 2; (f) median pre-

processed spectra (Savitzky-Golay smoothing and asymmetric least squares baseline correction) for meningiomas with a tentative assignment of the main Raman peaks. Grade 1 and Grade 2. Colour bar: Raman intensity. *v*: stretching vibration, *δ*: bending.

Initially, outlier detection was performed by a Hotelling T^2 *versus* Q residuals test, where 4 samples (2 meningiomas Grade 1, 2 meningiomas Grade 2) were removed (Appendix C, Figure C1). First-order algorithms were used to analyse the pre-processed spectral data after outlier removal. Feature extraction and classification by means of principal component analysis linear discriminant analysis (PCA-LDA), principal component analysis quadratic discriminant analysis (PCA-QDA) and principal component analysis support vector machines (PCA-SVM); and feature selection and classification by means of successive projections algorithm linear discriminant analysis (SPA-LDA), successive projections algorithm quadratic discriminant analysis (SPA-QDA), successive projections algorithm support vector machines (SPA-SVM), genetic algorithm linear discriminant analysis (GA-LDA), genetic algorithm quadratic discriminant analysis (GA-QDA) and genetic algorithm support vector machines (GA-SVM), were applied to distinguish meningiomas Grades I and II on sample basis. Amongst the PCA-based algorithms (using 8 PCs, 98.94% explained variance; Appendix C, Figure C2), the best performance was obtained with PCA-QDA (96.2% accuracy, 85.7% sensitivity, 100% specificity, and F-score = 92.3%). Also, SPA-QDA was the best algorithm amongst SPA-based methods, with the same performance of PCA-QDA. GA-based methods showed overall poorer performance, where the best algorithm (GA-QDA) achieved 73.1% accuracy but 0% sensitivity, indicating that GA-based models are most likely overfitted. More details about the predictive performance of each of these algorithms are provided in Table 4.1. The ROC curve for PCA-QDA and SPA-QDA models are shown in Figure 4.2, where the AUC value was found at 0.929 indicating an outstanding classification performance for both algorithms.

QDA-based algorithms exhibit superior performance in comparison with LDA- and SVM-based methods. Usually, for complex biological data, QDA outperforms LDA since QDA-based algorithms model each class variance individually, while LDA assumes classes having similar variance structures (Morais & Lima, 2018). This occurs because the performance of QDA ultimately depends on the variance structure of the data. QDA is expected to work better than LDA for most biological applications, since quite commonly biological samples are composed of complex chemical matrices with different variances structures for each class. For example, diseases' samples can have a smaller variance distribution than healthy control samples, since the latter can be composed of individuals with different life habits, while patients with a same specific disease usually have a similar lifestyle. The same can occur with different tumour grades, where one class can assume a different variance distribution in comparison with the other. The only situation where QDA underperforms LDA is when the number of samples in the dataset is small (Wu *et al.*, 1996), since the variance of each group might not be totally covered by QDA hence increasing the degree of extrapolation needed and commonly leading the model to overfitting. Using multiple algorithms to train and test the data is a common procedure in data science and machine learning. Subsequently, we assess validity of the algorithm through accuracy, sensitivity, specificity, and F-Score. The rationale behind this practice is to pick the best algorithm for current and future application and to avoid the problem of under or overfitting. See Table 4.1.

Table 4.1 Quality parameter for distinguishing Grade 1 and Grade 2 meningiomas in the test set.

Algorithm	Accuracy	Sensitivity	Specificity	F-score
PCA-LDA	46.2%	85.7%	31.6%	46.2%
PCA-QDA	96.2%	85.7%	100%	92.3%

PCA-SVM	61.6%	28.6%	73.7%	41.2%
SPA-LDA	57.7%	100%	42.1%	49.3%
SPA-QDA	96.2%	85.7%	100%	92.3%
SPA-SVM	34.6%	71.4%	21.1%	32.5%
GA-LDA	61.5%	57.1%	63.2%	60.0%
GA-QDA	73.1%	0%	100%	0%
GA-SVM	42.3%	42.9%	42.1%	42.5%

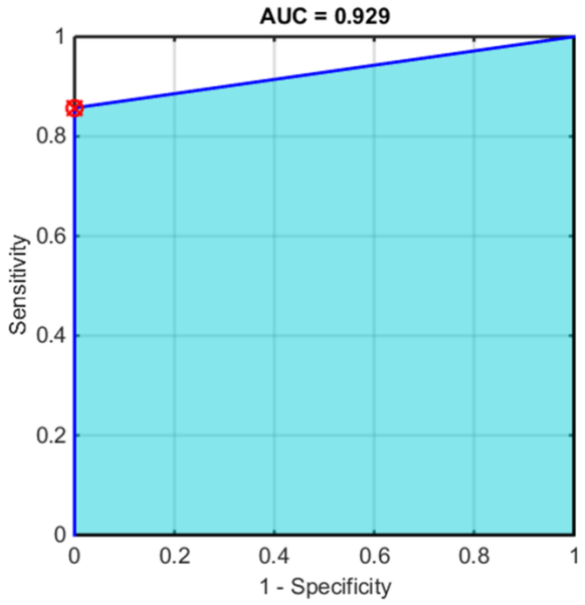

Figure 4.2 Receiver operating characteristic (ROC) curve for PCA-QDA and SPA-QDA. AUC: area under the curve.

SVM-based models seem to be highly overfitted, since the training performance for these algorithms are excellent (Table 4.2; Appendix C, Table C1), with near 100% correct classification rates; however, test performance is highly affected as demonstrated in Table 4.1. SVM classification performance would probably improve by adding more samples to the training set, thus creating a most representative training model. Nevertheless, PCA-QDA and SPA-QDA performance are both excellent in the test set, indicating that these algorithms are robust to provide a satisfactory prediction towards external samples.

Table 4.2 Correct classification rate for distinguishing Grade 1 and Grade 2 meningiomas.

Algorithm	Class	Training	Test
PCA-LDA	Grade 1	80.0	31.6
	Grade 2	66.7	85.7
PCA-QDA	Grade 1	97.8	100
	Grade 2	73.3	85.7
PCA-SVM	Grade 1	100	73.7
	Grade 2	100	28.6
SPA-LDA	Grade 1	75.6	42.1
	Grade 2	66.7	100
SPA-QDA	Grade 1	95.6	100
	Grade 2	46.7	85.7
SPA-SVM	Grade 1	77.8	21.1
	Grade 2	100	71.4
GA-LDA	Grade 1	100	63.2
	Grade 2	93.3	57.1
GA-QDA	Grade 1	100	100
	Grade 2	86.7	0
GA-SVM	Grade 1	91.1	42.1
	Grade 2	100	42.9

The difference-between-mean (DBM) spectrum, PCA loadings on PC1 (56.64% explained variance), and SPA-QDA selected variables are shown in Figure 4.3. The PCA loadings indicate higher coefficients at ~850 cm^{-1}, ~1003 cm^{-1}, ~1130 cm^{-1}, ~1337 cm-1, ~1450 cm^{-1}, ~1665 cm^{-1}, and ~1858 cm^{-1}; and the SPA-QDA selected variables are: ~850 cm^{-1}, ~1130 cm^{-1}, ~1245 cm^{-1}, ~1337 cm^{-1}, ~1450 cm^{-1}, and ~1858 cm^{-1}. Only the variable at 1245 cm^{-1} selected by SPA-QDA does not have a high PCA loadings, while the other variables selected by SPA-QDA are very close or are a perfect match with the ones observed in PCA-QDA. The list of PCA and SPA-QDA selected variables and tentative assignment according to Movasaghi *et al.* (2007) are shown in Table 4.3. The Raman shift at 1858 cm^{-1} is unknown based on this reference, but this wavenumber has been associated to C=O stretching in other literature (Mayo *et al.*, 2003). The peak

at around 850 cm^{-1} has been previously detected in meningioma samples as belonging to tyrosine (Mehta *et al.*, 2018), an α-amino acid that constitute important structures in proteins responsible for signal transduction processes (Kato *et al.*, 1993); and the peaks at 1003 cm^{-1} (phenylalanine) and 1450 cm^{-1} (CH_2 bending in DNA) have also been reported as biomarkers of meningioma tumours (Mehta *et al.*, 2018; Zhou *et al.*, 2012). Phospholipids (1130 cm^{-1}), Amide III (1245 cm^{-1}) and Amide I (1665 cm^{-1}) have been reported for brain tumours in general (Gajjar *et al.*, 2013; Zhou *et al.*, 2012).

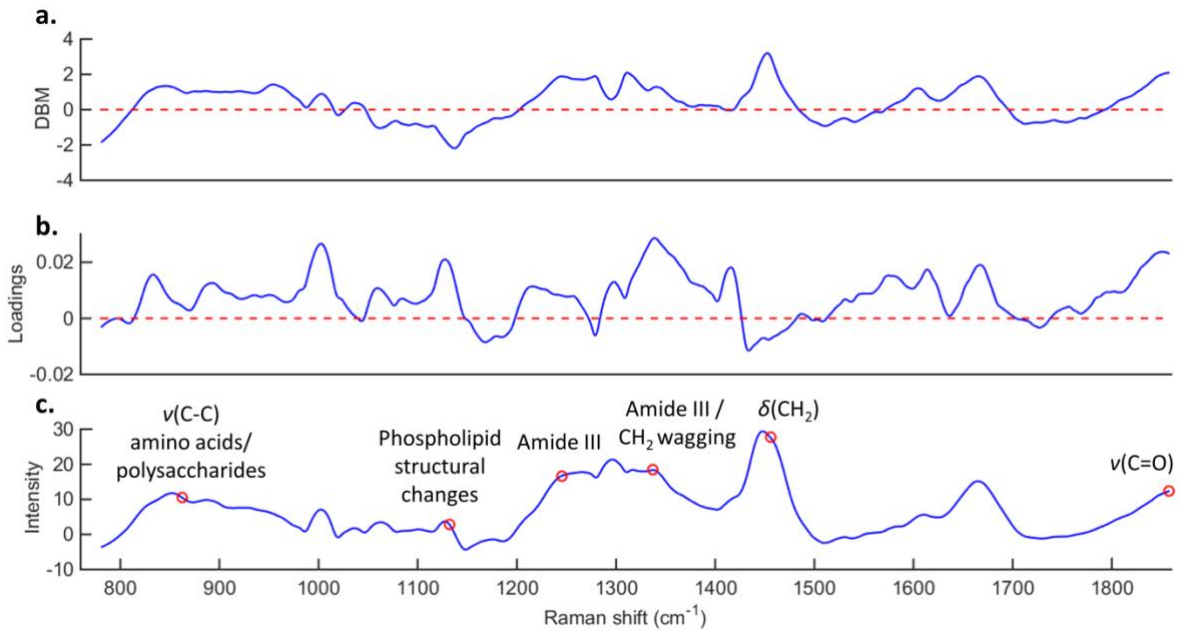

Figure 4.3 PCA loadings and SPA-QDA selected variables. (a) Difference-between-mean (DBM) spectrum (+ values: higher intensity in meningioma Grade 1 samples; - values: higher intensity in meningioma Grade 2 samples); (b) PCA loadings on PC1; (c) average training set spectrum and SPA-QDA selected variables (red circles) with their tentative assignment. *ν*: stretching vibration, *δ*: bending.

Table 4.3 Tentative assignment of PCA and SPA-QDA selected variables to distinguish meningiomas Grade 1and Grade 2. DBM: difference-between-mean spectrum, where ↑ represents higher intensity in meningioma Grade 1samples, and ↓ represents higher intensity in meningioma Grade 2 samples.

Peak	Algorithm	Assignment	DBM
850 cm^{-1}	PCA/SPA-QDA	Amino acids or polysaccharides	↑
1003 cm^{-1}	PCA	C-C in phenylalanine	↑
1130 cm^{-1}	PCA/SPA-QDA	Phospholipid structural changes	↓
1245 cm^{-1}	SPA-QDA	Amide III	↑
1337 cm^{-1}	PCA/SPA-QDA	Amide III and CH_2 wagging vibrations	↑
1450 cm^{-1}	PCA/SPA-QDA	CH_2 bending	↑
1665 cm^{-1}	PCA	Amide I	↑
1858 cm-1	PCA/SPA-QDA	C=O stretching	↑

MCR-ALS was employed to resolve the median Grade 1 and Grade 2 meningioma images in order to identify spectrochemical changes associated with tumour aggressiveness. MCR-ALS was performed with 4 components selected by singular value decomposition (99.99% explained variance, 0.21 lack of fit, non-negativity in concentration mode; Appendix C, Figure C3). The 1st component of MCR-ALS was found to be associated with Grade 2 appearance (Figure 4.4a), once it is clearly present in the Grade 2 tissue sample. The spectral profile of the 1st component (Sopt 1) indicates distinguishing features at the region between 1230 cm^{-1} and 1360 cm^{-1} in comparison with the spectral profiles for other components, where three peaks (1265 cm^{-1}, 1296 cm^{-1} and 1336 cm^{-1}) are presents. These peaks are associated with Amide III, CH_2 deformation in lipids, and CH_2/CH_3 twisting in polynucleotide chains, respectively (Movasaghi *et al.*, 2007). This region encompasses the wavenumber at 1337 cm^{-1} (amide III and CH_2 wagging vibrations) in Table 4.3. Similarly to Figure 4.1f, the peaks at 850 cm^{-1} [$\nu(C\text{-}C)_1$, amino acids or polysaccharides], 890 cm^{-1} [$\nu(C\text{-}C)_2$, proteins], 930 cm^{-1} [$\nu(C\text{-}C)_3$, amino acids], 1003 cm^{-1} [$\nu(C\text{-}C)_4$, phenylalanine], 1130 cm^{-1} (phospholipids), 1265 cm^{-1} (Amide III), 1296 cm^{-1} [$\delta(CH_2)_1$, lipids], 1336 cm^{-1} [$\delta(CH_3/CH_2)$, DNA/RNA], 1450 cm^{-1}

[$\delta(CH_2)_2$, malignant tissue], and 1665 cm^{-1} (Amide I) are also present. In addition, other peaks at 1060 cm^{-1} [$\nu(PO_2^-)$, DNA/RNA], 1100 cm^{-1} [$\nu(C\text{-}C)_5$, lipids], and a small arm at 1459 cm^{-1} [$\delta(CH_2)_3$, deoxyribose] (Movasaghi *et al.*, 2007) are observed as distinguishing features in the MCR-ALS Sopt 1 profile.

Bury *et al.* (2019a) have recently used Raman spectroscopy to discriminate meningioma Grade 1 brain tissue among different brain pathologies (low-grade glioma, high-grade glioma, metastasis, lymphoma, and no-tumour) with 94.8% accuracy, 63.9% sensitivity and 97.1% specificity using PCA-LDA with smear-based samples; and, meningioma Grade 1 brain tissue among low-grade glioma, high-grade glioma, metastasis and lymphoma with 90.8% accuracy, 91.7% sensitivity and 90.8% specificity using PCA-LDA with FFPE samples. Mehta *et al.* (2018) have recently used Raman spectroscopy to discriminate healthy controls and meningioma patients based on serum using PCA-LDA. Seventy patients (35 controls, 35 meningiomas) were analysed, resulting in 70% accuracy to distinguish meningiomas *versus* controls in an independent test set; 72% accuracy to distinguish meningiomas Grade 1 *versus* controls; and 80% accuracy to distinguish meningiomas Grade 2 *versus* controls. The results reported herein (96.2% accuracy, 85.7% sensitivity, 100% specificity) are very promising to distinguish meningioma tissue grades, which is critical to delineate patient treatment; and evidences the potential of Raman spectroscopy to investigate brain tumour tissues.

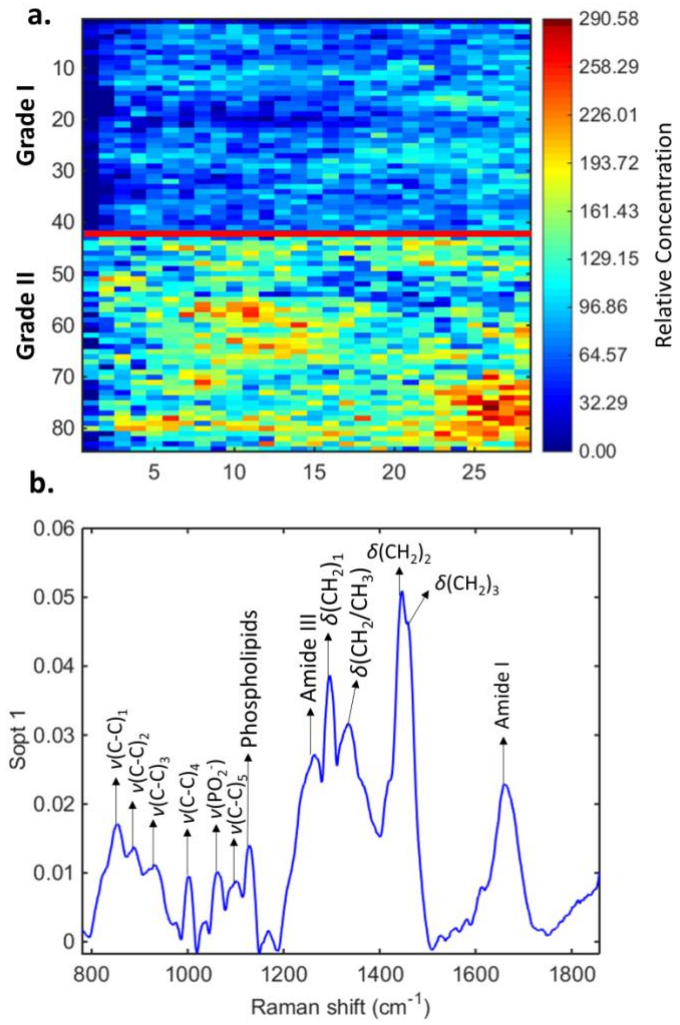

Figure 4.4 MCR-ALS results. (a) Recovered image using the MCR-ALS concentration profile for the 1st component; (b) MCR-ALS spectral profile for the 1st component with its tentative spectral markers assignment. Colour bar: relative concentration.

4.1.2 Three-dimensional discriminant analysis

A total of 95 images were analysed for three-dimensional discriminant analysis (66 grade 1 meningiomas, 24 grade 2 meningiomas, and 5 meningiomas from reoccurrence). Following pre-processing by spikes removal and baseline correction, the data underwent analysis by 3D-PCA-LDA and 3D-PCA-QDA in order to distinguish meningiomas grade 1 (n = 66) vs. grade 2 (n = 24), which are algorithms capable of working with the full 3D

hyperspectral images, with no need of unfolding them. Figure 4.5 shows examples of microscopy images for meningiomas grade 1 and 2 tissues (Figures 4.5a and 4.5b), as well as their average Raman imaging signatures (Figures 4.5c and 4.5d) and pre-processed spectra (Figures 4.5e and 4.5f).

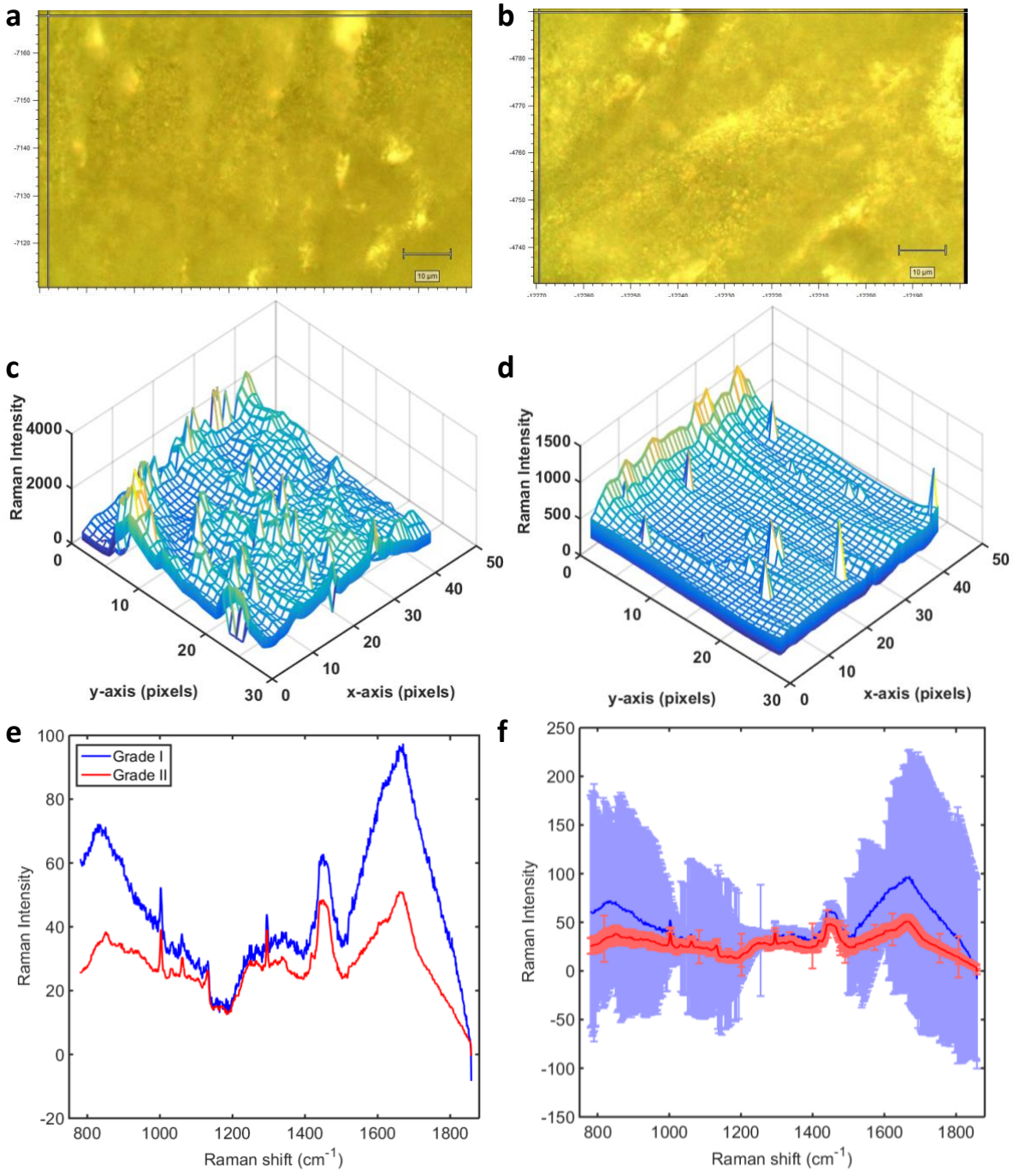

Figure 4.5 Examples of microscopic images of meningiomas (a) grade 1and (b) grade 2 tissues samples inside the Raman apparatus; average 3D Raman imaging signatures for meningiomas

(c) grade 1and (d) grade 2 samples; average Raman spectral signatures for (e) grade 1 and 2 meningiomas and (f) their standard-deviation.

The Raman spectra were acquired at the spectral range between 780-1858 cm^{-1}, which comprises the biofingerprint region where main absorptions for biomolecules such as carbohydrates, proteins, nucleic acids, and lipids can be observed (Kelly *et al.*, 2011). There are visual spectral differences for grade 1 and 2 meningiomas. Firstly, in Figure 4.5f, the standard-deviation for grade 1 and 2 meningiomas are very different, where grade 1 meningiomas show a large standard-deviation thus a wide spectral variation, while grade 2 meningiomas show a quite narrow standard-deviation, indicating a low spectral variability for this type of tumour. Figure 4.5e also shows differences in the spectral means for grade 1 and grade 2 meningiomas, where grade 2 meningiomas have an average lower intensity spectrum than grade 1 meningiomas, particularly in the regions around 800-100 cm^{-1} and 1500-1800 cm^{-1}. The 800-100 cm^{-1} region is mainly characterised by carbohydrates (*e.g.*, glucose at 842 cm^{-1}), nucleic acids (*e.g.*, RNA at 813 cm^{-1}, O-P-O stretching for DNA/RNA at 828 cm^{-1}, RNA ribose vibration at 867 cm^{-1}) and structural protein modes of tumours (~820 cm^{-1}) (Movasaghi *et al.*, 2007). The 1500-1800 cm^{-1} region is mainly characterised by the amide I peak of proteins (~1660 cm^{-1}) (Movasaghi *et al.*, 2007).

The images dataset was split into 70% of samples for training (46 grade 1, 17 grade 2 meningiomas) and 30% for testing (27 grade 1, 7 grade 2 meningiomas) before model construction. 3D-PCA-LDA and 3D-PCA-QDA models achieved very good performance in the training set where clear discrimination is observed using 2 PCs (Figure 4.6). The classification metrics for training, cross-validation (venetian blinds with 10 data splits) and test are shown in Table 4.4. The training and validation performance are perfect with accuracies of 100%. The test predictions show good results with accuracies of 81% for 3D-PCA-LDA (100%

sensitivity and 75% specificity) and 96% for 3D-PCA-QDA (100% sensitivity and 95% specificity). QDA shows better specificity thus being more accurate to identify grade 1 meningiomas. The F-score show better overall performance for 3D-PCA-QDA (F-score = 97%), thus indicating this algorithm can predict better test samples.

Table 4.4 Classification performance to distinguish meningiomas grade 1and II.

Algorithm	Set	Accuracy	Sensitivity	Specificity	F-score
3D-PCA-LDA	Training	1.00	1.00	1.00	1.00
	Cross-validation	1.00	1.00	1.00	1.00
	Test	0.81	1.00	0.75	0.86
3D-PCA-QDA	Training	1.00	1.00	1.00	1.00
	Cross-validation	1.00	1.00	1.00	1.00
	Test	0.96	1.00	0.95	0.97

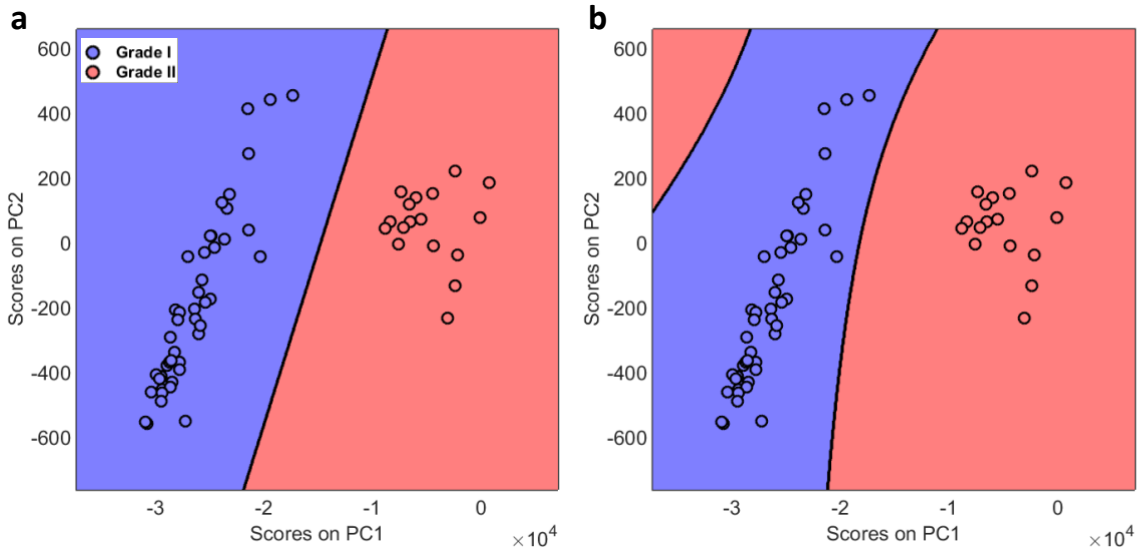

Figure 4.6 Discriminant boundaries for (a) 3D-PCA-LDA and (b) 3D-PCA-QDA showing the training samples.

The confusion matrices representing the prediction of the test samples are shown in Table 4.5. Their AUC values were calculated at 0.886 (3D-PCA-LDA) and 0.975 (3D-PCA-QDA), therefore being better for 3D-PCA-QDA (outstanding results). The remaining 5

recurrence samples were blindly predicted, and their outcome were majorly as grade 2 meningiomas using 3D-PCA-QDA (4 out of the 5 samples were predicted as grade 2, equivalent to 80%). The PCA loadings and the difference-between-mean (DBM) spectra for grade 1 and 2 meningiomas are show in Figure 4.7. Table 4.6 lists the main wavenumbers with the largest weights and their respective tentative assignments (Movasaghi *et al.*, 2007).

Table 4.5 Confusion matrix for the test set.

Algorithm		**Predicted**	
	Measured	Grade 1	Grade 2
3D-PCA-LDA	Grade 1	15	5
(AUC = 0.886)	Grade 2	0	7
	Recurrence	2	3
		Grade 1	Grade 2
3D-PCA-QDA	Grade 1	19	1
(AUC = 0.975)	Grade 2	0	7
	Recurrence	1	4

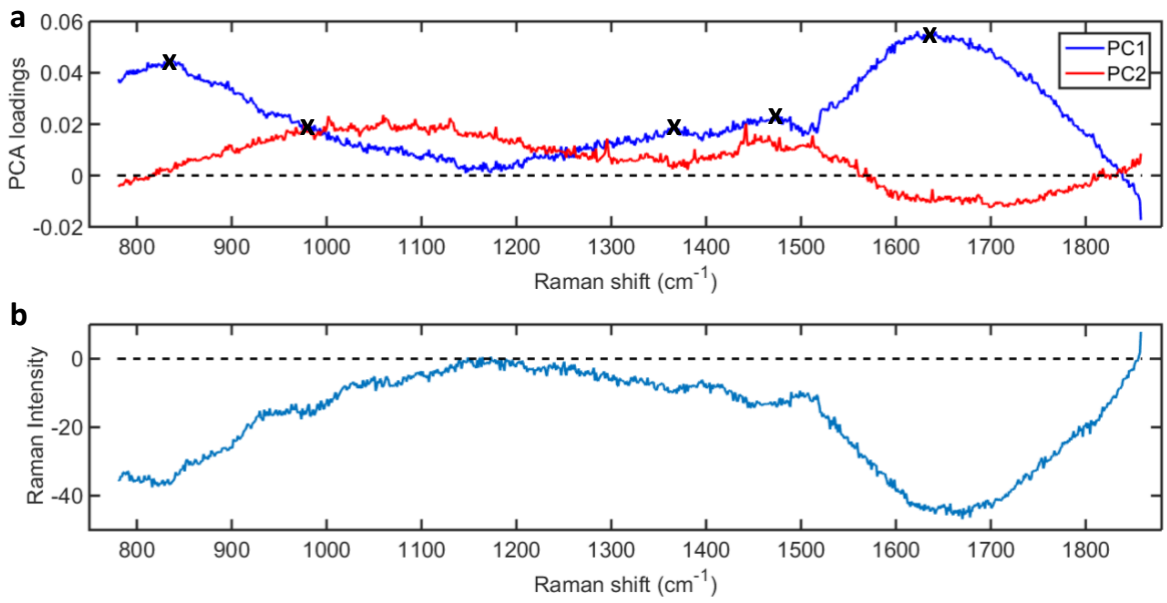

Figure 4.7 (a) 3D-PCA loadings on PC1 and PC2 and (b) difference-between-mean (DBM) spectrum between meningiomas grade 2 and grade 1. "x" markers show the main wavenumbers responsible for class differentiation.

Table 4.6. Main wavenumbers responsible for classification.

Wavenumber (cm^{-1})	Tentative assignment
832	υ_{as}(O-P-O) tyrosine
978	υ(C-C) β-sheet of proteins / δ(=CH) of lipids
1367	$\upsilon_s(CH_3)$ of phospholipids
1480	Amide II
1642	Amide I

4.2 Discussion

The diagnosis of meningioma tumours is a laborious procedure that requires clinical assessments such as radiological imaging and tissue histology, and often with later prognosis. Grade 1 meningiomas show histological patterns other than papillary, chordoid, clean cell or rhabdoid; grade 2 meningiomas show clear cell or chordoid cell types and have three of the following patterns: macronuclei, spontaneous necrosis, hypercellularity, small cell formation or sheeting architecture; grade 3meningiomas are much rarer and histologically they resemble other tumours such as melanomas, carcinomas, or sarcomas (Lilo *et al.*, 2020; Miller Jr *et al.*, 2014). The accurate and quick diagnosis can significantly aid clinicians planning the correct treatment and mitigate risks.

The use of Raman spectroscopy provides the ability to optically characterise biomolecular changes associated with the tumour grades, where the unique spectral fingerprint generated represents the samples biochemical profile. Infrared and Raman spectroscopy have been previously used to discriminate normal and tumour brain tissues, where neoplastic tissues such as meningiomas were found to be statically significant from normal tissues using PCA-LDA (Gajjar *et al.*, 2013). Herein, meningiomas tumour grades were distinguished using Raman hyperspectral imaging, where Raman spectra are acquired per individual tissue

positions forming a 3D image-like data. The 3D imaging data were analysed by newly-developed three-dimensional discriminant analysis algorithms (3D-PCA-LDA and 3D-PCA-QDA) which quickly discriminated the tissue grades in an accurate and systematic way. 3D-PCA-LDA achieved 81% accuracy (86% F-score, 100% sensitivity and 75% specificity) and 3D-PCA-QDA achieved 96% accuracy (97% F-score, 100% sensitivity and 95% specificity) in the test set. Four out the five recurrence samples were predicted using 3D-PCA-QDA as grade 2 meningiomas, showing these samples are mostly different from regular grade 1 meningiomas and are closer related to grade 2 meningiomas which have a higher likelihood of recurrence. The superior performance for 3D-PCA-QDA can be explained by the different variance structures for grades I and II meningiomas as shown in Figure 4.5f. QDA performs well when the data have difference variances for each class (Morais & Lima, 2018).

Cancerous and non-cancerous brain tissue samples have been distinguished with 89.4% sensitivity and 78.0% specificity using infrared spectroscopy, and glioma and meningiomas tissues have been distinguished at 82.1% sensitivity and 75.0% specificity using the same technique (Hands *et al.*, 2016). Meningiomas tumour grades have been distinguished using infrared spectroscopy with 79% accuracy (80% sensitivity and 73% specificity) using partial least squares discriminant analysis (PLS-DA) in Chapter 3. Serum-based Raman spectroscopy has been used to distinguish healthy controls *vs.* grade 1 meningiomas at 72% accuracy, and healthy controls *vs.* grade 2 meningiomas at 80% accuracy (Mehta *et al*, 2018). Grade 1 and 2 meningiomas have been classified using Raman microspectroscopy with classical discriminant analysis with 96.2% accuracy and F-score of 92.3% (85.7% sensitivity and 100% specificity) using unfolded PCA-QDA and SPA-QDA in section 4.2.1. This latter is a more complex algorithm that requires much larger time for processing (Morais *et al.*, 2020b).

The spectral markers associated with grade 1 and 2 discrimination are shown in Table 4.6. Most of them are associated with protein changes (832, 978, 1480 and 1642 cm^{-1}), and

lipids changes (978 and 1367 cm^{-1}). Protein changes such as Amide I (1642 cm^{-1}) and Amide II (1480 cm^{-1}) are known to be associated with brain cancer spectrochemical changes (Bury *et al.*, 2019b). For meningiomas grade 1 vs. grade 2 specifically, spectral changes for Amide I and Amide II has been observed as important markers for tumour differentiation using infrared spectroscopy in Chapter 3. In addition, lipids features have found to be highly related to brain tumours differences using infrared spectroscopy (Hands *et al.*, 2016). Although the molecular genetics and pathogenesis of meningiomas are not so well understood, growth factor alterations and signalling pathways have been reported, such as cell cycle deregulation and telomerase activation as signs for meningioma progression (Lilo *et al.*, 2020; Miller Jr *et al.*, 2014; Wrobel *et al.*, 2005). Cell cycle control, telomerase dynamics and deoxyribonucleic acid damage control are highly entwined in meningioma progression (Miller Jr *et al.*, 2014; Wrobel *et al.*, 2005). Meningiomas grade 1 are known to be characterised by overexpression of epidermal growth factor receptors and upregulation/overexpression of the platelet-derived growth factor receptor beta gene (Miller Jr *et al.*, 2014), downregulation of proteins of 4.1 family members (Miller Jr *et al.*, 2014; Saraf *et al.*, 2011), and mutation of the *NF2* gene on chromosome 22 in some meningiomas grade 1(Miller Jr *et al.*, 2014). Higher-grade meningiomas are associated with alterations in chromosome 10 and other genetic non-*NF2* changes (Miller Jr *et al.*, 2014; Wernicke *et al.*, 2010). Meningiomas grade 2 particularly are known to be associated with chromosome mutations in the 1p and 14p regions, which are responsible for housing tumour suppression genes, and other changes in chromosome 1 (Miller Jr *et al.*, 2014). These biochemical alterations on meningiomas can be detected in the Raman spectrochemical signatures enabling an accurate and quick diagnosis of their tumour grades through computational techniques. An advantage of this technique is that it is reagent-free and not affected by water interference, which is ideal for biological medium. These findings show the

potential of Raman hyperspectral imaging for differentiation of meningioma tumours, being a feasible new diagnostic tool for tumour grade detection in the clinical setting.

CHAPTER 5 | OVERALL DISCUSSION AND CONCLUSION

The proposed hypothesis was that the variability in the molecular phenotype of meningiomas (for example Grade 1, Grade 2, recurrence) were sufficiently different from one another that biospectrometry techniques were sensitive enough to stratify the patient into different categories based on the meningioma aggressiveness and potential for recurrence. The results presented in the thesis here confirmed that WHO grade 1 verses grade 2 meningioma verses grade 1 recurrence could be blindly discriminated using both ATR-FTIR and Raman spectroscopy. Several wavenumbers were identified as possible biomarkers towards tumour differentiation, associated with lipids, protein, DNA/RNA, and carbohydrate alterations, proving the hypothesis that there was a specific biomarker(s) responsible for the variability in the molecular phenotype.

Brain cancers are one of the main causes of cancer-related deaths worldwide, accounting for 3% of all tumours diagnosed annually and with an increasing incidence rate over the last few years (Bury *et al.*, 2020). Tumours are difficult to be fully removed thus causing post-surgery consequences and likely reoccurrence which increases mortality, even though they comprise a small portion of all tumours often diagnosed (Bury *et al.*, 2020; Hollon *et al.*, 2016). Most brain cancers are either meningioma or glioma tumours (Gajjar *et al.*, 2013). Meningiomas are a less aggressive type of tumours, often benign, that occurs in a supratentorial location, such as towards the spinal cord or the meninges surrounding the brain (Huntoon *et al.*, 2020; Lilo *et al.*, 2020; Mehta *et al.*, 2018). Glioma are a more aggressive type, comprising of neuroepithelial tumours originating from the glial or supporting cells of the central nervous system (CNS) (Davis, 2018).

Both FTIR and Raman spectroscopy can be employed for the chemical analysis of tissue, where vibrational signals are obtained from biomolecules bonds that compose the tissue. These unique spectral features for FTIR and Raman make these spectroscopy techniques very attractive to determine chemical compositions of unknown substances. FTIR spectroscopy, as well as other molecular spectroscopy techniques such as liquid chromatography-mass spectrometry (LC/MS), nuclear magnetic resonance (NMR) spectroscopy, near-infrared (NIR), and Raman spectroscopy provide robust and supportive data about the sample chemical composition.

Herein, we investigated both FTIR and Raman spectroscopy for analysis of meningioma tissues towards differentiation between WHO grade 1 and 2 tumours. Chapter 3 described the analysis using FTIR to investigative meningioma WHO tumour grades (grade 1 and 2) and the recurrence.

In Chapter 3, ATR-FTIR in combination with chemometric techniques were employed to distinguish meningiomas grade 1, grade 2 and grade 1 that re-occurred. Ninety-nine patients (70 WHO grade 1 meningiomas, 24 WHO grade 2 meningiomas, and 5 WHO grade 1 meningiomas from recurrence) were investigated in this study where their FFPE brain tissue samples were analysed by ATR-FTIR spectroscopy. Subsequent classification was performed *via* PCA-LDA and PLS-DA. PLS-DA gave the best results where grade 1 and grade 2 meningiomas were discriminated with 79% accuracy, 80% sensitivity and 73% specificity; while grade 1 *vs.* grade 1 recurrence and grade 2 *vs.* grade 1 recurrence were discriminated with 94% accuracy (94% sensitivity and specificity) and 97% accuracy (97% sensitivity and 100% specificity), respectively. Several wavenumbers were identified as possible biomarkers towards tumour differentiation. The majority of these were associated with lipids, protein, DNA/RNA, and carbohydrate alterations. These findings demonstrated the potential of ATR-

FTIR spectroscopy towards meningioma grade discrimination as a fast, low-cost, non-destructive, and sensitive tool for clinical settings.

In Chapter 4, we reported the analysis of meningiomas grade 1 and 2 tumours using Raman spectroscopy by means of classical analysis and by three-dimensional analysis for Raman imaging. Raman microspectroscopy imaging was used to investigate 95 brain tissue samples (66 WHO grade 1 meningiomas, 24 WHO grade 2 meningiomas and 5 WHO grade 1 meningiomas from recurrence) in order to differentiate meningiomas Grade 1 and Grade 2 samples, which are the commonest types of brain tumour. For the classical analysis using the unfolded spectra within the Raman microspectroscopy images, several classification algorithms using feature extraction and selection methods were tested, in which the best classification performances were achieved by unfolded PCA-QDA and SPA-QDA algorithms, resulting in accuracies of 96.2%, sensitivities of 85.7% and specificities of 100% using both methods. A biochemical profiling in terms of spectral markers was investigated using the difference-between-mean (DBM) spectrum, PCA loadings, SPA-QDA selected wavenumbers, and the recovered imaging profiles after MCR-ALS, where the following wavenumbers were found to be associated with class differentiation: 850 cm^{-1} (amino acids or polysaccharides), 1130 cm^{-1} (phospholipid structural changes), the region between 1230 – 1360 cm^{-1} (Amide III and CH_2 deformation), 1450 cm^{-1} (CH_2 bending), and 1858 cm^{-1} (C=O stretching). For the data analysis using the whole Raman hyperspectral images in Chapter 4, newly-developed three-dimensional discriminant analysis algorithms were used to process the hyperspectral imaging data in a 3D fashion. 3D-PCA-QDA was able to distinguish grade 1 and grade 2 meningioma samples with 96% test accuracy (100% sensitivity and 95% specificity), and 80% of the recurrence samples were classified as grade 2, indicating they are different from regular grade 1 meningiomas but closer

related to grade 2 tumours, which have much higher likelihood of recurrence. As advantage, Raman is reagent-free and not affected by water interference, which is ideal for biological medium. These findings show the potential of Raman hyperspectral imaging for differentiation of meningioma tumours, being a feasible new diagnostic tool for tumour grade detection in the clinical setting.

Table 5.1 summarises the results obtained with FTIR (Chapter 3) and Raman (Chapter 4) spectroscopy to distinguish meningiomas tumour grades. Raman spectroscopy has shown greater discrimination potential between grade 1 vs. II meningioma, while FTIR was able to detect differences between grade 2 and recurrence samples, whereas Raman predicted most of recurrence samples as grade 2 tumours.

Table 5.1 Best results using FTIR and Raman spectroscopy to distinguish WHO grade 1 vs. grade 2 meningiomas based on tissue analysis.

Technique	Samples	Algorithm	Main results
FTIR (ATR-FTIR)	70 grade 1 24 grade 2 5 recurrences grade 1	PLS-DA	Grade 1 *vs.* 2: 79% accuracy (80% sensitivity, 73% specificity) Grade 1 *vs.* I recurrence: 94% accuracy (94% sensitivity, 94% specificity) Grade 2 *vs.* 1 recurrence: 97% accuracy (97% sensitivity, 100% specificity)
Raman (imaging)	66 grade 1 24 grade 2 5 recurrences grade 1	3D-PCA-QDA	Grade 1 vs. 2: 96% accuracy (100% sensitivity, 95% specificity) Recurrence prediction: 80% predicted as grade 2

Both FTIR and Raman have proved to be high-throughput techniques which are reagent-free and non-destructive, giving accurate predictive information regarding the meningioma tumour grades, hence, having enormous clinical potential with regards to being developed for intra-operative real-time assessment of disease. Improvements of FTIR and Raman instrumentation overtime have finally put them in the lead through their improved

spectral quality, reproducibility of data, and user-friendliness coupled with relatively reduced maintenance cost. Advancements of Raman and FTIR spectroscopy have positively influenced the health sector to industrial and point-of-care applications. Real time application and the flexibility in the rapidly growing lasers and detectors have further offered the unique strengths in the existing diagnostic devices. Moving forward, the industrial production of lower-cost, sensitive and more modern devices are crucial for bringing these technologies into the clinical theatres as complementary tools to aid diagnostic. This in effect will reduce the death rates seen in the world today and it will also give timely and permanent solutions to chronic disease.

Limitations of this study are mainly the small number of grade 2 meningiomas. This is due to the natural distribution of ratio between grade 1 and grade 2 meningioma in a single centre in real world setting. In addition to that was our strict selection criteria and long term follow up which has excluded a number of pre-selected cases. The reason for this exclusion was to avoid selection bias. We tried to overcome this by obtaining multiple spectra points from each sample (10 for FTIR and 25 for Raman). This has helped to improve the results which is reflected by the performance of our selected algorithms.

As future work, I would like to build a lab within the department of neurosurgery equipped with the latest hardware and software technology in Raman spectroscopy that can be utilised for instant tissue diagnosis, prognostication, and surgical excision in real time. The precision of this technology will likely improve over the course of the foreseen future; the coming quantum computation will allow for better and quicker machine learning algorithms. Collaboration with other groups working on the field will be very useful to help to expand our shared knowledge and experience allowing us to deliver tailored medical and surgical care for our patients.

REFERENCES

Abbritti RV, Polito F, Cucinotta M, Lo Giudice C, Caffo M, Tomasello C, Germanò A, Aguennouz M. Meningiomas and Proteomics: Focus on New Potential Biomarkers and Molecular Pathways. Cancer Genomics Proteomics **2016**; 13(5):369–379.

Abramczyk H, Brozek-Pluska B, Jarota A, Surmacki J, Imiela A, Kopec M. A look into the use of Raman spectroscopy for brain and breast cancer diagnostics: linear and non-linear optics in cancer research as a gateway to tumor cell identity. Expert Rev. Mol. Diagn. **2020**; 20: 99–115.

Alexiou GA, Markoula S, Gogou P, Kyritsis AP. Genetic and molecular alterations in meningiomas. Clin. Neurol. Neurosurg. **2011**; 113(4): 261–267.

Ali K, Lu Y, Christensen C, May T, Hyett C, Griebel R, Fourney D, Meguro K, Resch L, Sharma RK. Fourier transform infrared spectromicroscopy and hierarchical cluster analysis of human meningiomas. Int. J. Mol. Med. **2008**; 21(3):297–301.

Al-Mefty, DeMonte F, McDermott M. Al-Mefty's Meningiomas. 2nd ed. Thieme Publishers: New York, **2011**.

al-Rodhan NR, Laws Jr ER. Meningioma: a historical study of the tumor and its surgical management. Neurosurgery **1990**; 26(5): 832–846.

Amatya VJ, Takeshima Y, Inai K. Methylation of p14(ARF) gene in meningiomas and its correlation to the p53 expression and mutation. Mod. Pathol. **2004**; 17(6): 705–710.

Amharref N, Beljebbar A, Dukic S, Venteo L, Schneider L, Plout M, Vistelle R, Manfait M. Brain tissue characterisation by infrared imaging in a rat glioma model. Biochim. Biophys. Acta **2006**; 1758(7):892–899.

Asaoka K, Barrs DM, Sampson JH, McElveen Jr JT, Tucci DL, Fukushima T. Intracanalicular meningioma mimicking vestibular schwannoma. AJNR Am. J. Neuroradiol. **2002**; 23(9): 1493–1496.

Auner GW, Koya SK, Huang C, Broadbent B, Trexler M, Auner Z, Elias A, Mehne KC, Brusatori MA. Applications of Raman spectroscopy in cancer diagnosis. Cancer Metastasis Rev. **2018**; 37: 691–717.

Bakay L. Cruveilhier on meningiomas (1829-1842). Surg. Neurol. **1989**; 32(2): 159–164.

Baker MJ, Trevisan J, Bassan P, Bhargava R, Butler HJ, Dorling KM, Fielden PR, Fogarty SW, Fullwood NJ, Heys KA, Hughes C, Lasch P, Martin-Hirsch PL, Obinaju B, Sockalingum GD, Sulé-Suso J, Strong RJ, Walsh MJ, Wood BR, Gardner P, Martin FL. Using Fourier transform IR spectroscopy to analyze biological materials. Nat. Protoc. **2014**; 9(8): 1771–1791.

Ballabio D, Consonni V. Classification tools in chemistry. Part 1: linear models. PLS-DA. Anal. Methods **2013**; 5:3790–3798.

Barthélemy EJ, Sarkiss CA, Lee J, Shrivastava RK. The historical origin of the term "meningioma" and the rise of nationalistic neurosurgery. J. Neurosurg. **2016**; 125(5): 1283–1290.

Bekaert L, Emery E, Levallet G, Lechapt-Zalcman E. Histopathologic diagnosis of brain metastases: current trends in management and future considerations. Brain Tumour Pathol. **2017**; 34: 8–19.

Beleites C, Steiner G, Sowa MG, Baumgartner R, Sobottka S, Schackert G, Salzer R. Classification of human gliomas by infrared imaging spectroscopy and chemometric image processing. Vib. Spectrosc. **2005**; 38(1-2):143–149.

Bender, L., Somme, F., Lhermitte, B., Ahle, G., Boone, M., Blonski, M., Pouget, C., Truc, G., Cebula, H., & Noël, G. High risk of recurrence for grade 2 meningioma: a 10-year multicenter analysis of prognosis factors. Chinese Clinical Oncology. **2021**; [Online] 10:3

Bie L, Zhao G, Ju Y, Zhang B. Integrative genomic analysis identifies CCNB1 and CDC2 as candidate genes associated with meningioma recurrence. Cancer Genet. **2011**; 204(10): 536–540.

Brereton RG, Lloyd GR. Partial least squares discriminant analysis: taking the magic away. J. Chemometr. **2014**; 28(4): 213–225.

Brereton RG, Lloyd GR. Support Vector Machines for classification and regression. Analyst **2010**; 135: 230–267.

Bro R, Smilde AK. Principal component analysis. Anal. Methods **2014**; 6: 2812–2831.

Bury D, Morais CLM, Ashton KM, Dawson TP, Martin FL. Ex Vivo Raman Spectrochemical Analysis Using a Handheld Probe Demonstrates High Predictive Capability of Brain Tumour Status. Biosensors **2019a**; 9: 49.

Bury D, Morais CLM, Martin FL, Lima KMG, Ashton KM, Baker MJ, Dawson TP. Discrimination of fresh frozen non-tumour and tumour brain tissue using spectrochemical analyses and a classification model. Br. J. Neurosurg. **2020**; 34: 40–45.

Bury D, Morais CLM, Paraskevaidi M, Ashton KM, Dawson TP, Martin FL. Spectral classification for diagnosis involving numerous pathologies in a complex clinical setting: A neuro-oncology example. Spectrochim. Acta. A Mol. Biomol. Spectrosc. **2019b**; 206: 89–96.

Butler HJ, Ashton L, Bird B, Cinque G, Curtis K, Dorney J, Esmonde-White K, Fullwood NJ, Gardner B, Martin-Hirsch PL, Walsh MJ, McAinsh MR, Stone N, Martin FL. Using Raman spectroscopy to characterize biological materials. Nat. Protoc. **2016**; 11(4): 664–687.

Butler HJ, Brennan PM, Cameron JM, Finlayson D, Hegarty MG, Jenkinson MD, Palmer DS, Smith BR, Baker MJ. Development of high-throughput ATR-FTIR technology for rapid triage of brain cancer. Nat. Commun. **2019**; 10: 4501.

Byrne HJ, Baranska M, Puppels GJ, Stone N, Wood B, Gough KM, Lasch P, Heraud P, Sulé-Suso J, Sockalingum GD. Spectropathology for the next generation: Quo vadis?. Analyst **2015**; 140: 2066–2073.

Cameron JM, Butler HJ, Smith BR, Hegarty MG, Jenkinson MD, Syed K, Brennan PM, Ashton K, Dawson T, Palmer DS, Baker MJ. Developing infrared spectroscopic detection for

stratifying brain tumour patients: glioblastoma multiforme vs. Lymphoma. Analyst **2019**; 144: 6736–6750.

Cameron JM, Conn JJA, Rinaldi C, Sala A, Brennan PM, Jenkinson MD, Caldwell H, Cinque G, Syed K, Butler HJ, Hegarty MG, Palmer DS, Baker MJ. Interrogation of IDH1 Status in Gliomas by Fourier Transform Infrared Spectroscopy. Cancers **2020a**; 12(12): 3682.

Cameron JM, Rinaldi C, Butler HJ, Hegarty MG, Brennan PM, Jenkinson MD, Syed K, Ashton KM, Dawson TP, Palmer DS, Baker MJ. Stratifying Brain Tumour Histological Sub-Types: The Application of ATR-FTIR Serum Spectroscopy in Secondary Care. Cancers **2020b**; 12(7): 1710.

Cao X, Hao S, Wu Z, Wang L, Jia G, Zhang L, Zhang J. Treatment Response and Prognosis After Recurrence of Atypical Meningiomas. World Neurosurg. **2015**; 84(4): 1014–1019.

Cea-Soriano L, Wallander MA, García Rodríguez LA. Epidemiology of meningioma in the United Kingdom. Neuroepidemiology **2012**; 39(1): 27–34.

Claus EB, Calvocoressi L, Bondy ML, Schildkraut JM, Wiemels JL, Wrensch M. Dental x-rays and risk of meningioma. Cancer **2012**; 118(18): 4530–4537.

Claus EB, Calvocoressi L, Bondy ML, Wrensch M, Wiemels JL, Schildkraut JM. Exogenous hormone use, reproductive factors, and risk of intracranial meningioma in females. J. Neurosurg. **2013**; 118(3): 649–656.

Cortes C, Vapnik V. Support-vector networks. Mach. Learn. **1995**; 20: 273–297.

Cushing H, Eisenhardt L. Meningiomas. Their Classification, Regional Behaviour, Life History, and Surgical End Results. C.C. Thomas: Baltimore, **1938**.

Cushing H. The Meningiomas (Dural Endotheliomas): Their Source, and Favoured Seats of Origin. Brain **1922**; 45(2): 282–316.

Davis ME. Epidemiology and Overview of Gliomas. Semin. Oncol. Nurs. **2018**; 34(5):420–429.

Desroches J, Jermyn M, Pinto M, Picot F, Tremblay MA, Obaid S, Marple E, Urmey K, Trudel D, Soulez G, Guiot MC, Wilson BC, Petrecca K, Leblond F. A new method using Raman spectroscopy for in vivo targeted brain cancer tissue biopsy. Sci. Rep. **2018**; 8: 1792.

DePaoli D, Lemoine É, Ember K, Parent M, Prud'homme M, Cantin L, Petrecca K, Leblond F, Côté DC. Rise of Raman spectroscopy in neurosurgery: a review. Journal of Biomedical Optics. **2020** ;25(5):050901

Dixon SJ, Brereton RG. Comparison of performance of five common classifiers represented as boundary methods: Euclidean Distance to Centroids, Linear Discriminant Analysis, Quadratic Discriminant Analysis, Learning Vector Quantization and Support Vector Machines, as dependent on data structure. Chemometr. Intell. Lab. Syst. **2009**; 95(1): 1–17.

Doyle NM, Doyle JF, Walter EJ. The life and work of Harvey Cushing 1869–1939: A pioneer of neurosurgery. J. Intensive Care Soc. **2017**; 18(2): 157–158.

Duraipandian S, Zheng W, Ng J, Low JJH, Ilancheran A, Huang Z. Near-infrared-excited confocal Raman spectroscopy advances in vivo diagnosis of cervical precancer. J. Biomed. Opt. **2013**; 18(6): 067007.

Ellenbogen RG, Sekhar LN, Kitchen ND. Principles of Neurological Surgery. 4th edn. Elsevier: Amsterdam, **2018**.

Gajjar K, Heppenstall LD, Pang W, Ashton KM, Trevisan J, Patel II, Llabjani V, Stringfellow HF, Martin-Hirsch PL, Dawson T, Martin FL. Diagnostic segregation of human brain tumours using Fourier-transform infrared and/or Raman spectroscopy coupled with discriminant analysis. Anal. Methods **2013**; 5:89–102.

Goldbrunner R, Minniti G, Preusser M, Jenkinson MD, Sallabanda K, Houdart E, von Deimling A, Stavrinou P, Lefranc F, Lund-Johansen M, Moyal ECJ, Brandsma D, Henriksson R, Soffietti R, Weller M. EANO guidelines for the diagnosis and treatment of meningiomas. Lancet Oncol. **2016**; 17(9): e383–e391.

Hands JR, Clemens G, Stables R, Ashton K, Brodbelt A, Davis C, Dawson TP, Jenkinson MD, Lea RW, Walker C, Baker MJ. Brain tumour differentiation: rapid stratified serum diagnostics via attenuated total reflection Fourier-transform infrared spectroscopy. J. Neurooncol. **2016**; 127(3):463–472.

Hands JR, Dorling KM, Abel P, Ashton KM, Brodbelt A, Davis C, Dawson T, Jenkinson MD, Lea RW, Walker C, Baker MJ. Attenuated Total Reflection Fourier Transform Infrared (ATR-FTIR) spectral discrimination of brain tumour severity from serum samples. J. Biophotonics **2014**; 7(3-4): 189–199.

Hartmann C, Brostöm J, Simon M. Diagnostic, and molecular pathology of meningiomas. Expert. Rev. Neurother. **2006**; 6(11): 1671–1683.

Hollon T, Lewis S, Freudiger CW, Xie XS, Orringer DA. Improving the accuracy of brain tumor surgery via Raman-based technology. Neurosurg. Focus **2016**; 40: E9.

Huntoon K, Toland AMS, Dahiya S. Meningioma: A Review of Clinicopathological and Molecular Aspects. Front. Oncol. **2020**; 10: 579599.

Ildan F, Erman T, Göçer AI, Tuna M, Bağdatoğlu H, Çetinalp E, Burgut R. Predicting the Probability of Meningioma Recurrence in the Preoperative and Early Postoperative Period: A Multivariate Analysis in the Midterm Follow-Up. Skull Base **2007**; 17(3): 157–171.

Jaumot J, de Juan A, Tauler R. MCR-ALS GUI 2.0: New features and applications. Chemom. Intell. Lab. Syst. **2015**; 140: 1–12.

Jhawar BS, Fuchs CS, Colditz G, Stampfer MJ. Sex steroid hormone exposures and risk for meningioma. J. Neurosurg. **2003**; 99(5): 848–853.

Kärjä V, Sandell P, Kauppinen T, Alafuzoff I. Does protein expression predict recurrence of benign World Health Organization grade 1meningioma?. Hum. Pathol. **2010**; 41(2): 199–207.

Kato H, Faria TN, Stannard B, Roberts Jr CT, LeRoith D. Role of tyrosine kinase activity in signal transduction by the insulin-like growth factor-I (IGF-I) receptor. Characterization of kinase-deficient IGF-I receptors and the action of an IGF-I-mimetic antibody (alpha IR-3). J. Biol. Chem. **1993**; 268(4): 2655–2661.

Kelly JG, Trevisan J, Scott AD, Carmichael PL, Pollock HM, Martin-Hirsch PL, Martin FL. Biospectroscopy to metabolically profile biomolecular structure: a multistage approach linking computational analysis with biomarkers. J. Proteome Res. **2011**; 10(4): 1437–1448.

Kenig S, Bedolla DE, Birarda G, Faoro V, Mitri E, Vindigni A, Storici P, Vaccari L. Fourier transform infrared microspectroscopy reveals biochemical changes associated with glioma stem cell differentiation. Biophys. Chem. **2015**; 207:90–96.

Kennard RW, Stone LA. Computer Aided Design of Experiments. Technometrics **1969**; 11(1):137–148.

Kleihues P, Burger PC, Scheithauer BW. Histological Typing of Tumours of the Central Nervous System. World Health Organization: Geneva, **1993**.

Klinger DR, Flores BC, Lewis JJ, Hatanpaa K, Choe K, Mickey B, Barnett S. Atypical Meningiomas: Recurrence, Reoperation, and Radiotherapy. World Neurosurg. **2015**; 84(3): 839–845.

Koljenović S, Schut TB, Vincent A, Kros JM, Puppels GJ. Detection of meningioma in dura mater by Raman spectroscopy. Anal. Chem. **2005**; 77: 7958–7965.

Krenning EP, Kwekkeboom DJ, Bakker WH, Breeman WA, Kooij PP, Uei HY, van Hagen M, Postema PT, de Jong M, Reubi JC, Visser TJ, Reijs AEM, Hofland LJ, Koper JW, Lamberts SWJ. Somatostatin receptor scintigraphy with [111In-DTPA-D-Phe1]- and [123I-Tyr3]-octreotide: the Rotterdam experience with more than 1000 patients. Eur. J. Nucl. Med. **1993**; 20(8): 716–731.

Larjavaara S, Haapasalo H, Sankila R, Helén P, Auvinen A. Is the incidence of meningiomas underestimated? A regional survey. Br. J. Cancer **2008**; 99(1): 182–184.

Lebert H. Traité pratique des maladies cancéreuses et des affections curables confondues avec le cancer. JB Baillière: Paris, **1851**.

Levy Jr WJ, Bay J, Dohn D. Spinal cord meningioma. J. Neurosurg. **1982**; 57(6): 804–812.

Lilo T, Morais CLM, Ashton KM, Pardilho A, Davis C, Dawson TP, Gurusinghe N, Martin FL. Spectrochemical differentiation of meningioma tumours based on attenuated total reflection Fourier-transform infrared (ATR-FTIR) spectroscopy. Anal. Bioanal. Chem. **2020**; 412: 1077–1086.

Livermore LJ, Isabelle M, Bell IM, Scott C, Walsby-Tickle J, Gannon J, Plaha P, Vallance C, Ansorge O. Rapid intraoperative molecular genetic classification of gliomas using Raman spectroscopy. Neurooncol. Adv. **2019**; 1(1): vdz008.

Livingston DM. The master of light: a biography of Albert A. Michelson. University of Chicago Press: Chicago, **1973**.

Longstreth Jr WT, Dennis LK, McGuire VM, Drangsholt MT, Koepsell TD. Epidemiology of intracranial meningioma. Cancer **1993**; 72(3): 639–648.

Louis DN, Perry A, Reifenberger G, von Deimling A, Figarella-Branger D, Cavenee WK, Ohgaki H, Wiestler OD, Kleihues P, Ellison DW. The 2016 World Health Organization Classification of Tumors of the Central Nervous System: a summary. Acta Neurophathol. **2016**; 131(6): 803–820.

Louis DN, Ohgaki H, Wiestler OD, Cavenee WK, Burger PC, Jouvet A, Scheithauer BW, Kleihues P. The 2007 WHO classification of tumours of the central nervous system. Acta Neuropathol. **2007**; 114(2): 97–109.

Louis DN, Perry A, Wesseling P, Brat DJ, Cree IA, Figarella-Branger D, Hawkins C, Ng HK, Pfister SM, Reifenberger G, Soffietti R, von Deimling A, Ellison DW. The 2021 WHO Classification of Tumors of the Central Nervous System: a summary. Neuro Oncol. **2021**; 23(8): 1231–1251.

Macmillan M. Localization and William Macewen's early brain surgery Part II: The cases. J. Hist. Neurosci. **2005**; 14(1): 24–56.

Maile EJ, Barnes I, Finlayson AF, Sayeed S, Ali R. Nervous System and Intracranial Tumour Incidence by Ethnicity in England, 2001–2007: A Descriptive Epidemiological Study. PLoS One **2016**; 11(5): e0154347.

Mandrekar JN. Receiver Operating Characteristic Curve in Diagnostic Test Assessment. J. Thorac. Oncol. **2010**; 5(9): 1315–1316.

Marosi C, Hassler M, Roessler K, Reni M, Sant M, Mazza R, Vecht C. Meningioma. Crit. Rev. Oncol. Hematol. **2008**; 67(2): 153–171.

McCall J. Genetic algorithms for modelling and optimisation. J. Comput. Appl. Math. **2005**; 184(1): 205–222.

McLendon RE, Rosenblum MK, Bigner DD. Russell & Rubinstein's Pathology of Tumors of the Nervous System. 7th edn. Hodder Education Publishers: London, **2006**.

Mehta K, Atak A, Sahu A, Srivastava S, Murali Krishna C. An early investigative serum Raman spectroscopy study of meningioma. Analyst **2018**; 143:1916–1923.

Martin FL, Kelly JG, Llabjani V, Martin-Hirsch PL, Patel II, Trevisan J, Fullwood NJ, Walsh MJ. Distinguishing cell types or populations based on the computational analysis of their infrared spectra. Nat. Protoc. **2010**; 5:1748–1760.

Mayo DW, Miller FA, Hannah RW. Course Notes on the Interpretation of Infrared and Raman Spectra. John Wiley & Sons: Hoboken, **2003**.

Miller Jr R, DeCandio ML, Dixon-Mah Y, Giglio P, Vandergrift III WA, Banik NL, Patel SJ, Varma AK, Das A. Molecular Targets and Treatment of Meningioma. J. Neurol. Neurosurg. **2014**; 1(1):1000101.

Mitchell AL, Gajjar KB, Theophilou G, Martin FL, Martin-Hirsch PL. Vibrational spectroscopy of biofluids for disease screening or diagnosis: translation from the laboratory to a clinical setting. J. Biophotonics **2014**; 7: 153–165.

Morais CLM, Giamougiannis P, Grabowska R, Wood NJ, Martin-Hirsch PL, Martin FL. A three-dimensional discriminant analysis approach for hyperspectral images. Analyst **2020a**; 145: 5915–5924.

Morais CLM, Lilo T, Ashton KM, Davis C, Dawson TP, Gurusinghe N, Martin FL. Determination of meningioma brain tumour grades using Raman microspectroscopy imaging. Analyst **2019a**; 144: 7024–7031.

Morais CLM, Lima KMG. Comparing unfolded and two-dimensional discriminant analysis and support vector machines for classification of EEM data, Chemometr. Intell. Lab. Syst. **2017**: 170: 1–12.

Morais CLM, Lima KMG, Martin FL. Uncertainty estimation and misclassification probability for classification models based on discriminant analysis and support vector machines. Anal. Chim. Acta **2019b**; 1063: 40–46.

Morais CLM, Lima KMG. Principal Component Analysis with Linear and Quadratic Discriminant Analysis for Identification of Cancer Samples Based on Mass Spectrometry. J. Braz. Chem. Soc. **2018**; 29(3): 472–481.

Morais CLM, Lima KMG, Singh M, Martin FL. Tutorial: multivariate classification for vibrational spectroscopy in biological samples. Nat. Protoc. **2020b**; 15: 2143–2162.

Morais CLM, Martin-Hirsch PL, Martin FL. A three-dimensional principal component analysis approach for exploratory analysis of hyperspectral data: identification of ovarian cancer samples based on Raman microspectroscopy imaging of blood plasma. Analyst **2019c**; 144: 2312–2319.

Morais CLM, Paraskevaidi M, Cui L, Fullwood NJ, Isabelle M, Lima KMG, Martin-Hirsch PL, Sreedhar H, Trevisan J, Walsh MJ, Zhang D, Zhu YG, Martin FL. Standardization of complex biologically derived spectrochemical datasets. Nat. Protoc. **2019d**; 14: 1546–1577.

Morais CLM, Santos MCD, Lima KMG, Martin FL. Improving data splitting for classification applications in spectrochemical analyses employing a random-mutation Kennard-Stone algorithm approach. Bioinformatics **2019e**; 35(24): 5257–5263.

Movasaghi Z, Rehman S, ur Rehman I. Fourier Transform Infrared (FTIR) Spectroscopy of Biological Tissues. Appl. Spectrosc. Rev. **2008**; 43(2): 134–179.

Movasaghi Z, Rehman S, ur Rehman I. Raman Spectroscopy of Biological Tissues. Appl. Spectrosc. Rev. **2007**; 42(5): 493–541.

Nagar VA, Ye JR, Ng WH, Chan YH, Hui F, Lee CK, Lim CCT. Diffusion-weighted MR imaging: diagnosing atypical or malignant meningiomas and detecting tumor dedifferentiation. AJNR Am. J. Neuroradiol. **2008**; 29(6): 1147–1152.

Navas N, Romero-Pastor J, Manzano E, Cardell C. Benefits of applying combined diffuse reflectance FTIR spectroscopy and principal component analysis for the study of blue tempera historical painting. Anal. Chim. Acta **2008**; 630(2): 141–149.

Netsky MG, Lapresle J. The First Account of a Meningioma. Bull. Hist. Med. **1956**; 30(5): 465–468.

Nikulin AE, Dolenko B, Bezabeh T, Somorjai RL. Near-optimal region selection for feature space reduction: novel preprocessing methods for classifying MR spectra. NMR Biomed. **1998**; 11(4-5): 209–216.

Noreen R, Pineau R, Chin CC, Cestelli-Guidi M, Hwu Y, Marcelli A, Moenner M, Petibois C. Functional histology of glioma vasculature by FTIR imaging. Anal. Bioanal. Chem. **2011**; 401(3):795–801.

Nowak A, Dziedzic T, Krych P, Czernicki T, Kunert P, Marchel A. Benign versus atypical meningiomas: risk factors predicting recurrence. Neurol. Neurochir. Pol. **2015**; 49(1): 1–10.

Ostrom QT, Gittleman H, Xu J, Kromer C, Wolinsky Y, Kruchko C, Barnholtz-Sloan JS. CBTRUS Statistical Report: Primary Brain and Other Central Nervous System Tumors Diagnosed in the United States in 2009-2013. Neuro Oncol. **2016**; 18(suppl_5): v1–v75.

Oya S, Kawai K, Nakatomi H, Saito N. Significance of Simpson grading system in modern meningioma surgery: integration of the grade with MIB-1 labeling index as a key to predict the recurrence of WHO Grade 1meningiomas. J. Neurosurg. **2012**; 117(1): 121–128.

Paraskevaidi M, Morais CLM, Raglan O, Lima KMG, Paraskevaidis E, Martin-Hirsch PL, Kyrgiou M, Martin FL. Aluminium foil as na alternative substrate for the spectroscopic interrogation of endometrial cancer. J. Biophotonics **2018**; 11(7): e201700372.

Patel AJ, Wan YW, Al-Ouran R, Revelli JP, Cardenas MF, Oneissi M, Xi L, Jalali A, Magnotti JF, Muzny DM, Doddapeneni HV, Sebastian S, Heck KA, Goodman JC, Gopinath SP, Liu Z, Rao G, Plon SE, Yoshor D, Wheleer DA, Zoghbi HY, Klisch TJ. Molecular profiling predicts meningioma recurrence and reveals loss of DREAM complex repression in aggressive tumors. Proc. Natl. Acad. Sci. U.S.A. **2019**; 116(43): 21715–21726,

Pećina-Šlaus N, Kafka A, Lechpammer M. Molecular Genetics of Intracranial Meningiomas with Emphasis on Canonical Wnt Signalling. Cancers **2016**; 8(7): 67.

Pećina-Šlaus N. Merlin, the NF2 gene product. Pathol. Oncol. Res. **2013**; 19(3): 365–373.

Perry A, Stafford SL, Scheithauer BW, Suman VJ, Lohse CM. Meningioma grading: an analysis of histologic parameters. Am. J. Surg. Pahtol. **1997**; 21(12): 1455–1465.

Poletto M, Zattera AJ, Santana RMC. Santana, Structural differences between wood species: Evidence from chemical composition, FTIR spectroscopy, and thermogravimetric analysis. J. Appl. Polym. Sci. **2012**; 126(S1): E337–E344.

Prats-Montalbán JM, de Juan A, Ferrer A. Multivariate image analysis: A review with applications. Chemometr. Intell. Lab. Syst. **2011**; 107(1): 1–23.

Preston DL, Ron E, Yonehara S, Kobuke T, Fujii H, Kishikawa M, Tokunaga M, Tokuoka S, Mabuchi K. Tumors of the nervous system and pituitary gland associated with atomic bomb radiation exposure. J. Natl. Cancer Inst. **2002**; 94(20): 1555–1563.

Rockhill J, Mrugala M, Chamberlain MC. Intracranial meningiomas: an overview of diagnosis and treatment. Neurosurg. Focus **2007**; 23(4): E1.

Roser F, Samii M, Ostertag H, Bellinzona M. The Ki-67 proliferation antigen in meningiomas. Experience in 600 cases. Acta Neurochir. **2004**; 146(1): 37–44.

Sadetzki S, Modan B, Chetrit A, Freedman L. An iatrogenic epidemic of benign meningioma. Am. J. Epidemiol. **2000**; 151(3): 266–272.

Santos MCD, Morais CLM, Nascimento YM, Araujo JMG, Lima KMG. Spectroscopy with computational analysis in virological studies: A decade (2006–2016). Trends Anal. Chem. **2017**; 97: 244–256.

Saraf S, McCarthy BJ, Villano JL. Update on meningiomas. Oncologist. **2011**; 16(11):1604–1613.

Skoog DA, Holler FJ, Crouch SR. Principles of Instrumental Analysis. 6th edn. Thomson Brooks/Cole: Belmont, **2007**.

Smith BR, Ashton KM, Brodbelt A, Dawson T, Jenkinson MD, Hunt NT, Palmer DS, Baker MJ. Baker, Combining random forest and 2D correlation analysis to identify serum spectral signatures for neuro-oncology. Analyst **2016**; 141: 3668–3678.

Soares SFC, Gomes AA, Araujo MCU, Galvão Filho AR, Galvão RKH. The successive projections algorithm. Trends Anal. Chem. **2013**; 42: 84–98.

Solero CL, Fornari M, Giombini S, Lasio G, Oliveri G, Cimino C, Pluchino F. Spinal meningiomas: review of 174 operated cases. Neurosurgery **1989**; 25(2): 153–160.

Steiner G, Shaw A, Choo-Smith LP, Abuid MH, Schackert G, Sobottka S, Steller W, Salzer R, Mantsch HH. Distinguishing and grading human gliomas by IR spectroscopy. Biopolymers. **2003**; 72(6):464–471.

Sughrue ME, Kane AJ, Shangari G, Rutkowski MJ, McDermott MW, Berger MS, Parsa AT. The relevance of Simpson Grade 1and II resection in modern neurosurgical treatment of World Health Organization Grade 1meningiomas. J. Neurosurg. **2010**; 113(5): 1029–1035.

Suppiah S, Nassiri F, Bi WL, Dunn IF, Hanemann CO, Horbinski CM, Hashizume R, James CD, Mawrin C, Noushmehr H, Perry A, Sahm F, Sloan A, Von Deimling A, Wen PY, Aldape K, Zadeh G, International Consortium on Meningiomas. Molecular and translational advances in meningiomas. Neuro Oncol. **2019**; 21(Supplement_1):i4–i17.

Takahashi Y, Wanibuchi M, Kimura Y, Akiyama Y, Mikami T, Mikuni N. Meningioma Originating from the Hypoglossal Canal: Case Report and Review of Literature. World Neurosurg. **2019**; 127:525–529.

Vandenabeele P, Edwards H. Raman Spectroscopy in Archaeology and Art History: Volume 2. Royal Society of Chemistry: London, **2018**.

Venur VA, Santagata S, Galanis E, Brastianos PK. New molecular targets in meningiomas: the present and the future. Curr. Opin. Neurol. **2018**; 31(6): 740–746.

Wang Q, Fan SY, Qian J, Wang JY, Lu YC, Hu GH, Luo C. AKT2 expression in histopathologic grading and recurrence of meningiomas. Eur. J. Surg. Oncol. **2014**; 40(9): 1056–1061.

Wehbe K, Forfar I, Eimer S, Cinque G. Discrimination between two different grades of human glioma based on blood vessel infrared spectral imaging. Anal. Bioanal. Chem. **2015**; 407:7295–7305.

Wernicke AG, Dicker AP, Whiton M, Ivanidze J, Hyslop T, Hammond EH, Perry A, Andrews DW, Kenyon L. Assessment of Epidermal Growth Factor Receptor (EGFR) expression in human meningioma. Radiat. Oncol. **2010**; 5:46.

Wiemels J, Wrensch M, Claus EB. Epidemiology and etiology of meningioma. J. Neurooncol. **2010**; 99(3): 307–314.

Wrobel G, Roerig P, Kokocinski F, Neban K, Hahn M, Reifenberger G, Lichter P. Microarray-based gene expression profiling of benign, atypical and anaplastic meningiomas identifies novel genes associated with meningioma progression. Int. J. Cancer **2005**; 114(2):249–256.

Wu W, Mallet Y, Walczak B, Penninckx W, Massart DL, Heuerding S, Erni F. Comparison of regularized discriminant analysis linear discriminant analysis and quadratic discriminant analysis applied to NIR data. Anal. Chim. Acta **1996**; 329(3): 257–265.

Yamanaka R, Hayano A, Kanayama T. Radiation-Induced Meningiomas: An Exhaustive Review of the Literature. World Neurosurg. **2017**; 97: 635–644.

Yano S, Kuratsu J, Kumamoto Brain Tumour Research Group. Indications for surgery in patients with asymptomatic meningiomas based on an extensive experience. J. Neurosurg. **2006**; 105(4): 538–543.

Yeo Y, Park C, Lee JW, Kang Y, Ahn JM, Kang HS, Lee E. Magnetic resonance imaging spectrum of spinal meningioma. Clin. Imaging. **2019**; 55:100–106.

Yew A, Trang A, Nagasawa DT, Spasic M, Choy W, Garcia HM, Yang I. Chromosomal alterations, prognostic factors, and targeted molecular therapies for malignant meningiomas. J. Clin. Neurosci. **2013**; 20(1): 17–22.

Youngblood, M. W., Duran, D., Montejo, J. D., Li, C., Omay, S. B., Özduman, K., Sheth, A. H., Zhao, A. Y., Tyrtova, E., Miyagishima, D. F., Fomchenko, E. I., Hong, C. S., Clark, V. E., Riche, M., Peyre, M., Boetto, J., Sohrabi, S., Koljaka, S., Baranoski, J. F., Knight, J., Zhu, H., Pamir, M. N., Avşar, T., Kilic, T., Schramm, J., Timmer, M., Goldbrunner, R., Gong, Y., Bayri, Y., Amankulor, N., Hamilton, R. L., Bilguvar, K., Tikhonova, I., Tomak, P. R., Huttner, A., Simon, M., Krischek, B., Kalamarides, M., Erson-Omay, E. Z., Moliterno, J., & Günel, M. **2020;** Correlations between genomic subgroup and clinical features in a cohort of more than 3000 meningiomas, *Journal of Neurosurgery JNS*, *133*(5), 1345-1354.

Yuzawa S, Nishihara H, Tanaka S. Genetic landscape of meningioma. Brain Tumor Pathol. **2016**; 33(4): 237–247.

Zhou Y, Liu C, Sun Y, Pu Y, Boydston-White S, Liu Y, Alfano RR. Human brain cancer studied by resonance Raman spectroscopy. J. Biomed. Opt. **2012**; 17(11): 116021.

APPENDIX A | BASIS OF FTIR AND RAMAN SPECTROSCOPY

A1. Brief history of Fourier-transform infrared (FTIR) spectroscopy

Infrared (IR) spectroscopy is a vibrational spectroscopy technique used to assess the chemical composition of a sample (Skoog *et al.*, 2007). It is based on the absorption of infrared light by the molecules that compose the material, where all molecules with a resultant dipole moment different from zero will absorb infrared radiation. The scientific idea behind the Fourier-transform infrared spectroscopy (FTIR) was first initiated in the late 1880s by Albert A. Michelson. The founder invented an interferometer, a device that Albert and Morley used to perform famous experiments determined to measure the exact speed of light. Besides the Michelson interferometer, he also introduced the scientific optical instruments. His efforts were widely accepted and appreciated by the scientists of the day. Later in 1907, Michelson's efforts and inventions were still applicable and won the Nobel Prize in Physics.

Michelson knew the spectroscopic potential of his interferometer, although it lacked the sensitive detectors and the Fourier-transform algorithms that consequently barred the instrument from its practical application. However, he still manipulated and used it to solve many doublet spectra back then in the field (Navas *et al.*, 2008). There were quite many challenges that scientists faced while using Fourier-transform spectroscopy (FTS) to compute the Fourier-transform of interferograms. It is because the FTS was not able to directly invert the values, so they guessed some spectra, calculated the inverse of their Fourier-transform, and then compared it to the interferogram they had earlier measured. The best results were obtained after modifying the guessed spectra to match the data at hand.

It is in the late 1940s that the practical application of the FTS was considered useful. The scientists first used the interferograms when measuring light from the celestial bodies after producing the first Fourier-transform spectrum in 1949. At this point, it became more accessible for the scientists to calculate the continuous necessary Fourier transforms though it became a task that was so difficult and consumed much time. Here, the scientists introduced the lamellar granting and the Fabry-Perot interferometers, besides the Michelson's. The schematic Figure A1a below represents the basic Michelson interferometer.

Movasaghi *et al.* (2008) speculated that the lamellar granting spectrometer share many standard features with the Michelson's. These two beam and multicomplex devices have high optical ability to produce the interferograms, which, when Fourier-transformed, provide the desired spectrum. However, in the lamellar granting instrument, the optical modulation part constitutes a pair of mirrors that are arranged in a tongue and groove manner to bring the appearance of one large mirror divided into two or more horizontal strips as indicated in Figure A1b.

Through the Fresnel mirrors, the scientists could observe interferences with the blue-ray path difference near line F at wavelength 1737. After the reflection on both mirror surfaces on the thin plate, they noticed increased interference at wavelength 3406. Later, they perfected the technique and used it to detect IR radiations and to measure IR wavelengths. The lamellar granting interferometer is preferred to Michelson's because it uses the entire wavefront, unlike the Michelson's that loses one half of the total flux even when the beam splitter is perfect and efficient. Additionally, the lamellar granting interferometer has high efficiency due to its far-infrared region.

The increased interest in spectroscopy facilitated advancements in interferometers and its applications in physical systems. The improvements in the theories included the fast Fourier-

transform algorithm that made the electronic computing of the Fourier transforms easy and efficient (Livingston, 1973). The idea substantially reduced the time of calculations and magnitude orders, as well as turning the interferogram to a readable spectrum feasible. The Fourier spectroscopy generated a new weapon to greater effectiveness to experimentalists in 1969.

The IR technique applied a reliable, simple, powerful, and most effective method to analyze organic materials with a dispersive technology in the early 1940s. However, there were shortcomings attached to its scanning speed and the general manual operations; it was too slow. The wavelength of the light that passed through also measured one by one with just a slit controlling the spectral bandwidth. The dispersive spectrometer required a source of visible wavelength calibrations because there was no reference to any. The dispersive spectrometer is shown in Figure A1c.

These shortcomings enhanced further improvements on the dispersive. Consequently, the improved phase came handy with three significant advantages over the dispersive FTIR system. The modern FTIR spectrometer does not separate light into individual frequencies for measurements; instead, every interferogram has information from each wavelength of the light being measured (Duraipandian *et al.*, 2013). Through the interferometer, the FTIR spectrometer modulates the wavelength from the broadband infrared source. The detector then measures the intensity of the transmitted and reflected light as a function of its wavelength.

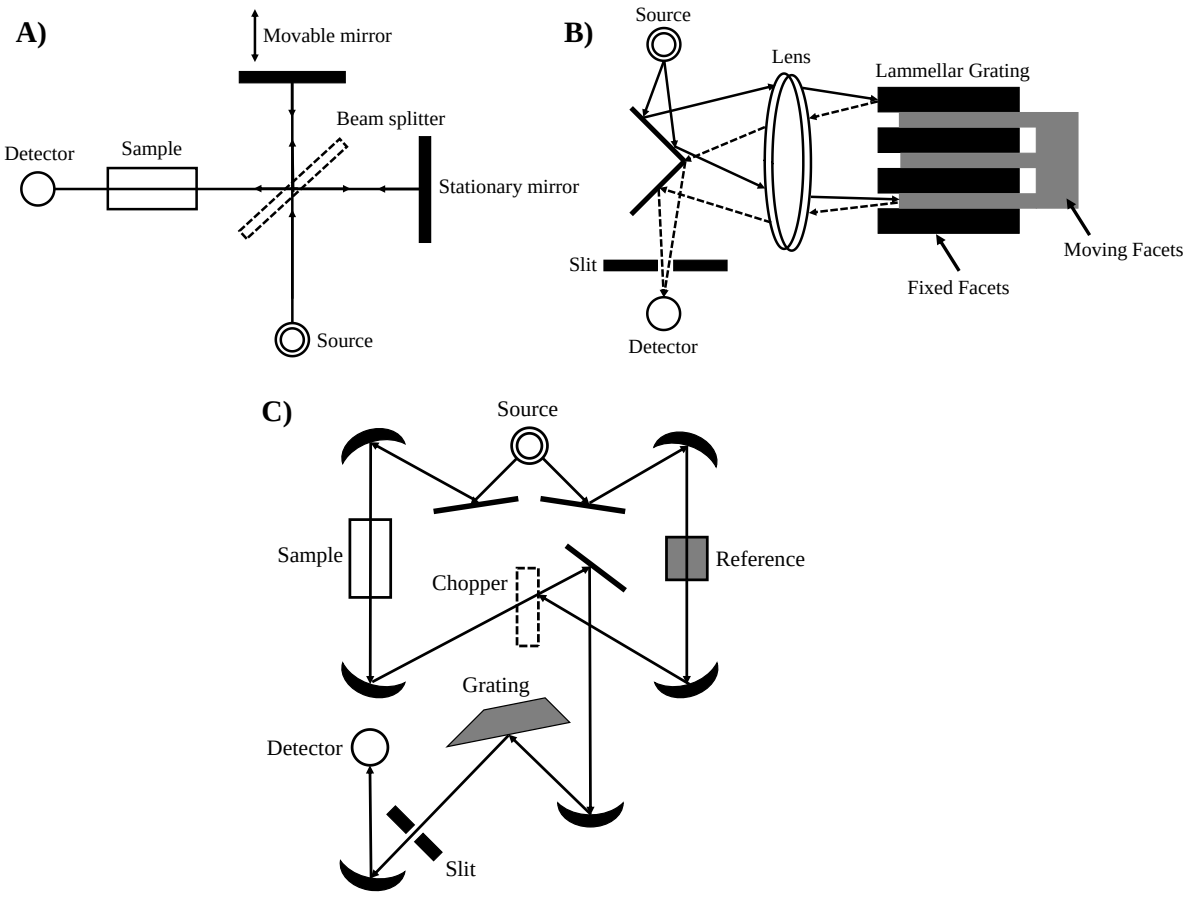

Figure A1. (a) Schematic diagram of Michelson interferometer; (b) the lamellar granting interferometer; (c) dispersive spectrometer.

With increased technology, modern spectrometers availability and enhanced capabilities increased with a gradual reduction in costs. Currently, the FTS hastened by the fastest computers processes the Fourier transformations with visible, infrared, and microwave regions in microseconds and are conventional devices in laboratories worldwide. The increase of performance and reduction in cost make FTS an attractive spectroscopy tool in many disciplines. Therefore, Fourier spectroscopy is a collective term that has been used while describing the breakdown of varying signals into the respective frequency components. It entails compelling mathematical methods that have been used by a series of spectroscopies,

including the Fourier-transform infrared (FTIR), Fourier-transform near infrared (FT-NIR), and Fourier-transform Raman spectroscopy.

A2. Brief history of Raman spectroscopy

On the other hand, Raman spectroscopy, a technique introduced in 1928 by Sir Chandrasekhara Venkata Raman, explained the effects of light changing its wavelength when it is passing through a transparent object. In his experiment, the Indian Physicist used sunlight as a source, liquid in a bucket as the collector, and his eyes, detectors. This remarkable phenomenon was called the Raman scattering. He gradually improved his instrumentation to achieve a better result; from helium, argon, rubidium and cesium lamps to lasers Ar^+ (351.l-514.5 nm), Kr^+ (337.4-676.4 nm) and today laser diodes NdYAG (1,064 nm) while the photomultipliers and CCD cameras used as detectors. Moreover, the extended the progress to the detection systems from the cooled cascade RCA IP21 in 1942 to cooled RCA C-7073B photomultiplier in 1950 then cooled RCA IP21 photomultiplier tube that was used by 1953 (Vandenabeele & Edwards, 2018). In the meantime, it was introduced a device called Hilger E612 that was used as a photoelectric instrument. Subsequently, Cary Model 81 Raman spectrometer came to existence. It used a three kilowatts helicon Hg arc of Toronto type with double gating, double slit twin monochromator.

The persistence in developing the optical system continued in 1960. The scientists learned that a twin monochromator could eliminate the stray lights more efficiently compared to the single monochromator. Instead, they introduced a triple monochromator, which was perfect in removing the stray gleams. Eventually, in 1968, the Holographic gratings appeared, which wholesomely improved the efficiency of the Raman scattering and collection systems.

The developments have ensured the current commercial state of the art of the Raman measurements and instrumentation.

Typically, the Raman scattering is used to collect spectroscopic data through an inelastic scattering process based on molecular polarizability changes (Santos *et al.*, 2017). Inelastic scattering involves the frequency of changes that occur in the monochromatic photons in the light after interacting with samples. The electromagnetic scattering occurs due to vibrations and rotations between the molecules. The real photons have varied energy; therefore, the scattering system is likely to lose or gain power. The difference in the frequency of incoming and outgoing photons forms Stokes and anti-Stokes scattering, as shown in Figure A2.

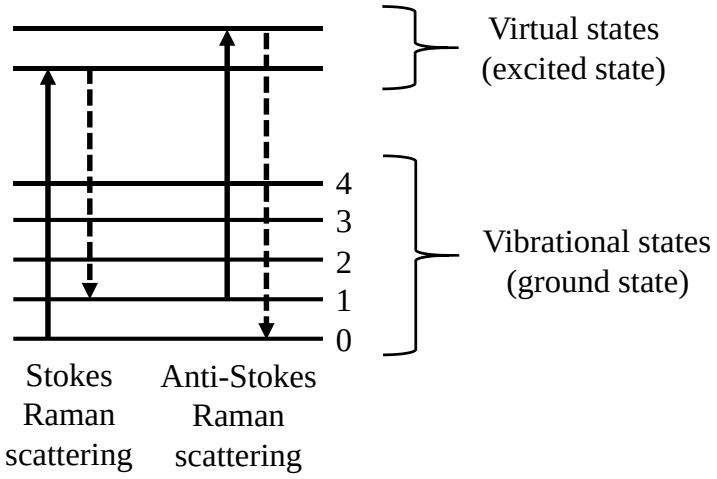

Figure A2. Stokes and Anti-Stokes Raman scattering, where continuous arrow: absorbed electromagnetic radiation; dashed arrow: released electromagnetic radiation.

APPENDIX B | SUPPLEMENTARY MATERIAL FOR CHAPTER 3

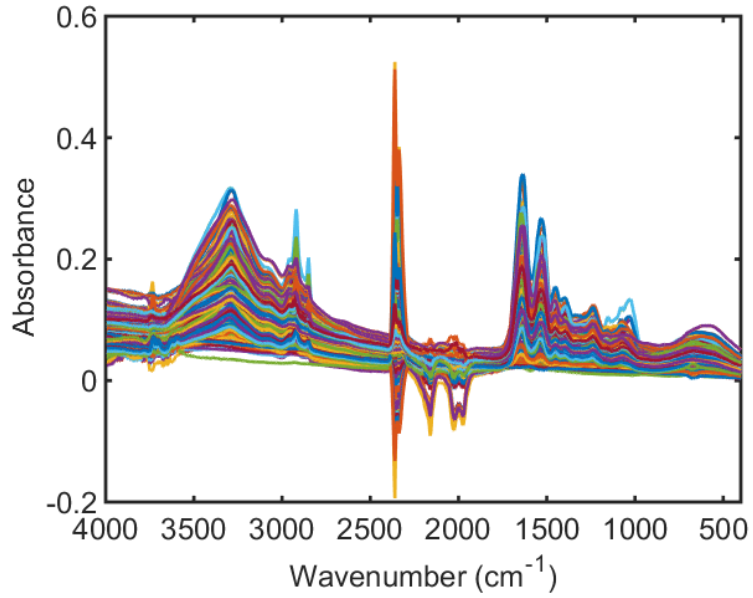

Figure B1. Raw IR spectra for meningiomas WHO Grade 1, 2 and 1-recurrence.

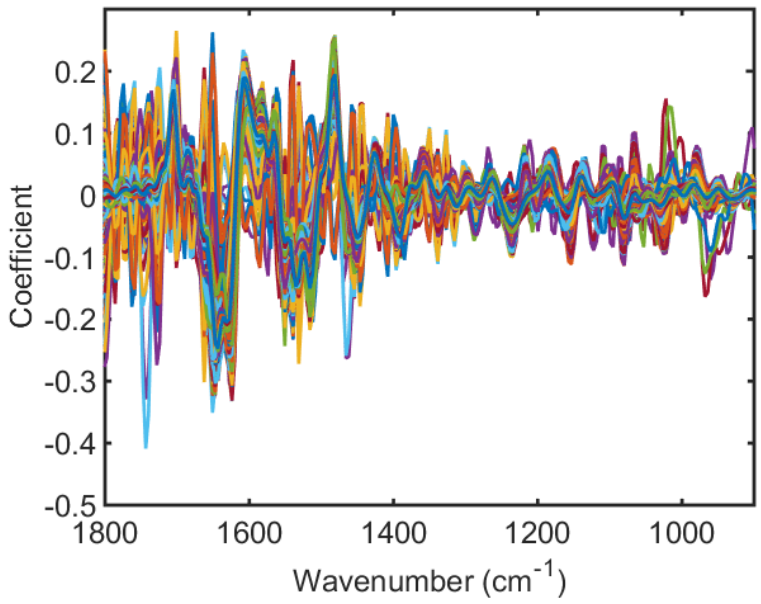

Figure B2. Pre-processed IR spectra (Savitzky-Golay 2nd derivative and vector normalisation) for meningiomas WHO Grade 1, 2 and 1-recurrence.

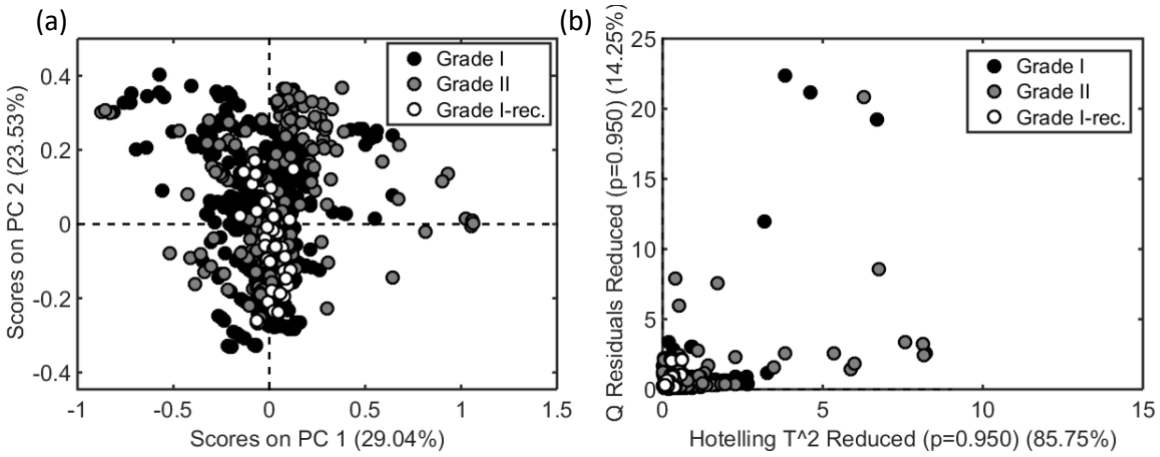

Figure B3. a) PCA scores on PC1 *versus* PC2 for the pre-processed spectral data in the fingerprint region (Savitzky-Golay 2nd derivative [window of 7 points, 2nd order polynomial fit] and vector normalisation); (b) Hotelling's T^2 *versus* Q residuals chart (6 PCs, 85.57% explained variance). Grade 1-rec. stands for WHO Grade 1 samples that reoccurred.

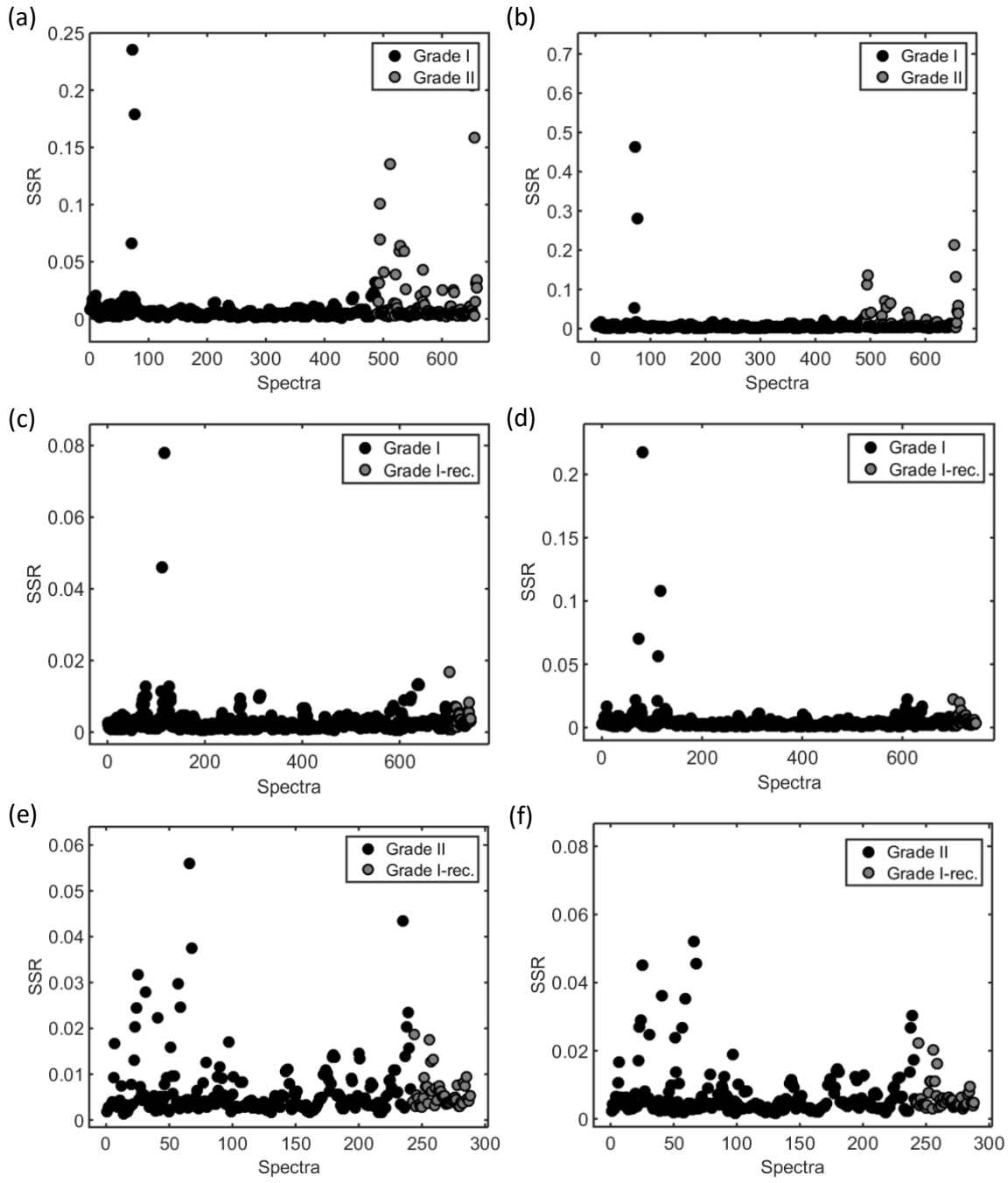

Figure B4. Sum of squared residuals (SSR) for (a) PCA-LDA and (b) PLS-DA models to distinguish Grade 1 *vs.* Grade 2 meningiomas; (c) PCA-LDA and (d) PLS-DA models to distinguish Grade 1 *vs.* Grade 1 meningiomas that reoccurred; (e) and (f) PCA-LDA and PLS-DA models to distinguish Grade 2 *vs.* Grade 1 meningiomas that reoccurred.

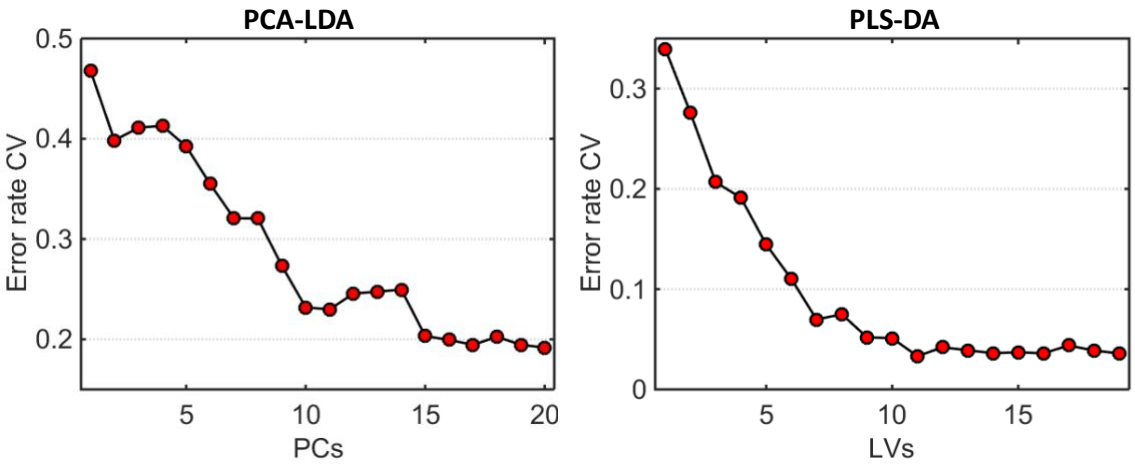

Figure B5. Cross-validation error for PCA-LDA and PLS-DA models to distinguish meningiomas grade 1 *vs.* grade 2 samples.

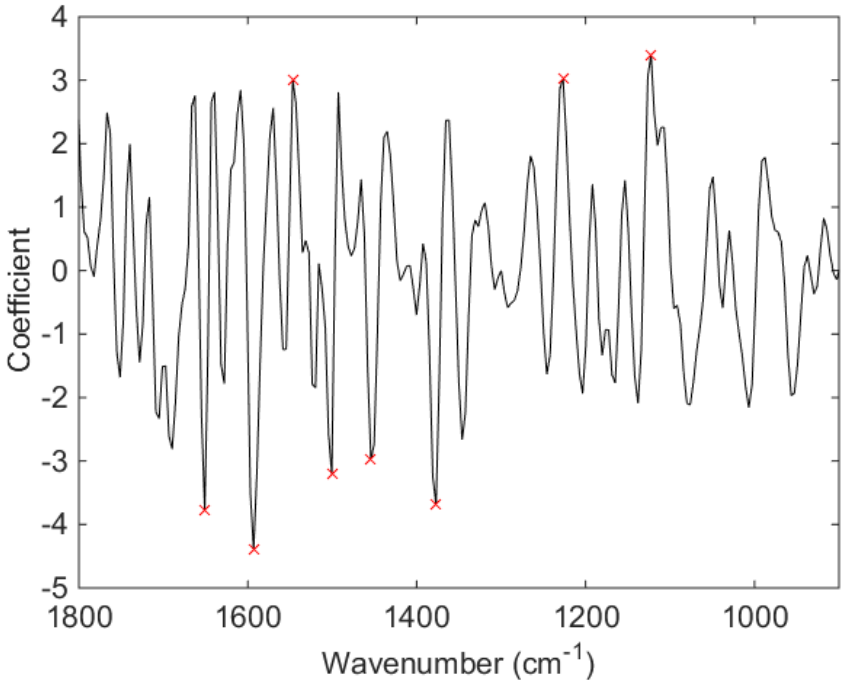

Figure B6. PLS-DA coefficients to distinguish meningiomas grade 1 *vs.* grade 2 samples.

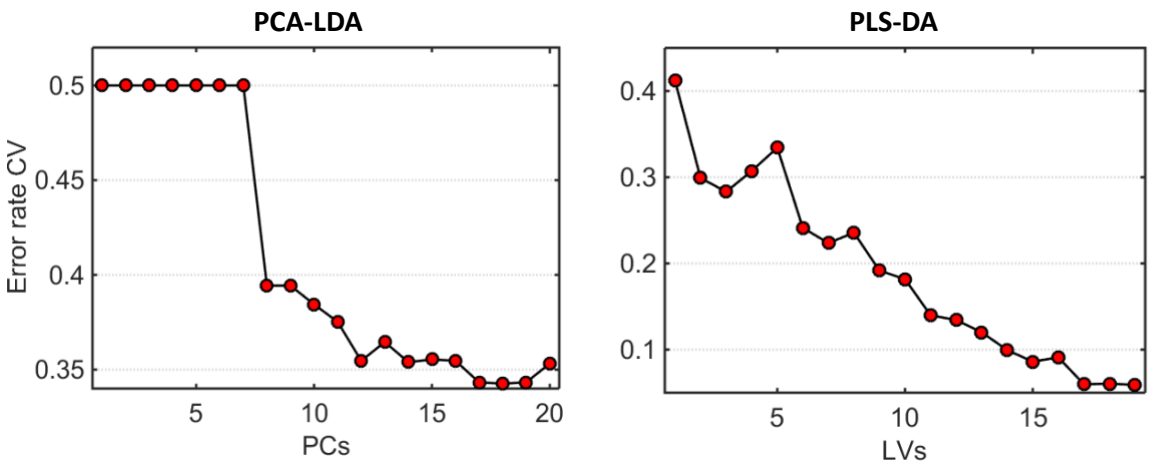

Figure B7. Cross-validation error for PCA-LDA and PLS-DA models to distinguish meningiomas grade 1 *vs.* grade 1 recurrence samples.

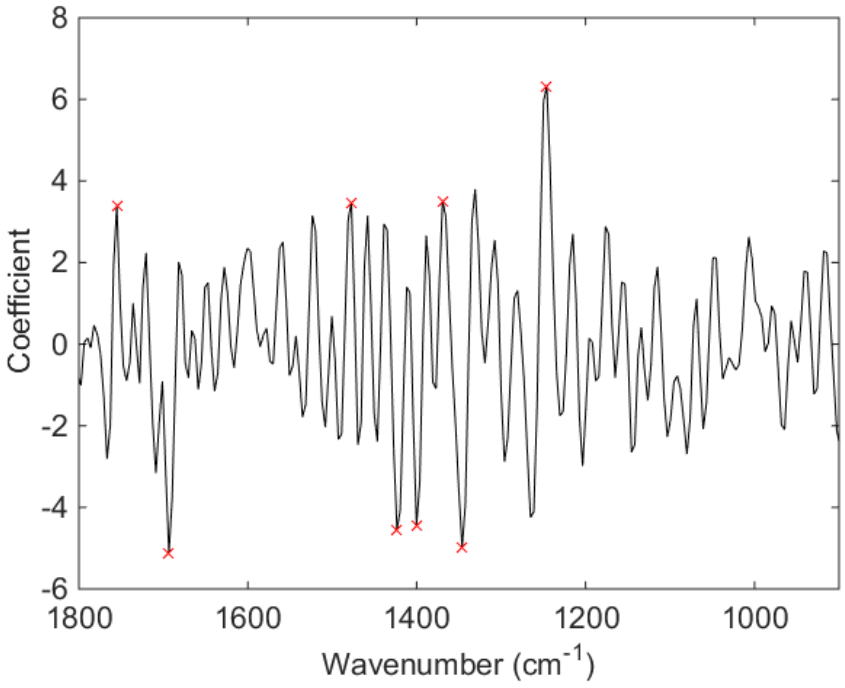

Figure B8. PLS-DA coefficients to distinguish meningiomas grade 1 *vs.* grade 1 recurrence samples.

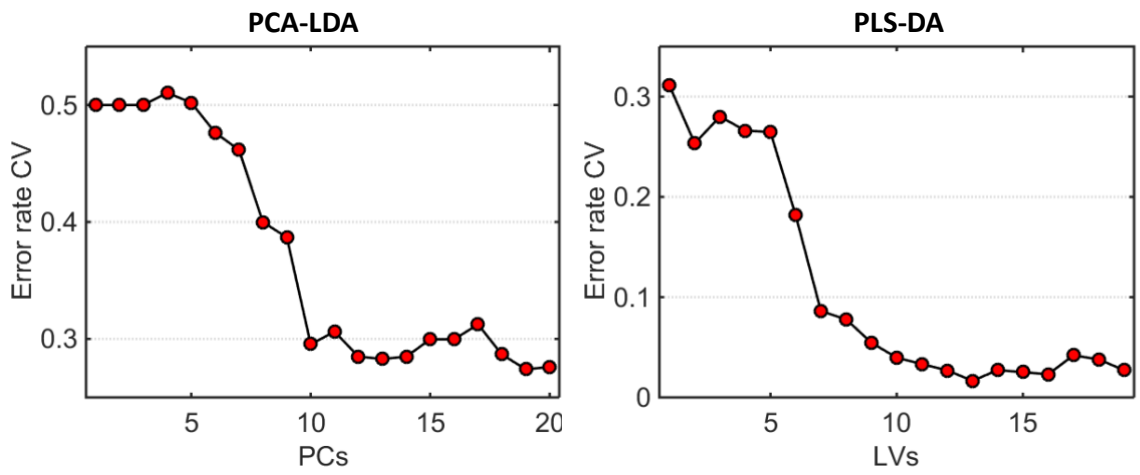

Figure B9. Cross-validation error for PCA-LDA and PLS-DA models to distinguish meningiomas grade 2 *vs.* grade 1 recurrence samples.

APPENDIX C | SUPPLEMENTARY MATERIAL FOR CHAPTER 4

Table C1. Correct classification rate for distinguishing Grade 1and Grade 2 meningiomas.

Algorithm	Class	Training	Test
PCA-LDA	Grade 1	80.0	31.6
	Grade 2	66.7	85.7
PCA-QDA	Grade 1	97.8	100
	Grade 2	73.3	85.7
PCA-SVM	Grade 1	100	73.7
	Grade 2	100	28.6
SPA-LDA	Grade 1	75.6	42.1
	Grade 2	66.7	100
SPA-QDA	Grade 1	95.6	100
	Grade 2	46.7	85.7
SPA-SVM	Grade 1	77.8	21.1
	Grade 2	100	71.4
GA-LDA	Grade 1	100	63.2
	Grade 2	93.3	57.1
GA-QDA	Grade 1	100	100
	Grade 2	86.7	0
GA-SVM	Grade 1	91.1	42.1
	Grade 2	100	42.9

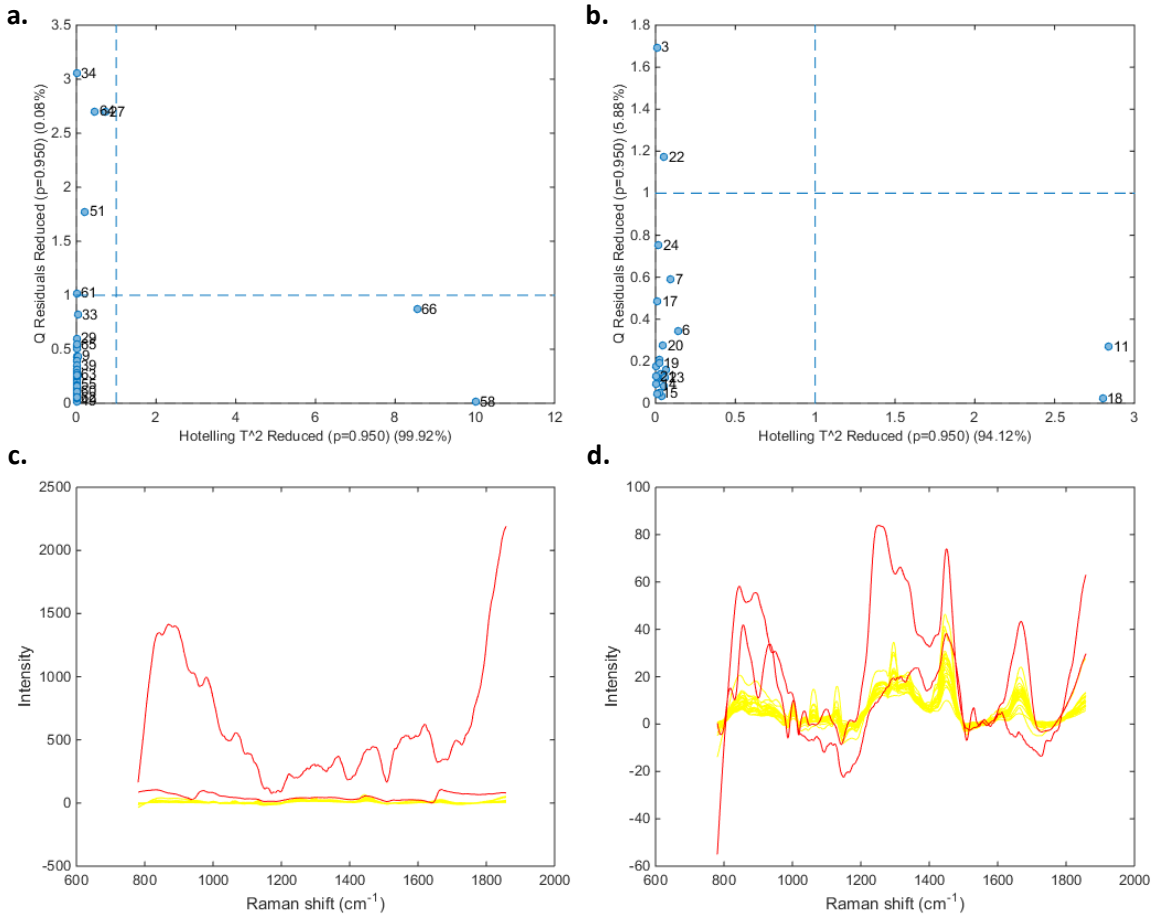

Figure C1. Outliers identified by a Hotelling T^2 *versus* Q residuals test (PCA with 8 PCs). (a) Meningioma Grade 1 samples (outliers: 58, 66); (b) meningioma Grade 2 samples (outliers: 11, 18); (c) meningioma Grade 1 outlier spectra in red; (d) meningioma Grade 2 outlier spectra in red.

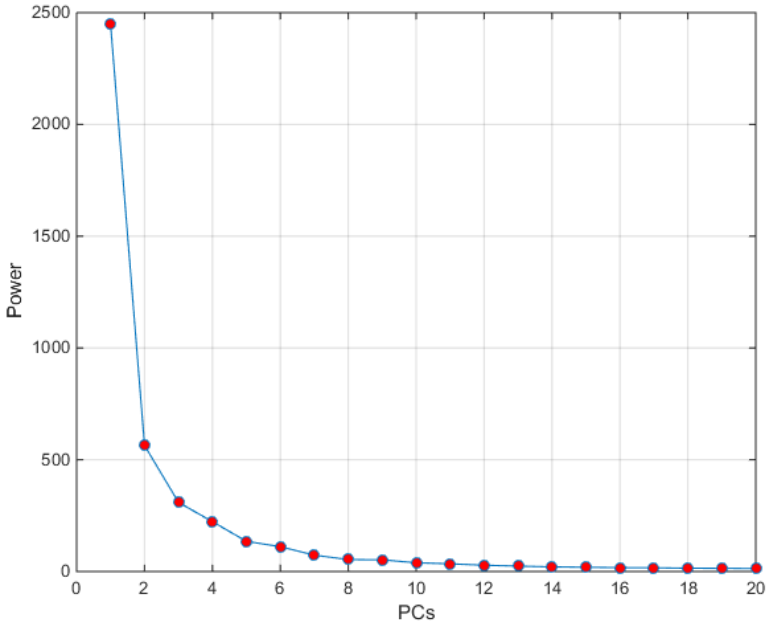

Figure C2. Singular value varying the number of principal components (PCs) of PCA.

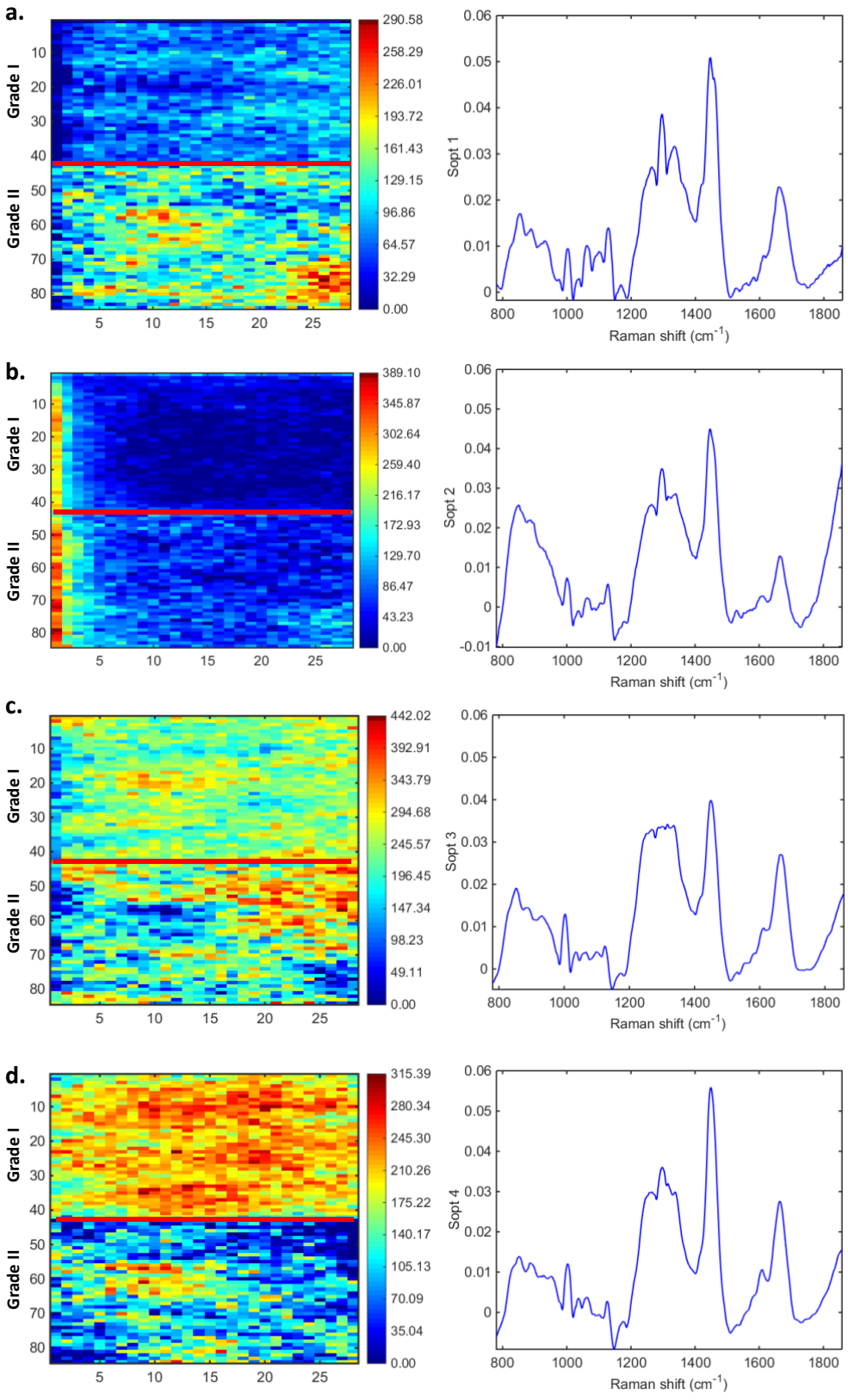

Figure C3. Concentration distribution maps and recovered spectral profiles by MCR-ALS for the 1st (a), 2nd (b), 3rd (c), and 4th (d) components. Colour bar: relative concentration.

PUBLICATIONS:

1. Lilo T, Morais CLM, Shenton C, Ray A, Gurusinghe N. Revising Fourier-transform infrared (FT-IR) and Raman spectroscopy towards brain cancer detection. *Photodiagnosis and Photodynamic Therapy* 2022; **38**: 102785.

2. Lilo T, L. M. Morais C, Ashton KM, et al. Raman hyperspectral imaging coupled to three-dimensional discriminant analysis: classification of meningiomas brain tumour grades. *Spectrochimica Acta Part A: Molecular and Biomolecular Spectroscopy* 2022: 121018.

3. Lilo T, Morais CLM, Ashton KM, et al. Spectrochemical differentiation of meningioma tumours based on attenuated total reflection Fourier-transform infrared (ATR-FTIR) spectroscopy. *Analytical and Bioanalytical Chemistry* 2020; **412**(5): 1077-86.

4. Morais CL, Lilo T, Ashton KM, et al. Determination of meningioma brain tumour grades using Raman microspectroscopy imaging. *Analyst* 2019; **144**(23): 7024-31.

5. Lilo T, Morais C, Ashton K, et al. Predicting meningioma recurrence using spectrochemical analysis of tissues and subsequent predictive computational algorithms. *Neuro-Oncology* 2019; **21**(Supplement_4): iv5-iv.

6. De Lelis Medeiros De Morais C, Lilo T, Ashton K, et al. Determination of meningioma brain tissue grades using Raman hyperspectral imaging. *Neuro-Oncology* 2019; **21**(Supplement_4): iv5-iv6.

7. Front Cover - Spectrochemical differentiation of meningioma tumours based on attenuated total reflection Fourier-transform infrared (ATR-FTIR) spectroscopy https://doi.org/10.1007/s00216-019-02332-w

Photodiagnosis and Photodynamic Therapy 38 (2022) 102785

Contents lists available at ScienceDirect

Photodiagnosis and Photodynamic Therapy

journal homepage: www.elsevier.com/locate/pdpdt

Revising Fourier-transform infrared (FT-IR) and Raman spectroscopy towards brain cancer detection

Taha Lilo [a,b,*], Camilo L.M. Morais [b], Catriona Shenton, Writing – review & editing [a], Arup Ray, Supervision [a], Nihal Gurusinghe, Supervision [a]

[a] Department of Neurosurgery, Royal Preston Hospital, Lancashire Teaching Hospitals NHS Trust, Preston PR2 9HT, UK
[b] School of Pharmacy and Biomedical Sciences, University of Central Lancashire, Preston PR1 2HE, UK

ARTICLE INFO

Keywords:
Brain cancer
Glioma
Meningioma
Glioblastoma
FT-IR spectroscopy
Raman

ABSTRACT

Fourier-transform infrared (FT-IR) and Raman spectroscopy are being widely applied as sensor-based techniques in oncology, particularly in the diagnosis of brain cancers and their subtypes. Overtime, these techniques have become more sensitive; and, accuracies of over 90% have been observed in several studies. This is indication of their potential for clinical implementation. Herein, we present a mini-review by revisiting some fundamentals of FT-IR and Raman spectroscopy along with their applications towards brain cancer detection in the literature.

1. Introduction

1.1. Brief history of Fourier-transform infrared (FT-IR) spectroscopy

Infrared (IR) spectroscopy is a vibrational spectroscopy technique used to assess the chemical composition of a sample [1]. It is based on the absorption of infrared light by the molecules that compose the material, where all molecules with a resultant dipole moment different from zero will absorb infrared radiation. The scientific idea behind the Fourier-transform infrared (FT-IR) spectroscopy was first initiated in the late 1880s by Albert A. Michelson. The founder invented an interferometer, a device that Albert and Morley used to perform famous experiments determined to measure the exact speed of light. Besides the Michelson interferometer, he also introduced the scientific optical instruments. His-efforts were widely accepted and appreciated by the scientists of the day. Later in 1907, Michelson's efforts and inventions were still applicable and he won the Nobel Prize in Physics.

Michelson knew the spectroscopic potential of his interferometer, although it lacked the sensitive detectors and the Fourier-transform algorithms that consequently barred the instrument from its practical application. However, he still manipulated and used it to solve many doublet spectra back then in the field [2]. There were quite many challenges that scientists faced while using Fourier-transform spectroscopy (FTS) to compute the Fourier-transform of interferograms. It is because the FTS was not able to directly invert the values, so they guessed some spectra, calculated the inverse of their Fourier-transform, and then compared it to the interferogram they had earlier measured. The best results were obtained after modifying the guessed spectra to match the data at hand.

It is in the late 1940s that the practical application of the FTS was considered useful. The scientists first used the interferograms when measuring light from the celestial bodies after producing the first Fourier-transform spectrum in 1949. At this point, it became more accessible for the scientists to calculate the continuous necessary Fourier transforms though it became a task that was so difficult and consumed much time. Here, the scientists introduced the lamellar granting and the Fabry-Perot interferometers, besides the Michelson's. The schematic Fig. 1a below represents the basic Michelson interferometer.

Movasaghi et al. [3] speculated that the lamellar granting spectrometer share many standard features with the Michelson's. These two beam and multicomplex devices have high optical ability to produce the interferograms, which, when Fourier-transformed, provide the desired spectrum. However, in the lamellar granting instrument, the optical modulation part constitutes a pair of mirrors that are arranged in a tongue and groove manner to bring the appearance of one large mirror divided into two or more horizontal strips as indicated in Fig. 1b.

Through the Fresnel mirrors, the scientists could observe interferences with the blue-ray path difference near line F at wavelength

* Corresponding author.
E-mail address: taha.lilo@icloud.com (T. Lilo).

https://doi.org/10.1016/j.pdpdt.2022.102785
Received 5 December 2021; Received in revised form 15 February 2022; Accepted 25 February 2022
Available online 26 February 2022

Spectrochimica Acta Part A: Molecular and Biomolecular Spectroscopy 273 (2022) 121018

Contents lists available at ScienceDirect

Spectrochimica Acta Part A: Molecular and Biomolecular Spectroscopy

journal homepage: www.elsevier.com/locate/saa

Raman hyperspectral imaging coupled to three-dimensional discriminant analysis: Classification of meningiomas brain tumour grades

Taha Lilo [a,b,*], Camilo L.M. Morais [b], Katherine M. Ashton [c], Charles Davis [b], Timothy P. Dawson [c], Francis L. Martin [d], Jane Alder [b], Gareth Roberts [a], Arup Ray [a], Nihal Gurusinghe [a]

[a] Department of Neurosurgery, Royal Preston Hospital, Lancashire Teaching Hospitals NHS Trust, Preston PR2 9HT, UK
[b] School of Pharmacy and Biomedical Sciences, University of Central Lancashire, Preston PR1 2HE, UK
[c] Department of Neuropathology, Royal Preston Hospital, Lancashire Teaching Hospitals NHS Trust, Preston PR2 9HT, UK
[d] Biocel UK Ltd, Hull HU10 6TS, UK

HIGHLIGHTS

- Raman hypespectral imaging can diagnose meningiomas tumour grades.
- Three-dimensional discriminant analysis algorithms were applied.
- The technique is reagent-free, quick and accurate.
- High test accuracy, sensitivity and specificity were observed.
- This technique could be a robust diagnostic tool.

GRAPHICAL ABSTRACT

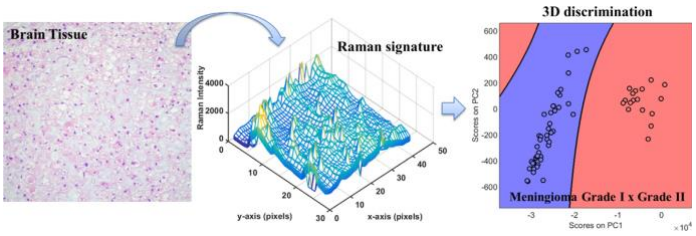

ARTICLE INFO

Article history:
Received 17 October 2021
Received in revised form 4 February 2022
Accepted 6 February 2022
Available online 8 February 2022

Keywords:
Raman hyperspectral imaging
Meningiomas
Brain cancer
Three-dimensional classification
Biospectroscopy

ABSTRACT

Meningiomas remains a clinical dilemma. They are the commonest "benign" types of brain tumours and, although being typically benign, they are divided into three WHO grades categories (I, II and III) which are associated with the tumour growth rate and likelihood of recurrence. Recurrence depends on extend of surgery as well as histopathological diagnosis. There is a marked variation amongst surgeons in the follow-up arrangements for their patients even within the same unit which has a significant clinical, and financial implication. Knowing the tumour grade rapidly is an important factor to predict surgical outcomes and adequate patient treatment. Clinical follow up sometimes is haphazard and not based on clear evidence. Spectrochemical techniques are a powerful tool for cancer diagnostics. Raman hyperspectral imaging is able to generate spatially-distributed spectrochemical signatures with great sensitivity. Using this technique, 95 brain tissue samples (66 meningiomas WHO grade I, 24 meningiomas WHO grade II and 5 meningiomas that reoccurred) were analysed in order to discriminate grade I and grade II samples. Newly-developed three-dimensional discriminant analysis algorithms were used to process the hyperspectral imaging data in a 3D fashion. Three-dimensional principal component analysis quadratic discriminant analysis (3D-PCA-QDA) was able to distinguish grade I and grade II meningioma samples with 96% test accuracy (100% sensitivity and 95% specificity). This technique is here shown to be a high-throughput, reagent-free,

* Corresponding author at: Department of Neurosurgery, Royal Preston Hospital, Lancashire Teaching Hospitals NHS Trust, Preston PR2 9HT, UK.
E-mail address: taha.lilo@icloud.com (T. Lilo).

https://doi.org/10.1016/j.saa.2022.121018

Analyst

PAPER

View Article Online
View Journal | View Issue

Cite this: *Analyst*, 2019, **144**, 7024

Determination of meningioma brain tumour grades using Raman microspectroscopy imaging†

Camilo L. M. Morais, *[a] Taha Lilo,[a,b] Katherine M. Ashton,[c] Charles Davis,[a] Timothy P. Dawson, [c] Nihal Gurusinghe[b] and Francis L. Martin *[a]

Received 13th August 2019,
Accepted 18th October 2019

DOI: 10.1039/c9an01551e

rsc.li/analyst

Raman spectroscopy is a powerful technique used to analyse biological materials, where spectral markers such as proteins (1500–1700 cm^{-1}), carbohydrates (470–1200 cm^{-1}) and phosphate groups of DNA (980, 1080–1240 cm^{-1}) can be detected in a complex biological medium. Herein, Raman microspectroscopy imaging was used to investigate 90 brain tissue samples in order to differentiate meningioma Grade I and Grade II samples, which are the commonest types of brain tumour. Several classification algorithms using feature extraction and selection methods were tested, in which the best classification performances were achieved by principal component analysis-quadratic discriminant analysis (PCA-QDA) and successive projections algorithm-quadratic discriminant analysis (SPA-QDA), resulting in accuracies of 96.2%, sensitivities of 85.7% and specificities of 100% using both methods. A biochemical profiling in terms of spectral markers was investigated using the difference-between-mean (DBM) spectrum, PCA loadings, SPA-QDA selected wavenumbers, and the recovered imaging profiles after multivariate curve resolution alternating least squares (MCR-ALS), where the following wavenumbers were found to be associated with class differentiation: 850 cm^{-1} (amino acids or polysaccharides), 1130 cm^{-1} (phospholipid structural changes), the region between 1230–1360 cm^{-1} (Amide III and CH_2 deformation), 1450 cm^{-1} (CH_2 bending), and 1858 cm^{-1} (C=O stretching). These findings highlight the potential of Raman microspectroscopy imaging for determination of meningioma tumour grades.

Introduction

Raman spectroscopy provides sensitive spectrochemical signatures of materials based on their molecular polarisability changes.[1] Raman is based on an inelastic scattering phenomenon that occurs in less than 1% of the absorbed photons by a molecule. This inelastic scattering is composed of Stokes and anti-Stokes scattering: the former occurs when the molecule emits a photon with less energy than the absorbed incoming radiation, and the latter happens when the molecule emits a photon with higher energy than the absorbed incoming radiation.[2] At room temperature, the Stokes scattering is more frequent, thus most instruments filter the elastic and anti-Stokes scattering and record the Stokes scattering signal as the final Raman spectrum.

Microspectroscopy Raman imaging allows one to obtain microscopically spatially distributed spectral data, where each position in the image is composed of a Raman spectrum in a specific wavenumber range. The hyperspectral image data are represented by three-dimensional (3D) arrays, where the spatial coordinates are present in the *x*- and *y*-axis while the spectral information is in the *z*-axis. A major advantage of Raman imaging is that it can be non-destructive depending on the incident laser frequency, has minimum water interference, and has a relatively low cost in comparison with other analytical techniques.

Raman imaging has been used in a wide range of applications, including pharmaceutical analysis,[3] forensic investigations,[4] food quality control,[5] and to analyse biological materials.[6] In the latter, cancer detection plays an important role, where Raman imaging has been successfully applied to investigate breast,[7] cervical,[8] lung,[8] skin,[9] ovarian,[10] and brain cancer.[11]

Most of brain cancers are gliomas or meningioma tumours.[12] Gliomas are more aggressive types of tumours and have been widely investigated using Raman spectroscopy,[12–15]

[a]*School of Pharmacy and Biomedical Sciences, University of Central Lancashire, Preston PR1 2HE, UK. E-mail: cdlmedeiros-de-morai@uclan.ac.uk, flmartin@uclan.ac.uk*
[b]*Neurosurgery, Royal Preston Hospital, Lancashire Teaching Hospitals NHS Trust, Preston PR2 9HT, UK*
[c]*Neuropathology, Royal Preston Hospital, Lancashire Teaching Hospitals NHS Trust, Preston PR2 9HT, UK*

†Electronic supplementary information (ESI) available. See DOI: 10.1039/c9an01551e

Analytical and Bioanalytical Chemistry
https://doi.org/10.1007/s00216-019-02332-w

RESEARCH PAPER

Spectrochemical differentiation of meningioma tumours based on attenuated total reflection Fourier-transform infrared (ATR-FTIR) spectroscopy

Taha Lilo[1,2] · Camilo L. M. Morais[2] · Katherine M. Ashton[3] · Ana Pardilho[1] · Charles Davis[2] · Timothy P. Dawson[3] · Nihal Gurusinghe[1] · Francis L. Martin[2]

Received: 1 October 2019 / Revised: 11 November 2019 / Accepted: 5 December 2019

Abstract
Meningiomas are the commonest types of tumours in the central nervous system (CNS). It is a benign type of tumour divided into three WHO grades (I, II and III) associated with tumour growth rate and likelihood of recurrence, where surgical outcomes and patient treatments are dependent on the meningioma grade and histological subtype. The development of alternative approaches based on attenuated total reflection Fourier-transform infrared (ATR-FTIR) spectroscopy could aid meningioma grade determination and its biospectrochemical profiling in an automated fashion. Herein, ATR-FTIR in combination with chemometric techniques is employed to distinguish grade I, grade II and grade I meningiomas that re-occurred. Ninety-nine patients were investigated in this study where their formalin-fixed paraffin-embedded (FFPE) brain tissue samples were analysed by ATR-FTIR spectroscopy. Subsequent classification was performed via principal component analysis plus linear discriminant analysis (PCA-LDA) and partial least squares plus discriminant analysis (PLS-DA). PLS-DA gave the best results where grade I and grade II meningiomas were discriminated with 79% accuracy, 80% sensitivity and 73% specificity, while grade I versus grade I recurrence and grade II versus grade I recurrence were discriminated with 94% accuracy (94% sensitivity and specificity) and 97% accuracy (97% sensitivity and 100% specificity), respectively. Several wavenumbers were identified as possible biomarkers towards tumour differentiation. The majority of these were associated with lipids, protein, DNA/RNA and carbohydrate alterations. These findings demonstrate the potential of ATR-FTIR spectroscopy towards meningioma grade discrimination as a fast, low-cost, non-destructive and sensitive tool for clinical settings.

Keywords Meningioma · Infrared spectroscopy · ATR-FTIR · Chemometrics

Introduction

Meningioma and glioma tumours constitute the majority of primary brain cancers [1]. Gliomas are a more aggressive and intrinsic type of tumour, which comprise neuroepithelial tumours originating from the glial or supporting cells of the central nervous system (CNS) [2]. Meningiomas are the commonest type of brain tumours, showing differentiation towards the meninges surrounding the brain and the spinal cord [3]. They are slow-growing extrinsic tumours with variable prognosis, occasionally growing to a very large size. The majority occur in a supratentorial location, while a few can arise in the posterior cranial fossa and, rarely, as extracranial meningiomas [4]. They often manifest as single or sporadic lesions, producing non-descript symptoms. The symptoms are variable in nature depending on the location and the size of the lesion. The most common presenting symptom is headache. However, symptoms may include any sensory and/or motor deficits and gait disturbance.

Multiple meningiomas are commonly associated with neurofibromatosis type II [5]. Meningiomas can be

Electronic supplementary material The online version of this article (https://doi.org/10.1007/s00216-019-02332-w) contains supplementary material, which is available to authorized users.

✉ Francis L. Martin
flmartin@uclan.ac.uk

[1] Department of Neurosurgery, Royal Preston Hospital, Lancashire Teaching Hospitals NHS Trust, Preston PR2 9HT, UK

[2] School of Pharmacy and Biomedical Sciences, UCLan, Preston PR1 2HE, UK

[3] Department of Neuropathology, Royal Preston Hospital, Lancashire Teaching Hospitals NHS Trust, Preston PR2 9HT, UK

Published online: 21 December 2019

Volume 412 · Number 5 · January 2020

ANALYTICAL & BIOANALYTICAL CHEMISTRY

Gas-aggregated Ag nanoparticles for detecting small molecules using LDI MS
Dynamic in vitro intestinal barrier model coupled to chip-based LC-MS
Multi-sensor integration approach based on hyperspectral imaging and electronic nose
Spectrochemical differentiation of meningioma tumours based on ATR-FTIR spectroscopy

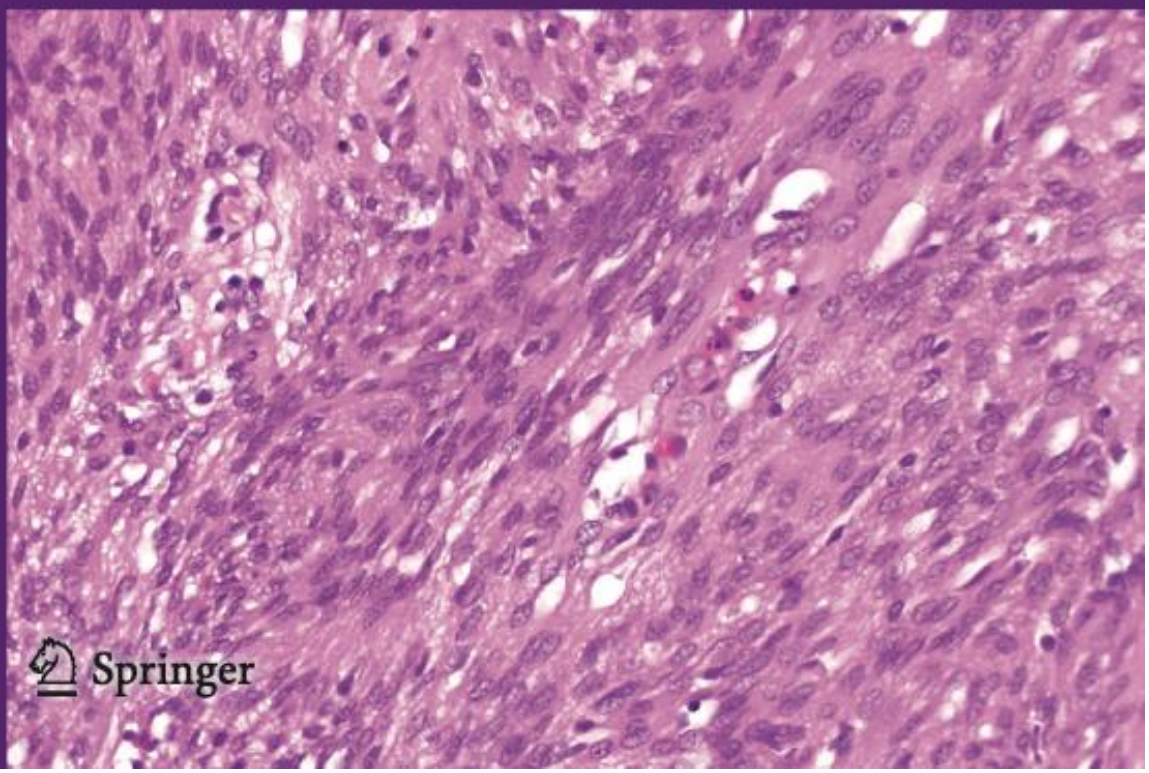

Springer